UNIVERSITAT POLITÈCNICA DE VALÈNCIA

Department of Mechanical and Materials Engineering

Ph.D. Thesis

Direct creation of patient-specific Finite Element models from medical images and preoperative prosthetic implant simulation using h-adaptive Cartesian grids

Presented by: Luca Giovannelli M.Sc.

Supervised by: Dr. Juan José Ródenas García

Dr. Manuel Tur Valiente

Valencia, September 2018

Ph.D. Thesis

Direct creation of patient-specific Finite Element models from medical images and preoperative prosthetic implant simulation using h-adaptive Cartesian grids

for the degree of

Doctor in Industrial Engineering and Production

presented by

Luca Giovannelli M.Sc.

at the

Department of Mechanical and Materials Engineering

of Universitat Politècnica de València

Supervised by

Dr. Juan José Ródenas García
Dr. Manuel Tur Valiente

Valencia, September 2018

Ph.D. THESIS

Direct creation of patient-specific Finite Element models from medical images and preoperative prosthetic implant simulation using h-adaptive Cartesian grids

Presented by:	Luca Giovannelli M.Sc.
Supervised by:	Dr. Juan José Ródenas García
	Dr. Manuel Tur Valiente

QUALIFYING TRIBUNAL

PRESIDENT: Dr. _____

VOCAL: Dr. _____

SECRETARY: Dr. _____

Valencia, September 2018

Abstract

In silico medicine is believed to be one of the most disruptive changes in the near future. A great effort has been carried out during the last decade to develop predicting computational models to increase the diagnostic capabilities of medical doctors and the effectiveness of therapies. One of the key points of this revolution, will be personalisation, which means in most of the cases creating patient specific computational models, also called digital twins. This practice is currently wide-spread in research and there are quite a few software products in the market to obtain models from images. Nevertheless, in order to be usable in the clinical practice, these methods have to drastically reduce the time and human intervention required for the creation of the numerical models.

This thesis focuses on the proposal of the image-based Cartesian grid Finite Element Method (*cg*FEM), a technique to automatically obtain numerical models from images and carry out linear structural analyses of bone, implants or heterogeneous materials.

In the method proposed in this thesis, after relating the image scale to corresponding elastic properties, all the pixel information will be used for the integration of the element stiffness matrices, which homogenise the elastic behaviour of the groups of pixels contained in each element. An initial uniform Cartesian mesh is h-adapted to the image characteristics by using an efficient refinement procedure which takes into account the local elastic properties associated to the pixel values. Doing so we avoid

an excessive elastic property smoothing due to element integration in highly heterogeneous areas, but, nonetheless we obtain final models with a reasonable number of degrees of freedom.

The result of this process is a non-conforming mesh in which C_0 continuity is enforced via multipoint constraints at the hanging nodes. In contrast to the standard procedures for the creation of Finite Element models from images, which usually require a complete and watertight definition of the geometry and treat the result as a standard CAD, with cgFEM it is not necessary to define any geometrical entity, as the procedure proposed leads to an implicit definition of the boundaries. Nonetheless, it is straightforward to include them explicitly in the model if necessary, such as smooth surfaces to impose the boundary conditions more precisely or CAD models of endoprostheses for the simulation of implants. As a consequence, the amount of human work required for the creation of the numerical models is drastically reduced.

In this thesis, we analyse in detail the new method behaviour in 2D and 3D problems from CT-scans, X-ray images and synthetic images, focusing on three classes of problems. These include the simulation of bones, the material characterisation of solid foams from CT scans, for which we developed the cgFEM virtual characterisation technique, and the structural analysis of future implants, taking advantage of the capability of cgFEM to easily mix images and CAD models.

Resumen

Se cree que la *medicina in silico* supondrá uno de los cambios más disruptivos en el futuro próximo. A lo largo de la última década se ha invertido un gran esfuerzo en el desarrollo de modelos computacionales predictivos para mejorar el poder de diagnóstico de los médicos y la efectividad de las terapias. Un punto clave de esta revolución, será la personalización, que conlleva en la mayoría de los casos, la creación de modelos computacionales específicos de paciente, también llamados gemelos digitales. Esta práctica está actualmente extendida en la investigación y existen en el mercado varias herramientas de software que permiten obtener modelos a partir de imágenes. A pesar de eso, para poder usar estos métodos en la práctica clínica, se necesita reducir drásticamente el tiempo y el trabajo humano necesarios para la creación de los modelos numéricos.

Esta tesis se centra en la propuesta de la versión basada en imágenes del *Cartesian grid Finite Element Method* (*cg*FEM), una técnica para obtener de forma automática modelos a partir de imágenes y llevar a cabo análisis estructurales lineales de huesos, implantes o materiales heterogéneos.

En la técnica propuesta, tras relacionar la escala de color de la imágen con valores de propiedades mecánicas, se usa toda la información contenida en los píxeles para evaluar las matrices de rigidez de los elementos que homogenizan el comportamiento elástico de los grupos de píxeles contenidos en cada elemento. Se h-adapta una malla cartesiana inicialmente uniforme a las características de la imágen usando un pro-

cedimiento eficiente que tiene en cuenta las propiedades elásticas locales asociadas a los valores de los píxeles. Con eso, se evita un suavizado excesivo de las propiedades elásticas debido a la integración de los elementos en áreas altamente heterogéneas, pero, no obstante, se obtienen modelos finales con un número razonable de grados de libertad.

El resultado de este proceso es una malla no conforme en la que se impone la continuidad C_0 de la solución mediante restricciones multi-punto en los *hanging nodes*. Contrariamente a los procedimientos estandar para la creación de modelos de Elementos Finitos a partir de imágenes, que normalmente requieren la definición completa y *watertight* de la geometrá y tratan el resultado como un CAD estandar, con *cg*FEM no es necesario definir ninguna entidad geométrica dado que el procedimiento propuesto conduce a una definición implícita de los contornos. Sin embargo, es inmediato incluirlas explícitamente en el modelo en el caso de que sea necesario, como por ejemplo superficies suaves para imponer condiciones de contorno de forma más precisa o volúmenes CAD de dispositivos para la simulación de implantes. Como consecuencia de eso, la cantidad de trabajo humano para la creación de modelos se reduce drásticamente.

En esta tesis, se analiza en detalle el comportamiento del nuevo método en problemas 2D y 3D a partir de CT-scan, radiográfias e imágenes sintéticas, centrandose en tres clases de problemas. Estos incluyen la simulación de huesos, la caracterización de materiales a partir de TACs, para lo cual se ha desarrollado la *cgFEM virtual characterisation technique*, y el análisis estructural de futuros implantes, aprovechando la capacidad del *cg*FEM de combinar fácilmente imágenes y modelos de CAD.

Resum

Es creu que la medicina in silico suposarà un dels canvis més disruptius en el futur pròxim. Al llarg de l'última dècada, s'ha invertit un gran esforç en el desenvolupament de models computacionals predictius per millorar el poder de diagnòstic dels metges i l'efectivitat de les teràpies. Un punt clau d'aquesta revolució, serà la personalització, que comporta en la majoria dels casos la creació de models computacionals específics de pacient. Aquesta pràctica està actualment estesa en la investigació i hi ha al mercat diversos software que permeten obtenir models a partir d'imatges. Tot i això, per a poder-se utilitzar en la pràctica clínica aquests métodes es necessita reduir dràsticament el temps i el treball humà necessaris per a la seva creació. Aquesta tesi es centra en la proposta d'una versió basada en imatges del *Cartesian grid Finite Element Method* (*cg*FEM), una técnica per obtenir de forma automàticament models a partir d'imatges i dur a terme anàlisis estructurals lineals d'ossos, implants o materials heterogenis. Després de relacionar l'escala del imatge a propietats macàniques corresponents, s'usa tota la informació continguda en els píxels per a integrar les matrius de rigidesa dels elements que homogeneïtzen el comportament elàstic dels grups de píxels continguts en cada element. Es emphh-adapta una malla inicialment uniforme a les característiques de la imatge usant un procediment eficient que té en compte les propietats elàstiques locals associades als valors dels píxels. Amb això, s'evita un suavitzat excessiu de les propietats elàstiques a causa de la integració dels elements en àrees altament heterogénies, però, tot i això, s'obtenen models finals amb un nombre

raonable de graus de llibertat. El resultat d'aquest procés és una malla no conforme en la qual s'imposa la continuïtat C_0 de la solució mitjançant restriccions multi-punt en els hanging nodes. Contràriament als procediments estàndard per a la creació de models d'Elements finits a partir d'imatges, que normalment requereixen la definició completa i *watertight* de la geometria i tracten el resultat com un CAD estàndard, amb *cg*FEM no cal definir cap entitat geométrica. No obstant això, és immediat incloure-les en el model en el cas que sigui necessari, com ara superfícies suaus per imposar condicions de contorn de forma més precisa o volums CAD de dispositius per a la simulació d'implants. Com a conseqüència d'això, la quantitat de treball humà per a la creació de models es redueix dràsticament. En aquesta tesi, s'analitza en detalls el comportament del nou métode en problemes 2D i 3D a partir de CT-scan i radiografies sintétiques i reals, centrant-se en tres classes de problemes. Aquestes inclouen la simulació d'ossos, la caracterització de materials a partir de TACs, per a la qual s'ha desenvolupat la *cg*FEM virtual characterisation technique, i l'anàlisi estructural de futurs implants, aprofitant la capacitat del *cg*FEM de combinar fàcilment imatges i models de CAD.

Acknowledgements

Contents

Chapter 1

Introduction

Nowadays, the use of numerical models based on volumetric image data is widespread in biomechanics. Great efforts have been made to solve the elasticity problem in a number of patient specific medical applications using the Finite Element Method (FEM), common in structural engineering. This is the case, for instance, of the prediction of bone fracture risk, [1], [2], [3], [4], and the evaluation of bone quality parameters for the detection of osteoporosis, [5] and [6]. Preoperative implant simulation is a particularly promising use for patient-specific numerical models. This is fundamental for several applications such as studying the effect of positioning [7], predicting the long term prosthesis performance thanks to the recent advances in bone remodelling [8], [9] and [10], designing customized implants taking advantage of optimization and 3D printing [11] and [12].

FEM is a numerical technique which provides approximate solutions for Boundary Value Problems (BVPs) described by Partial Differential Equations (PDEs). It started to be developed at middle of the last century fuelled by the necessity to solve complex problems related to elasticity and structural analysis in aeronautical and civil engineering.

After gaining solid mathematical bases in the 1960s and 1970s, it spread to a wider variety of disciplines such as, among others, chemistry and biology, and became the predominant simulation method in Computer Aided Engineering (CAE), which consists of a design stage, in which a component geometrically defined by a Computer Aided Design (CAD) system, and an analysis stage, in which its behaviour under a specific load condition is predicted by performing a FEM analysis.

The high cost in terms of man-hour is well known in the case of ordinary FE applications, in which the generation of the mesh from CAD models is often one of the most time consuming steps of the whole simulation process, as pointed out by [13] and [14].

In this context, a great number of numerical techniques have been proposed to streamline the modelling of complex geometries. Most of them are geometry independent techniques defined by the umbrella term of Finite Elements in ambient space, [15] but available in the literature under a number of different names such as Fictitious Domain, [16], or Embedded Methods, [17], among others. These were originally developed to reduce the modelling effort for standard, CAD-based FE problems, which is, even in this case, responsible for about 80% of all the simulation time cost, [18]. These methods simplify the mesh generation by using an auxiliary domain Ω_e, in general characterized by a simple, easy to mesh geometry, containing the problem domain Ω. The auxiliary, or meshing, domain Ω_e is discretised instead of the problem domain Ω. During the evaluation of the element integrals these methods require the information about the problem domain because the mesh does not conform to Ω.

The Cartesian grid Finite Element Method (*cg*FEM), which is the background of this thesis, belongs to the category of Finite Elements in ambient space. It uses geometry-independent grids to create non conforming discretisation meshes in order to make the modelling stage automatic and overcome the shortcomings of traditional FEM.

In *geometry-based cg*FEM the problem domain is immersed into a hierarchical structure of Cartesian grids. For the elements on the boundary the stiffness matrix is calculated solely by integrating the part of the element actually lying within the domain Ω. Special techniques are used to account for the exact geometry during the element integration process, thus avoiding modelling errors associated to an inexact representation of the boundary [19]. A local h-adaptive refinement is used to enhance the solution [20].

In the last decades, it has become more and more common to carry out FEM simulations on models obtained from Volumetric Images such as Computed Tomography (CT) and Magnetic Resonance (MR) scans for certain applications, especially in biomechanics and material science.
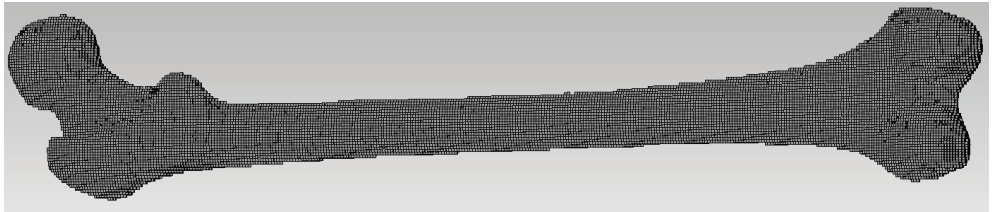
(a)
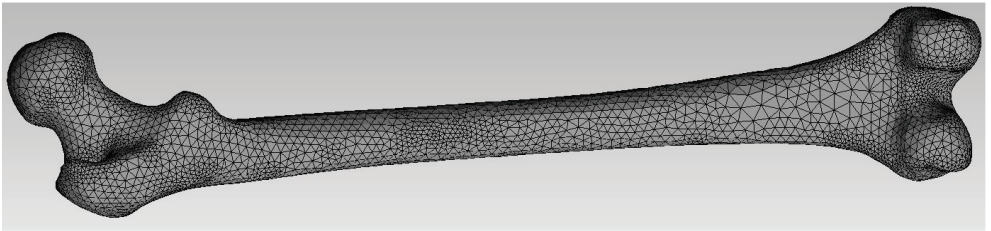
(b)

Figure 1.1: Classical meshes of CT-based femur model. (a) *voxel-based* hexahedral mesh; (b) *geometry-based* tetrahedral mesh.

Even more challenging obstacles to automatic modelling can be found in these cases, because the surfaces and volumes are not expressed in an explicit form in the first place, but they have to be obtained from bitmaps by means of segmentation tools. It is necessary to avoid the presence of unconnected domains and to make the surfaces close exactly when they define volumes. These problems are not trivial and their solution is hard to automate.

A common approach consists in selecting a number of pixels in the image based on the grey level and assigning an element of the FE mesh to each pixel/voxel, as done for instance by [5] and [21]. This produces hexahedral meshes which, in some cases, can be processed to smooth the external surfaces. This method generates FE models which have a very large number of degrees of freedom and therefore involves a high computational effort, see Figures 1.1a and 1.2a.
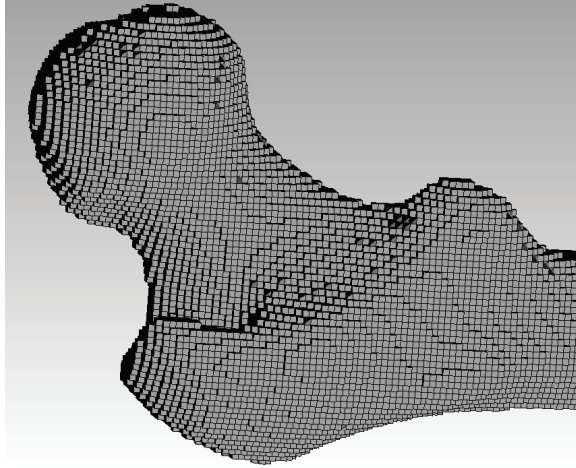
(a)
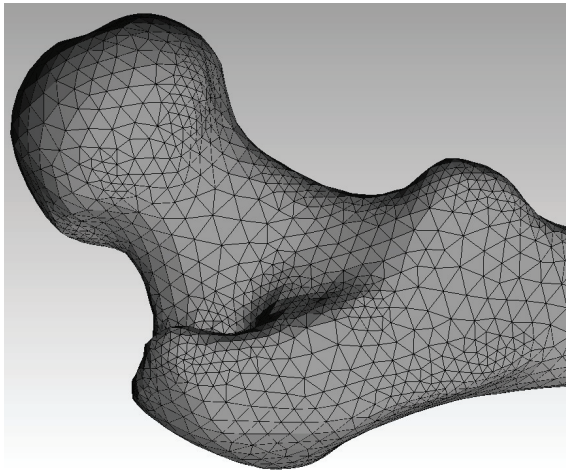
(b)

Figure 1.2: Classical meshes of CT-based proximal femur model. (a) *voxel-based* hexahedral mesh; (b) *geometry-based* tetrahedral mesh.

Another common solution is to create surfaces on the basis of the variation of the color levels in the image and to use them to define volumes. Then the unconnected domains have to be deleted and the mesh can finally be created in the usual way as if it were a CAD model, [22], [23]. In this case, surfaces are required to create

perfectly closed volumes, which might possibly need human intervention. The resulting geometry can be seen as extra information which does not exist in the original image. In both cases the image needs to be heavily processed before mesh tools can be used, see Figures 1.1b and 1.2b. Furthermore, the way they deal with material properties usually consists of individuating which living tissue corresponds to each volume and assigning the corresponding material characteristics from the literature as if the domains were homogeneous. This makes it impossible to take into account the heterogeneity of the material during the simulation using standard methods. For prosthesis analyses, for example, the *geometry-based* FE approach, [24], is usually preferred because the assembly between the geometrical models can be performed with standard CAD tools. On the other hand, when a reliable relation between voxel values and elastic properties is available, as in the case of bone CT scan, it is usually easier to take it into account using *voxel-based* methods due to the correspondence between elements and voxels. Doing the same with *geometry-based* meshes is more complicated because the elements do not conform to the pixels. A possible solution lies in assigning each integration point the average value of the stiffness corresponding to the surrounding pixels. Nevertheless the size of this influence area is not univocally defined, [25].

This thesis is a contribution to the relatively recent efforts to overcome the shortcomings of these standard methods by using the approach of Finite Elements in Ambient Space to domains defined in images. In particular we remark the application to image-based problems of X-FEM, [26] and [27], Composite Finite Elements, [28], both taking advantage of a level set representation of the boundaries obtained by standard segmentation procedures, and the Finite Cell Method (FCM), [29] and [30], which combines the fictitious domain approach with high-order hierarchical Ansatz spaces by p-adapting a non conforming Cartesian mesh in which the pixels are treated as integration subdomains. Recently a method combining FCM and Isogeometric analysis (IGA) has been proposed [31] to model the elastic behaviour of trabecular bone from μCT scans. This includes a B-spline level set function, which makes it possible to obtain a smooth representation of boundaries from the pixelated segmentation mask of the trabeculae, and locally refined spline spaces for the problem discretisation.

We chose to avoid both the level set technique and the element interpolation function enrichment typical of X-FEM as, apart from implying more complex algorithms, these techniques require an image-segmentation stage that, in most cases, involves

considerable human intervention. As in FCM, we reduce the image segmentation burden by superimposing a Cartesian mesh on the image and introduce all the information provided by the image at the element integration stage. In contrast to FCM, we use h-adaptivity to refine the mesh. Doing so, we simplify the methodology and act in accordance with the numerical results, shown in Section 2.3.1, which suggest to use low order interpolation functions for the problem under consideration.

Objectives

In this thesis we address the problem of creating numerical models from medical images for the linear elasticity problem. In particular our objective is to develop and validate procedures for the reduction of the human intervention required at the modelling stage as well as the overall computational cost of the simulation. We consider problems over domains defined by images, focusing on the structural analysis of bone tissue.

In particular our contribution aims at:

- reducing of the modelling burden by making the mesh generation automatic;

- introducing the local pixel elastic properties into the numerical model;

- simplifying the process of coupling image and CAD based models, necessary, for instance, in the case of *in silico* validations of implants;

- reducing the computational cost at the integration and resolution stages.

These aspects have been tackled by developing an image-based version of the Cartesian grid Finite Element Method (*cg*FEM) [32] and in particular by:

- directly superimposing *cg*FEM hierarchical structure on images and using heterogeneity indicators to guide the automatic mesh adaptation;

- applying special integration schemes which include all the information provided by the image;

- using geometry-independent elements which can easily take into account information from different sources such as CADs and CT scans.

- taking advantage of the special features of Cartesian grids.

After this short introduction, we introduce the main characteristics of image-based *cg*FEM, proposed in this thesis, in Chapter 2, which contains results about the method behaviour for problems with different material property distributions, orders of the interpolation functions and integration schemes. Chapter 3 shows applications of *cg*FEM to the numerical characterisation of the overall elastic behaviour of solid foams from μCT scans. Chapter 4 introduces the problem of prosthetic device simulation through a number of examples which include the calculation of natural frequencies to evaluate the stability of future implants.

Chapter 2

Image-based *cg*FEM

This chapter presents the image-based *cg*FEM developed in this thesis. The method is based on the geometrical *cg*FEM, which will be introduced first.

2.1. The geometrical *cg*FEM

The Cartesian grid Finite Element Method (*cg*FEM), is a numerical technique which uses a hierarchical set of nested regular Cartesian grids to create an adaptive geometry-independent calculation mesh of non-conforming regular quatrilaterla/hexahedral elements. In this thesis this method is applied for the solution of structural problems in linear elasticity. Originally, *cg*FEM main purpose was addressing issues related to the high cost of meshing and re-meshing, a well as the cost of stiffness matrix integration in FE models. These are especially relevant in iterative procedures, for instance in shape or topological optimization.

In geometrically defined problems, the domain is available as a CAD model. This is intersected with a quadtree/octree hierarchical structure of Cartesian grids, see Figure 2.1, to obtain the corresponding *cg*FEM model. The FE calculation is carried out on a mesh consisting of elements belonging to different levels of the hierarchical structure. This makes mesh adaptivity particularly fast and cheap as all the elements and their mutual relationships are known *a priori*.

We call this *discretisation mesh* to distinguish it from the *integration mesh*. These do not coincide, in contrast to standards FE. On the one hand, the discretisation mesh is the support of the FE interpolation functions and, due to the regular element shape the Jacobian is constant at each element as there is no possibility of element distortion during the meshing and remeshing processes. On the other hand, the integration mesh consists of all the subdomains necessary for the numerical integration of the element stiffness matrix, that is for the definition of the Gauss point locations. The distortion of the integration subdomains does not affect the accuracy of the method.

The intersection of the hierarchical structure with the problem geometrical domain makes it possible to distinguish three classes of elements depending on their position as they can lie in the bulk, on the boundary or outside the problem domain. The last are discarded. It is worth mentioning that, even in *h*-adapted *cg*FEM meshes, the elements are geometrically similar.

Due to this similarity, all the inner elements on a domain, homogeneous from the elastic properties point of view, have proportional stiffness matrices with scale factors only depending on the difference between refinement levels [33]. Consequently, it is possible to compute the stiffness matrix of one inner element only and scale it to obtain those of all the other inner elements with the same material properties.

In contrast, the elements cut by the geometrical boundary are decomposed into triangular or tetrahedral integration subdomains, for 2D ad 3D problems respectively, to properly capture the geometry near the boundary during the integration stage, see Figure 2.2, therefore, their stiffness matrices have to be computed separately.

At this stage it is possible to take into account the geometrical boundaries with different degrees of approximation: linear, as shown in Figure 2.2, with higher polynomial degrees or exact using trasfinite interpolation in 2D [32] or a NEFEM inspired integration technique in 3D problems, [34].

As shown by Figure 2.2, external boundaries can be considered a special case of interface between domains of different material properties.
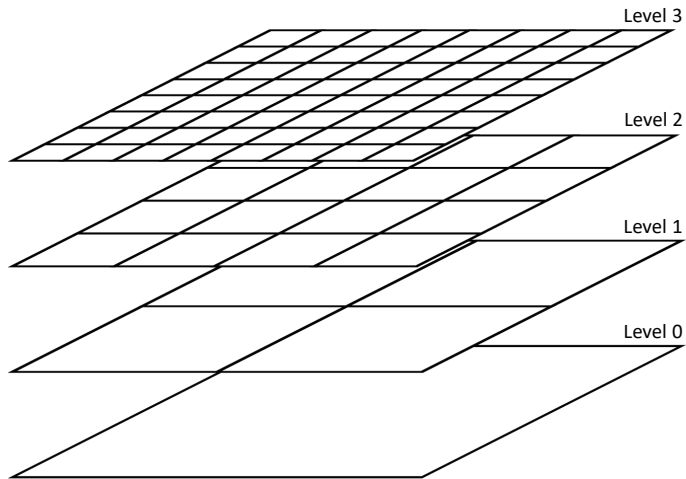
(a)
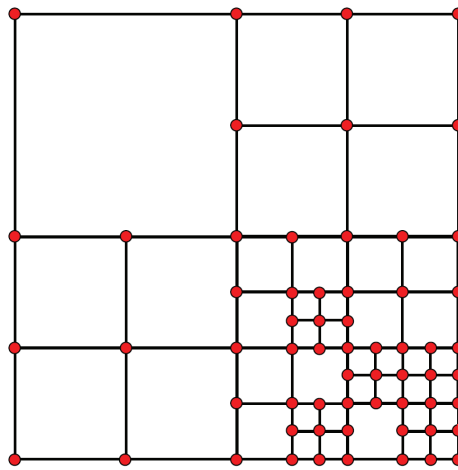
(b)

Figure 2.1: *cg*FEM mesher. (a) First levels of the hierarchical structure of nested Cartesian grids; (b) Example of non-conforming Finite Element mesh with *cg*FEM.
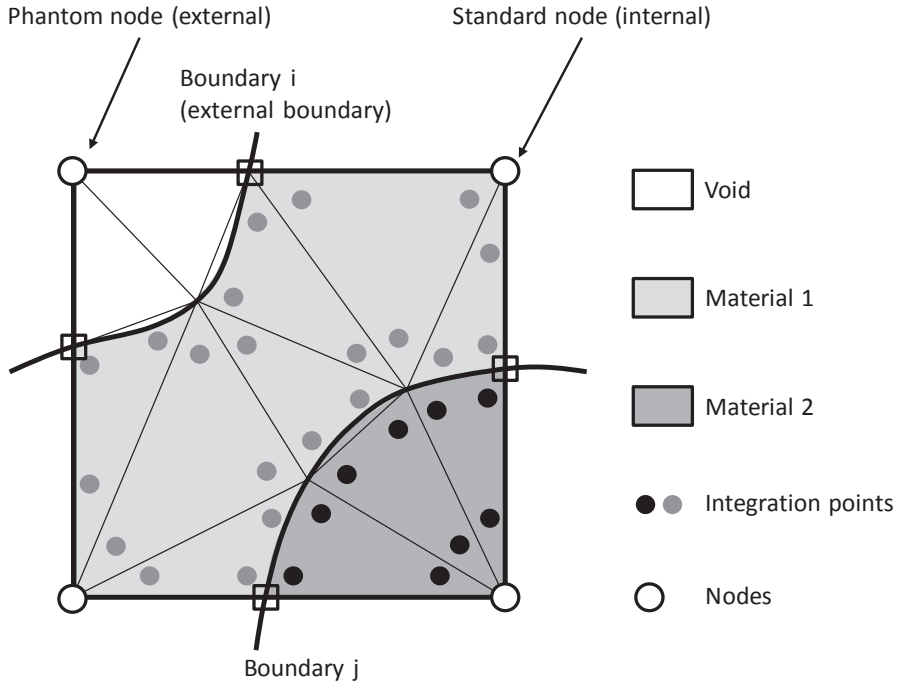
Figure 2.2: Triangular integration subdomains of *cg*FEM element containing geometrical boundaries.

It is worth highlighting that, whereas the discontinuity is taken into account in the integration scheme, the strain discontinuity at the interface is not included in the model since the element shape functions and their derivatives are continuous inside the element domain.

Substituting the discontinuous material behaviour with a continuous one can be seen as a material homogenisation process at the element level.

The computational effort required to create the stiffness matrix is therefore proportional to the number of elements cut by the boundary. Consequently, the problem complexity associated to the evaluation of element matrices is reduced by one dimension.

In addition, once the system matrix is assembled, it is possible to reduce the computational cost associated to its resolution by properly reordering the system DOFs. This can usually be done in most algebraic systems of equation, nevertheless

in the case of *cg*FEM this reordering is faster and more efficient due to the *a priori* knowledge of the mesh connectivity and hierarchy, see [32].

The first step of the meshing process is the creation of a uniform Cartesian mesh. Afterwards, this is firstly refined on the basis of geometrical criteria without the necessity to solve the FE problem, and, finally, in an iterative process following an *a posteriori* Zienkiewicz and Zhu error estimator, [35] and [36] based on the use of a recovered stress field obtained by an enhanced version of the superconvergent patch recovery (SPR) technique, [37] and [38].

In geometry-based problems, the Dirichlet boundary conditions are enforced on the geometrical boundary in a weak sense via stabilized Lagrangian multipliers, [39] and [40].

Next section explains the element integration procedures used in *image-based cg*FEM. Even though these differ from the integration technique of the *geometry-based cg*FEM, nonetheless they are based on the concept of properly integrating the element matrices while keeping a standard continuous function approximation even for heterogeneous elements as those on the boundaries.

2.2. The image-based *cg*FEM

In this section we propose *image-based cg*FEM as a methodology to create FE models of objects defined by images. We will first describe the element integration technique in Section 2.2.1. The kind of relation used to relate material properties and pixel intensity values is treated in Section 2.2.2. Finally, in Section 2.2.3, we will introduce a mesh refinement strategy based on element heterogeneity.

2.2.1. Element integration

When *cg*FEM is applied to image-based problems, once the structure of Cartesian grids is superimposed on the image, it is no longer possible to distinguish elements in the bulk from those on the domain boundary, see Figure 2.3a, as this is available

as a distribution of image grey levels instead of a well defined geometrically contour. Under the assumption that it is possible to properly assign local material properties to the pixels according to their colour level, all the elements in the mesh contain, in the general case, heterogeneous materials as in the case of the elements on the boundary in standard geometrical *cg*FEM, se Section 2.1. Hence, these elements will be treated in a similar way, that is by properly integrating the element stiffness matrix $\mathbf{k}^e$ (2.1), which homogenizes the elastic behaviour of the different domains, as in the case of Figure 2.2. (Note that, following this approach, not only $\mathbf{B}$, the matrix containing the shape function derivatives in linear elasticity, depends on the spatial coordinates $\mathbf{x}--$ but also $\mathbf{D}$, the linear Hooke's law matrix, does. As a consequence, $\mathbf{k}^e$ is evaluated as:

$$\mathbf{k}^e \quad = \quad \int_{V^e} \mathbf{B}^T(\mathbf{x})\mathbf{D}(\mathbf{x})\mathbf{B}(\mathbf{x})dV \tag{2.1}$$

In the process, all the pixels contained in the elements are taken into account at the integration stage. As opposite to the procedures used for this purpose in conforming meshes, in the Cartesian environment this is straightforward because, as explained later in this Section, the mesh creation guarantees that an integer number of pixels is contained in each element. The evaluation of the element integrals can be carried out by adopting different numerical quadrature rules. In this thesis we take into account three possibilities:

- a Riemann sum inspired integration quadrature, see (2.2), in which an integration point is located at the centre of each pixel i with constant weight, see Figure 2.3b, and the weight w_i, corresponding to each pixel/integration point is constant for all pixels and equal to the relative area of each pixel in the element;

$$\mathbf{k}^e = \sum_{i=1}^{IP} \mathbf{B}^T(\boldsymbol{\xi}_i)\mathbf{D}(\boldsymbol{\xi}_i)\mathbf{B}(\boldsymbol{\xi}_i) \mid \mathbf{J}(\boldsymbol{\xi}_i) \mid w_i \tag{2.2}$$

- a domain decomposition quadrature, see (2.3), in which a Gauss integration scheme is applied at each pixel considered as homogeneous from the point of
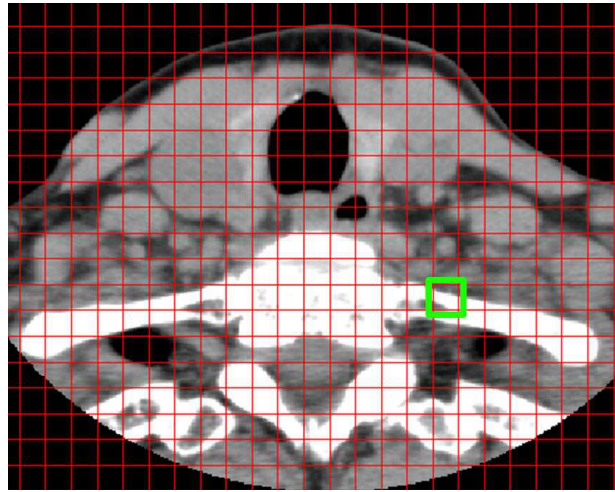
(a)
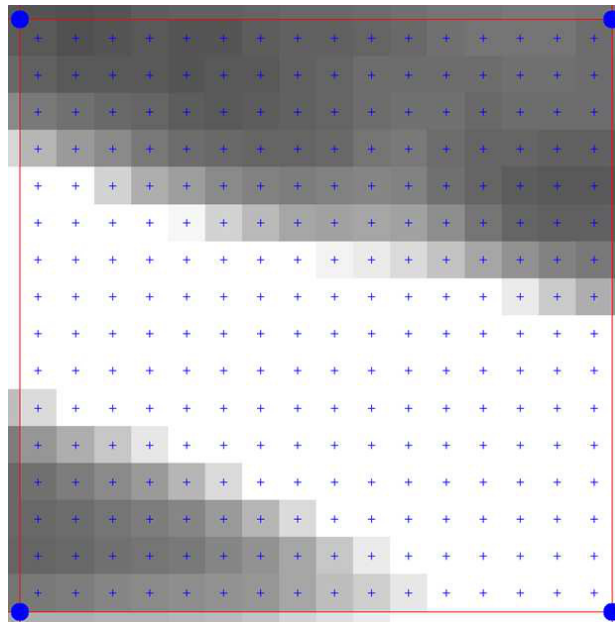
(b)

Figure 2.3: Uniform *cg*FEM mesh. (a) Detail of neck CAT scan cross section immersed in uniform mesh; (b) Magnification of the element highlighted in green.

view of the elastic properties;

$$\mathbf{k}^e \quad = \quad \sum_{i=1}^{IS}\sum_{j=1}^{IP}\mathbf{B}^T(\boldsymbol{\xi}_{ij})\mathbf{D}_i\mathbf{B}(\boldsymbol{\xi}_{ij}) \mid \mathbf{J}(\boldsymbol{\xi}_{ij}) \mid w_j \tag{2.3}$$

- a least square-based recovery of the elastic property field, see (2.4) and (2.5), which makes it possible to integrate with the proper Gauss quadrature a continuous function on the element domain.

The Riemann sum option is generally less accurate compared to the Gauss quadrature, in addition its accuracy depends on the level of mesh refinement as the number of pixels per element and, consequently, of integration points decreases when the elements are split.

In order to quantify this loss of accuracy, in the following sections, we compare it with the subdomain decomposition scheme which uses the proper number of integration points independently from the element level in the hierarchical structure. This is similar to the solution presented in [41] for *image-based* FCM.

The downside of the subdomain decomposition scheme, compared to the Riemann sum one, lies in the higher number of integration points required.

In both of these two methods, the number of integration points is kept constant over the mesh refinement since all the pixels are integrated with the same quadrature rule, therefore, in an h-adapted mesh, elements from different levels of the Cartesian hierarchical structure contain a different number of IP making the process harder to parallelise.

In the third solution, the material property samples are fitted in each element by the polynomial $\mathbf{p}(\boldsymbol{\xi})^T\mathbf{a}_e$. The column vector $\mathbf{p}$ represents the polynomial basis of a given order, $\mathbf{p} = \{1\ \xi\ \eta\ \zeta\ \xi^2\ \eta^2\ \zeta^2\ \xi\eta\ \xi\zeta\ \eta\zeta\ ...\}^T$, and the column vector $\mathbf{a}$ contains the polynomial coefficients for each element e. The recovered material property field is piecewise continuous and discontinuous at the interface between neighbouring elements. The polynomial $\mathbf{p}(\boldsymbol{\xi})^T\mathbf{a}_e$ can be least squares fitted to the material properties P_i at the centre of the pixels $\boldsymbol{\xi}_i$ by the minimization of the functional Π with respect

to each one of the polynomial coefficients a_j as follows:

$$\min_{a_j} \Pi = \min_{a_j} \sum_{i}^{NP} (P_i - \mathbf{p}(\boldsymbol{\xi}_i)^T \mathbf{a})^2 \tag{2.4}$$

This leads to the system of linear equations

$$\left[\sum_{i}^{NP} \mathbf{p}(\boldsymbol{\xi}_i)\mathbf{p}(\boldsymbol{\xi}_i)^T \right] \mathbf{a} = \sum_{i}^{NP} P_i \mathbf{p}(\boldsymbol{\xi}_i) \tag{2.5}$$

which has to be solved to compute the coefficient column vector $\mathbf{a}$ for each element in the mesh.

The element stiffness matrix can be finally computed, see (2.2), by using the proper Gaussian quadrature on the basis of the degree of the integrand. Due to the regularity of *cg*FEM meshes and the fact that the set of Gauss points used for the integration is the same, in local coordinates, for all the elements in the mesh, we can compute the $\mathbf{B}$ matrix only once for a given level and scale it for all the elements in the mesh, [42]. In contrast, in the previous methods, it is necessary to compute a $\mathbf{B}$ matrix per level. Figure 2.4 shows a schematic representation of the three methods.

If a mesh contains elements from the 4th level of the Cartesian grid structure and each of them contains $32 \times 32 \times 32$ pixels, the number of integration points for which it is necessary to compute the shape function derivatives is 32768 in the case of the Riemann sum. The number of integration points per element is 8 times higher for the decomposition in subdomains when the shape functions are linear whereas it is only 27 if the LS fitting is used.

Let's consider the previous case of a mesh only containing 4th level elements. If the mesh is *h*-refined with 5th level elements of $16 \times 16 \times 16$ pixels the $\mathbf{B}$ matrix has to be computed at 4096 additional locations. Introducing level 6, 7 and 8 element increases the number of locations by 512, 64 and 8 respectively, reaching an overall number of 37448. Independently of the mesh refinement, the LS technique, continues to require the computation of the $\mathbf{B}$ matrix at 27 positions only.

The least square fitting alone cannot guarantee neither the stability of the method nor the compliance with the energy conservation principles. This is due to the fact

Riemann sum

(a)

Integration subdomains

(b)

Fitting-based

(c)

○ Nodes   ■ Integration point position   ● Elastic property value
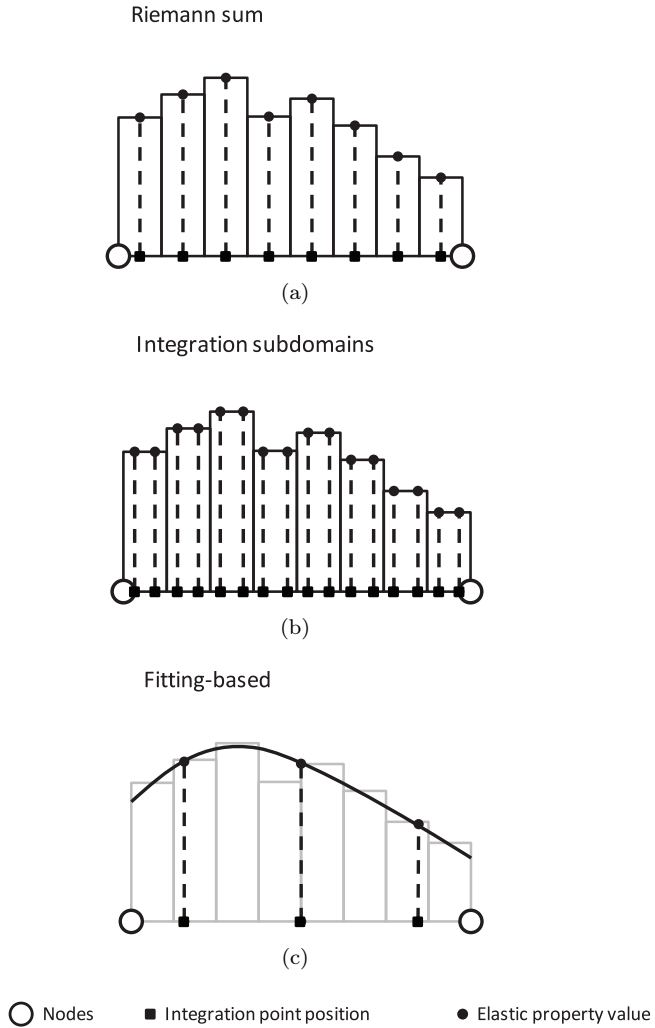
Figure 2.4: Schematic 1D representation for the integration techniques presented in Section 2.2. (a) Riemann sum; (b) Decomposition in integration subdomains; (c) Fitting-based integration.

that, in principle, no restriction is enforced which guarantees physical admissibility of the extrapolated values.

The material model considered in this thesis is assumed to be isotropic at the IP level. Its behaviour is defined by two independent parameters. If we use the standard engineering elastic constants, the value is admissible only if positive, in the case of the Young's modulus, and between 0 and 0.5 in the case of the Poisson's ratio.

In order to guarantee the uniqueness and physical admissibility of the solution, the unacceptable values obtained after the extrapolation are detected and the LS coefficient scaled to keep the same average value but with values in the admissible range.

For reasons which are made clear below, in Section 2.3, we propose to use the *image-based cg*FEM with linear shape function as well as linear fitting to avoid a series of drawbacks which appear if higher order functions are used together with a pixelised domain description. It is pointless to increase the LS fitting order with low order shape functions. It only increases the computational cost (more IPs) and makes unphysical elastic property values more likely to appear and harder to correct.

2.2.2. Local material properties

CT scan pixel values are expressed in Hounsfield units (HU), these measure the local average X-ray absorption of the material volumes corresponding to the pixels. Typical HU ranges for the main biological materials can be found in the literature. In the field of bone mechanics, an intense research has been carried out to relate bone Hounsfield values to corresponding elastic properties. In most of the cases two-step non-linear relationships (between HU scale and apparent mineral density and between apparent mineral density and Young's modulus) have been proposed, see, for instance, [43], [44] and [45]. The purpose of this thesis does not include the obtention of reliable HU-E relationships, as it mainly focuses on the numerical aspects of the method. Therefore, in the simulations that follow we use various kinds of 2D and 3D images, trying when it is possible to extract material data from the literature.

In most of the cases, especially when an anatomical site-specific law, [46], is not available, we propose to associate given pixel values to the average elastic properties found in the literature and then linearly interpolate the values in between, obtaining a piece-wise linear functions as schematically shown in Figure 2.5. At the level of the
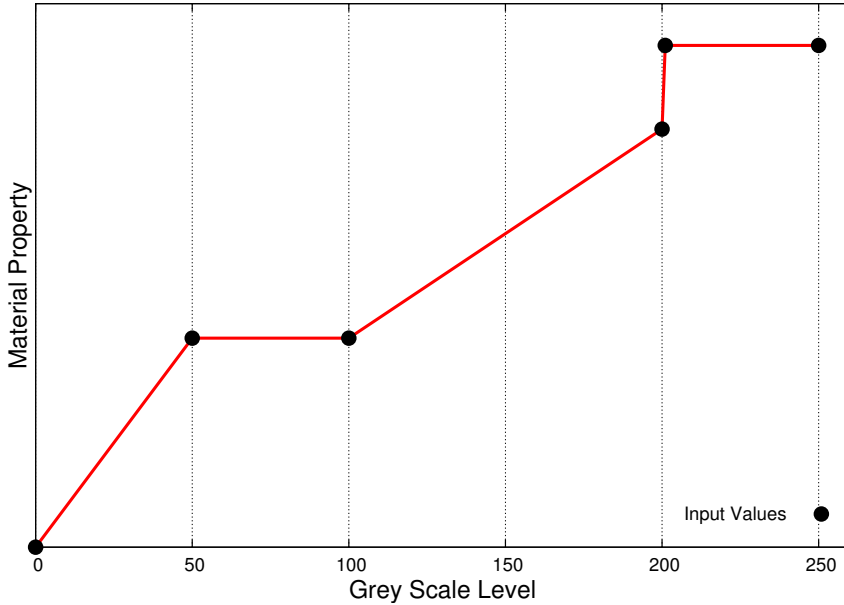
Figure 2.5: Schematic representation of the relation between grey scale pixel values and material properties.

pixel, we consider linear isotropic material models. Doing so we only let anisotropy appear at the macroscopic level as a result of the image heterogeneity.

2.2.3. Mesh adaptivity

To prevent the method from performing a too aggressive homogenisation, we propose to h-adapt the mesh according to the pixel heterogeneity in the first place, before any FE calculation is carried out. This process is fast and inexpensive, since it is based on the Cartesian grid hierarchical structure, in which the nth-level is the result of splitting each element of the grid of the $(n-1)^{\text{th}}$-level in two new elements along each direction. Due to this procedure, each parent element can be divided into 2^D new elements, being D the problem spatial dimension.

As shown in Figure 2.6a, an initial uniform grid is superimposed upon the image. Afterwards, the mesh is refined through an iterative process. The element heterogene-

ity is evaluated at each step and used to choose the elements to split, an additional check and refinement of their neighbours makes it possible keep a maximum difference of one level between adjacent elements.

The user has to provide the starting and maximum allowed mesh levels as well as the parameters which define the refinement criterion. The process leads to a final mesh as the one shown in Figure 2.6b.

We propose to use the index I_R^e, defined in (2.6) as an indicator of the element heterogeneity, being α_i^A the value of the Young's modulus E assigned to the pixel i within the domain A.

$$I_R^e = \frac{\Delta\alpha^{\Omega^e}}{\Delta\alpha^{\Omega}} = \frac{max(\alpha_i^{\Omega^e}) - min(\alpha_i^{\Omega^e})}{max(\alpha_j^{\Omega}) - min(\alpha_j^{\Omega})}; \tag{2.6}$$

The heterogeneity evaluation method is rather general, in the sense that it could be easily extended to anisotropic material models by computing an I_R^e-like index for each independent parameter which defines its elastic behaviour and use then these indices to define a mesh refinement criterion.

In the following, for simplicity, all the meshes are refined evaluating the Young's modulus heterogeneity only. It is reasonable as the main interest in this thesis is in the mechanical behaviour of bone or metallic foams. In the former case, the vast majority of the relationships between stiffness and HU proposed take into account the Young's modulus only, usually, assigning a constant Poisson's ratio close to 0.3.

The mesh obtained at the end of the refinement process is strongly dependent on the problem, that is on both the image and the HU-E relationship. Nevertheless, in the vast majority of the simulations that have been carried out so far, $I_R^e \approx 0.2$ has provided adequate models. A study on the effect of the prescribed value of I_R^e is shown in Section 2.4.1.

The heterogeneity-based refinement presented so far is not based on any error estimator and is similar to the refinement, based on geometrical features only, which is carried out in *cg*FEM, before the computation of any FE solution. Since heterogeneity is not the only aspect which determines high values of the stress gradient it cannot substitute error estimation. Nevertheless, this method is inexpensive and provide good results with lower DOFs than a uniform mesh, as a consequence, it can, at
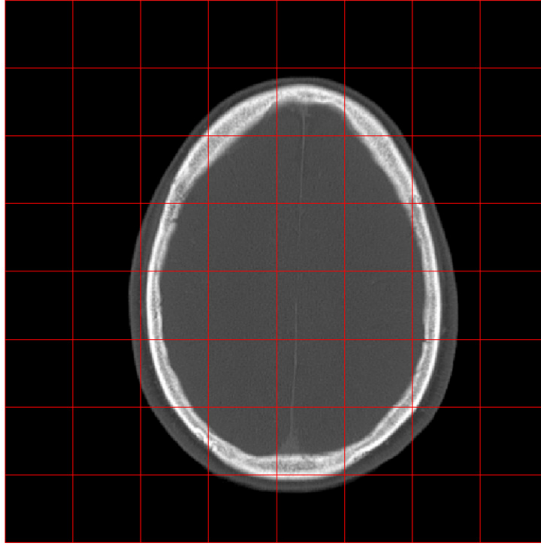
(a)
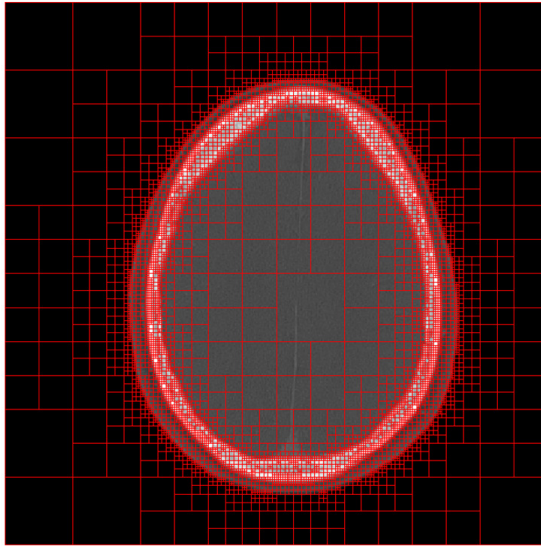
(b)

Figure 2.6: Mesh refinement process. (a) Initial uniform mesh; (b) h-adapted mesh.

least, provide a good starting point for further error estimation-driven mesh refining processes.

2.3. Validation

In the current section, we present some validation results obtained for synthetic 2D images. In Section 2.3.1 we mainly focus on the effect of the elastic property distribution and mesh size on the analysis results and on the image resolution influence in Section 2.3.2.

Later on we refer to the following expression for the error in energy norm, see [47]:

$$
e_r = 100\sqrt{\frac{\left|\int_{\Omega_{ex}} \boldsymbol{\sigma}_{ex}^T \mathbf{D}_{ex}^{-1} \boldsymbol{\sigma}_{ex} d\Omega - \int_{\Omega_h} \boldsymbol{\sigma}_h{}^T \mathbf{D}_{im}^{-1} \boldsymbol{\sigma}_h d\Omega\right|}{\int_{\Omega_{ex}} \boldsymbol{\sigma}_{ex}^T \mathbf{D}_{ex}^{-1} \boldsymbol{\sigma}_{ex} d\Omega}} = 100\sqrt{\frac{|U_{ex} - U_h|}{U_{ex}}} \qquad (2.7)
$$

in which $\boldsymbol{\sigma}$, U,Ω and $\mathbf{D}$ are stress, strain energy, problem domain and material compliance matrix. The subindexes $_{ex}$ and $_h$ identify the magnitudes for the exact problem and the FE one respectively, whereas the subindex $_{im}$ refers to the material properties as they are extracted from the image. The exact solution is calculated analytically, if its formulation is available as in the case of Section 2.3.1.1 and 2.3.2, otherwise it is substituted for a numerical solution obtained from a more accurate FE model, as in Section 2.3.1.2. It is worth mentioning that we use the absolute value in (2.7) to make it possible for us to represent the error norm in a logarithmic scale.

In the validation problems presented in this Section, the Poisson's ratio has a constant value of 0.3 and the stiffness matrices are computed using the integration subdomain (IS) scheme, see (2.3), to make the integration error negligible.

2.3.1. Effect of mesh size and elastic property distribution

In this section, we analyse *cg*FEM convergence behaviour in the case of uniform mesh refinement with different Young's modulus distributions for linear and quadratic FE interpolation. In order to better understand the effect of the element size, the refinement is carried out until obtaining meshes even finer than the corresponding bitmaps, i.e. considering several elements in each pixel, called sub-pixel meshes.

We consider three problems based on 128×128 pixel grey scale images. In the first one the bitmap is created from a geometrical model containing strong discontinuities, see Section 2.3.1.1, whereas in Sections 2.3.1.2 the images are obtained from analytical elastic property distributions.

2.3.1.1. A strong discontinuity case

The first case shows the convergence behaviour of the image-based model of a homogeneous pipe with a circular cross-section loaded by internal pressure under the hypothesis of plain strain condition according to Figure 2.7a and Table 2.1.

This problem is a typical benchmark in computational mechanics and has a well known analytical solution.

As usual, the model is simplified by taking advantage of its symmetry, therefore, only one fourth of the pipe is studied imposing convenient symmetry boundary conditions.

The image used in the simulation, see Figure 2.7b, was obtained by integrating a NURBs-based geometrical representation of the cylinder in a uniform mesh. This mesh had the same resolution as the desired resulting image. We evaluated the percentage area of each element covered by the cylinder and assigned a grey level proportional to this area percentage to this element. Considering each element as a pixel we created the grey scale image of the cylinder. To ensure full control on the conversion from vector to bitmap and all its approximation sources, we avoided to use standard graphic software, choosing instead to use geometry-based *cg*FEM to carry out the conversion from vector to bitmap representation. The procedure result is meant to mimic an idealised (noise free) X-ray scan, in which we assume that the
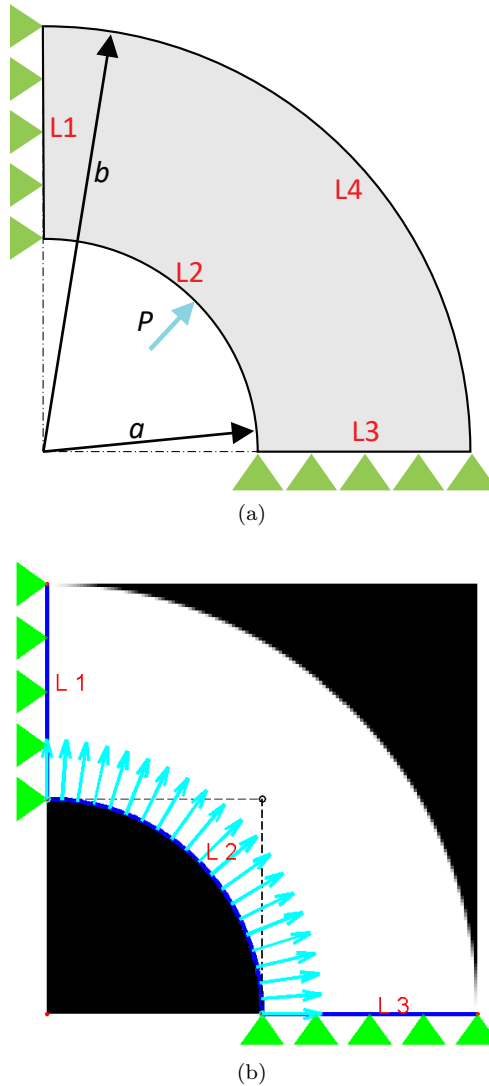
(a)

(b)

Figure 2.7: One fourth of pipe section with internal pressure in plain strain condition, extracted from [42]. (a) Geometrical model; (b) Corresponding bitmap model.

pixel colour only depends on the partial volume effect (PVE) (caused by the fact that a number of pixels represent partially empty volumes) and that the corresponding Young's modulus is proportional to the pixel value. The latter is implicit in our

choice to establish a linear relation between the Young's modulus and the grey scale computed by interpolating the values in Table 2.1.

a [m]	3
b [m]	6
P [MPa]	1

Material	E [MPa]	Grey level
Material 1	0	0
Material 2	1000	255

Table 2.1: Properties referred to the models in Figure 2.7.

Integrating a CAD representation over a uniform grid and converting the pixel values into grey scale, ensures that the only difference between the models lays in the inaccurate representation near the boundaries, which is pixel-size dependent.

The results in terms of strain energy and error are shown in Figure 2.8. The dash-dotted trace refers to sub-pixel meshes, in which each pixel is discretised into several elements, of the *image-based* problems. The super pixel meshes, where each element contains several pixels, are represented as solid lines. To distinguish the interpolation degree, the results obtained with linear and quadratic shape functions are represented with round and square markers respectively.

In the upper part of the graph we represent the FE and exact energy norms vs degrees of freedom for the linear and quadratic image-based models. The solid black horizontal lines represent the exact (solid) and estimated pixel-based (dotted) solutions. This estimated *pixel-based* reference solution is computed by solving the problem with a very refined uniform quadratic mesh (the level 9 of the nested Cartesian structure). Figures 2.9, 2.10 and 2.11 show how the exact solution of the pixmap (the stepped problem) is different from the solution of the corresponding geometrical problem. In particular, the effect of the discontinuities, due to the piece-wise constant distribution of elastic properties, is apparent in the magnification of the von Mises stress field close to the Neumann boundary for the image-based linear overkilled solution in Figure 2.11b, where each pixel has been discretised into 4×4 elements. The effect of the discontinuities near the boundary is consistent with the stress oscillations found in [48] and [49] for *pixel-based* FE models
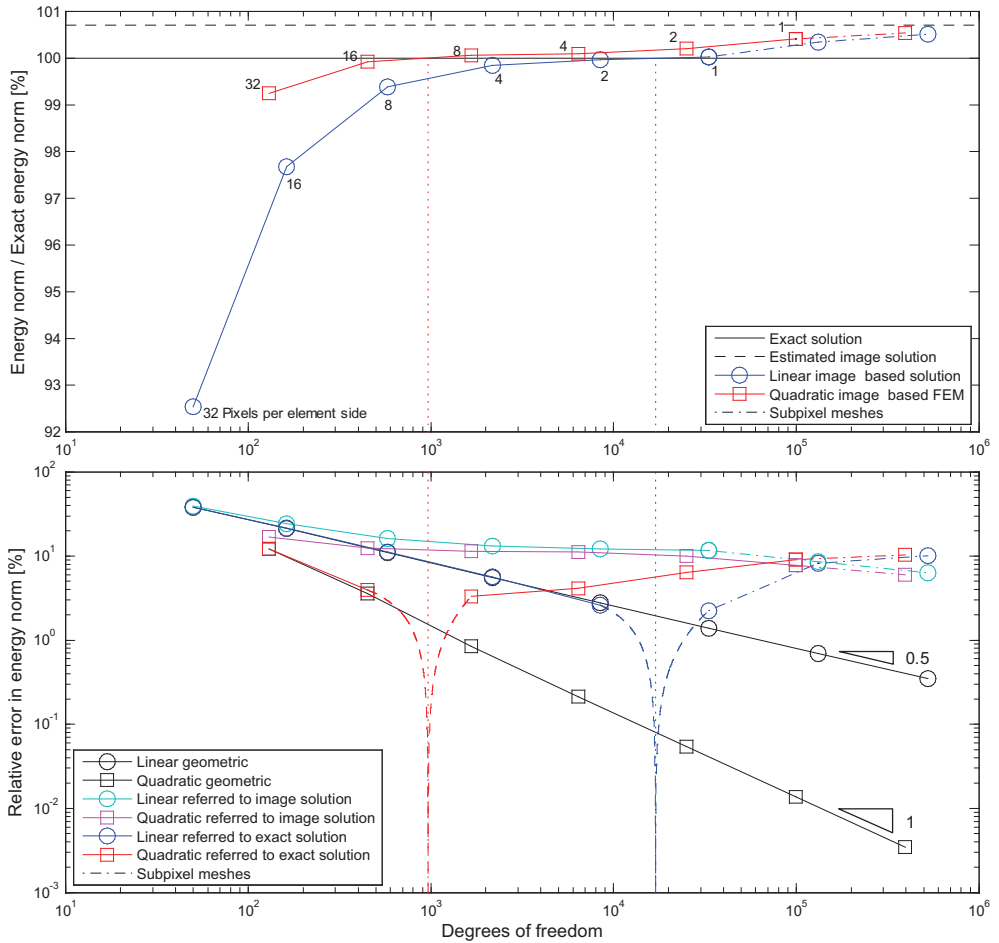
Figure 2.8: Relative energy norm and error convergence of the problem shown in figure 2.7 with uniform mesh refinement and image resolution of 128 × 128 pixels.

As it is to be expected, the blue and red curves in Figure 2.8 top do not converge to the analytical solution, but to the dotted line. In particular both linear and quadratic sub-pixel meshes diverge from the exact analytical solution as the refinement increases.

Since the discontinuous reference solution is higher in terms of strain energy than the exact one, the convergence curves intersect the exact solution. These intersections are marked by vertical dotted lines which are prolonged to the lower graph because
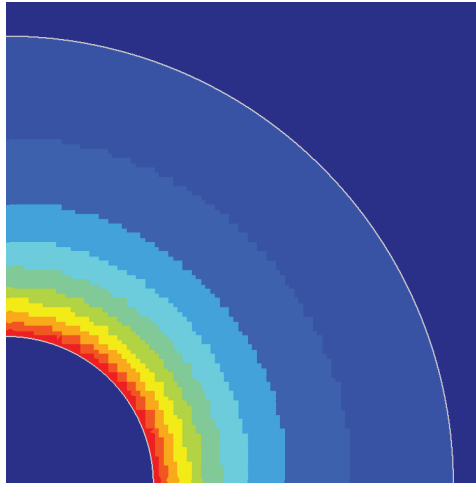
(a)
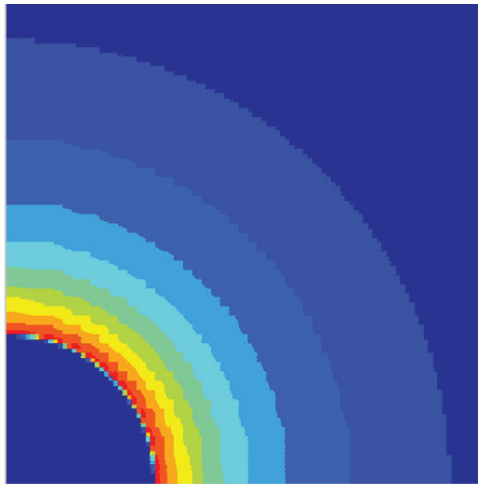
(b)

Figure 2.9: Von Mises stress field distribution for the geometry (a) and the 128 × 128 image-based (b) models in Figure 2.7a with linear interpolation functions and uniform level-6 mesh. The image-based model contains 2 × 2 pixels per element, see the blue curves in Figure 2.8.

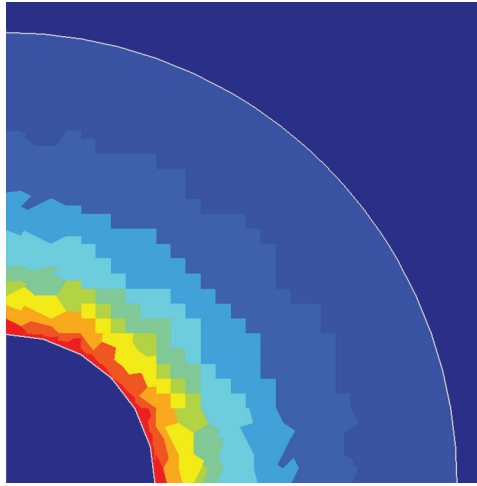(a)
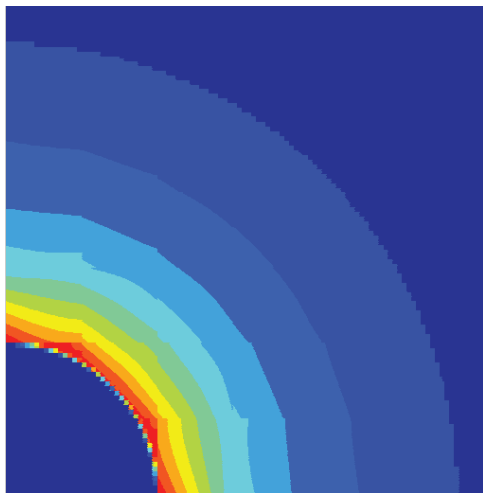

(b)

Figure 2.10: Von Mises stress field distribution for the geometry (a) and the 128 × 128 image-based (b) models in Figures 2.7a and 2.7b with quadratic interpolation functions and uniform level-3 meshes. The image-based model contains 16 × 16 pixels per element, see the red curves in Figure 2.8.
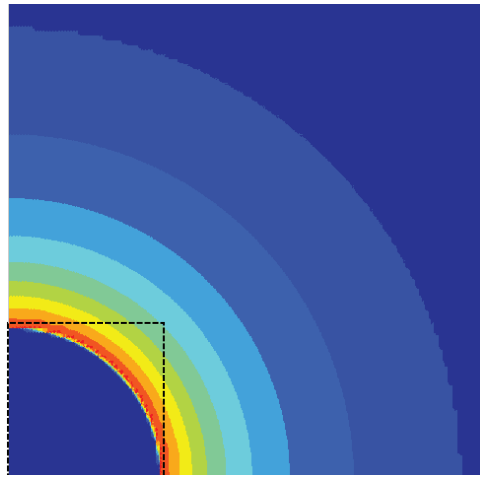
(a)
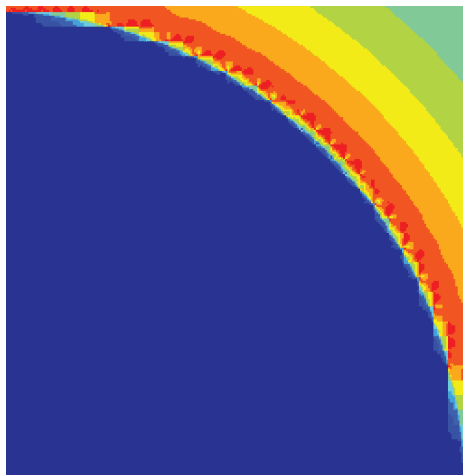
(b)

Figure 2.11: Overkilled solution for the 128 × 128 image-based model in Figure 2.7b with linear interpolation functions and a sub-pixel uniform level-9 mesh discretising each pixel with 4 × 4 elements, corresponding to the last points of the blue curves in Figure 2.8. (a) Von Mises stress field distribution; (b) Magnification of the Von Mises stress representation in area close to the Neumann boundary.

they are relevant to understand the error behaviour. This intersection occurs for coarser meshes in the case of quadratic interpolation.

The relative error in energy norm versus degrees of freedom is plotted in the lower graph of Figure 2.8. The solid black curves, characterised by the theoretical slope of 0.5 and 1 with respect to the number of degrees freedom, are the convergence results for the *cg*FEM geometric problem (for linear and quadratic FE interpolation order respectively). The blue and red curves correspond to the homologous ones in the upper graph. They refer to the image-based models with linear and quadratic interpolation functions and represent the strain energy value computed according to (2.7). As a consequence, in each of them an ideal point can be individuated which corresponds to the relative intersection in the upper graph and for which the error equals 0. The vertical dotted lines are, therefore, asymptotes for the error curves and the asymptotic branches are represented with a dashed trace. These 0 error points do not correspond to any actual mesh and will only appear if the singular image solution has a strain energy higher than the exact solution. They are the result of a strain energy compensation between the discretisation error and the modelling error since the former decreases throughout the refinement process, as in usual FEM, whereas the latter increases because finer meshes better capture the difference between the pixmap and the geometrical model.

As the number of degrees of freedom increases beyond the vertical asymptotes, the blue and red error curves significantly diverge from the respective geometrical FE solutions. As a consequence, they lose the theoretical convergence rates in logarithmic scale of 0.5 for linear and 1 for quadratic interpolation functions.

For linear interpolation functions, the geometry and image-based solutions behave alike provided that the elements are bigger than the pixels, however the solution clearly diverges for sub-pixel meshes (represented as dash-dot lines). In the case of quadratic elements, in contrast, this phenomenon starts appearing for coarser meshes because of the higher discretisation error reduction rate.

In the lower part of Figure 2.8 we also plot the image-based model error convergence curves with respect to the image solution, in cyan and magenta for linear and quadratic elements respectively. They result from substituting the exact strain energy U in (2.7) with the estimation of the pixelised model solution corresponding to the black dashed line in the upper graph. As the mesh is refined these curves tend to have the same slope. This behaviour is reasonable considering that the pixelised model is piecewise discontinuous and, as a consequence, the discontinuities prevent the convergence from reaching the theoretical values guaranteed for problems with

smooth solutions. The convergence slope is, therefore, determined by the discontinuities and is independent from the FE interpolation order. In this numerical example, the bitmap intrinsic inaccuracy in the domain boundary representation prevents the numerical solution from converging to the exact one with the increase of the number of degrees of freedom. In contrast, a limit appears for which the increase of computational cost due to the mesh refinement ceases to reduce the error with respect to the analytical solution. In this case, this limit can be set at around 2×2 and 16×16 pixels per element for linear and quadratic FE interpolation respectively. Refining the mesh beyond these values is uneconomical. The number of mesh levels suitable for the simulation is broader for linear FE interpolation functions, as a consequence, this polynomial order appears more suitable for the *h*-refinement of *cg*FEM.

2.3.1.2. A smooth Young's modulus distribution

Figure 2.12 shows a [-0.5, 0.5]×[-0.5, 0.5] plate under plane strain loaded with uniform unit tension on the upper side and symmetry boundary conditions on the lower and left sides. We consider two Young's modulus distributions, one polynomial expressed in (2.8) and another bi-sinusoidal, expressed in (2.9).
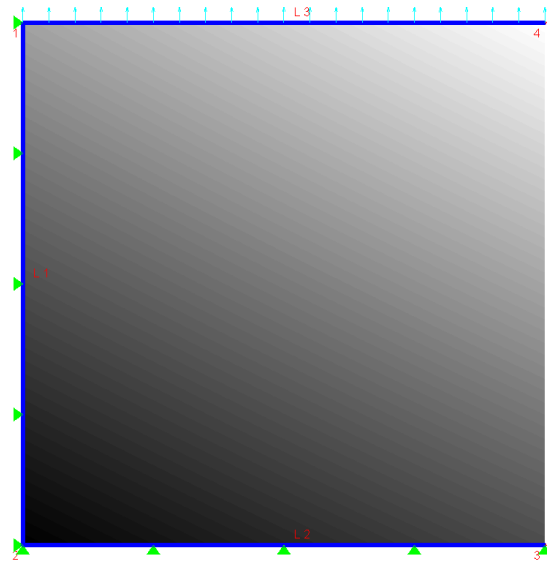
The Young's modulus distributions are shown together with the problem boundary conditions in Figures 2.12a and 2.12b respectively.

A 128×128 pixel image was obtained computing the analytical mean value of the Young's modulus in the area of each pixel and converting it into grey scale for each case.

$$E(x, y) = (y + 10)(x + 10)^2 \tag{2.8}$$

$$E(x, y) = (y + 10)(x + 10)^2(1 + 0.7 \sin(2\pi x) \sin(2\pi y)) \tag{2.9}$$

In the image-based models we established a linear relation between colour and stiffness in such a way that the minimum of the function in (2.8) and (2.9) on the problem domain corresponds to 0 and its maximum to 255 in grey scale.

(a)
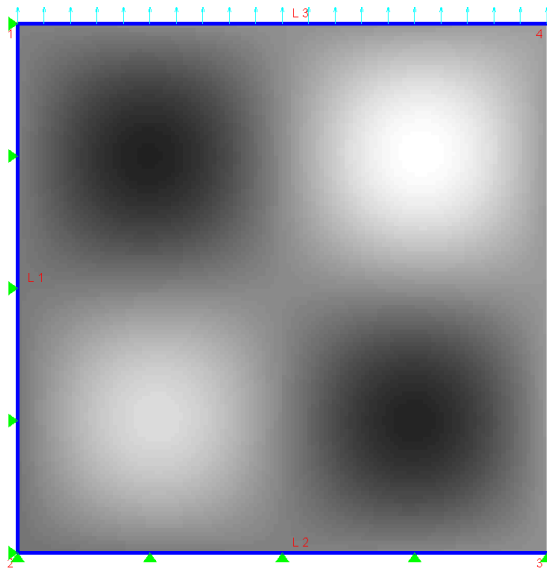
(b)

Figure 2.12: Square plate models representing the smooth variations of Young's modulus. (a) Polynomial distribution (2.8). (b) Bi-sinusoidal distribution (2.9).

Polynomial Young's modulus distribution

As in the previous section, the upper graph of Figure 2.13 compares the energy norm convergence of the image-based models for linear (blue) and quadratic (red) shape functions. The reference and the estimated image solutions are traced as solid
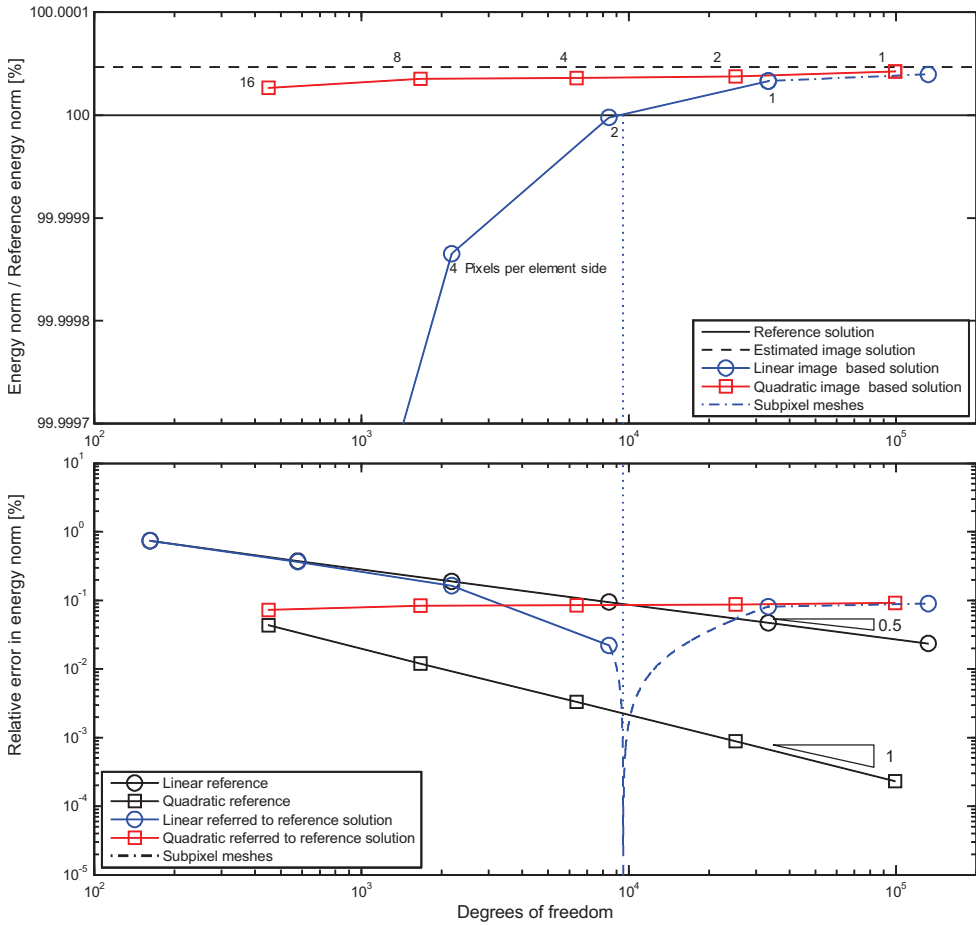

Figure 2.13: Relative energy norm (top) and error (bottom) convergence of the problem shown in figure 2.12a with uniform mesh refinement and image resolution of 128 × 128 pixels.

and dashed black lines respectively. These solutions were computed with quadratic

8 level meshes integrating the element stiffness matrix with the analytical Young's modulus distribution in the first case and with the value from the 128×128 bitmap in the second one.

The estimated reference strain energy for the pixelised model is higher than that estimated for the corresponding continuous property distribution, therefore the blue and red curves intersect the solid black line, similarly to Section 2.3.1.1.

In this case, the intersection is only represented for linear interpolation functions in Figure 2.13 for an element size that would be slightly smaller than 2×2 pixels per element. Note that, in this case, the convergence curve starts diverging from the theoretical behaviour of the continuous model for a coarser mesh than in the previous numerical example.

In the quadratic case it occurs for a coarser mesh outside the represented range. The intersection is marked and prolonged to the error graph and used to draw the asymptotic curve branches.

The reference curves for the continuous material property distribution converge at the theoretical rate for linear and quadratic interpolation functions.

In this case the estimated reference solutions for the continuous and the pixelised material distributions are closer than in Section 2.3.1.1, nevertheless the behaviour of the image-based simulation is similar for linear interpolation functions (blue curve). Instead, the discretisation error is negligible compared with the modelling one in the case of quadratic meshes (red curve) and, consequently, the solution directly converges to the modelling error.

Note that, for linear interpolation functions, the error convergence curve is less stable than in the previous cases and shows a certain divergence from the theoretical curve even at 2×2 pixels per element.

Bisinusoidal Young's modulus distribution

The results in Figure 2.14 refer to the problem shown in Figure 2.12b and were computed as in the previous case, see Figure 2.12a.

Differently from the previous numerical example, the estimated solution of the continuous model is higher, in terms of strain energy, than the estimated solution for the pixelised model. This results in the absence of any intersection of the blue and red
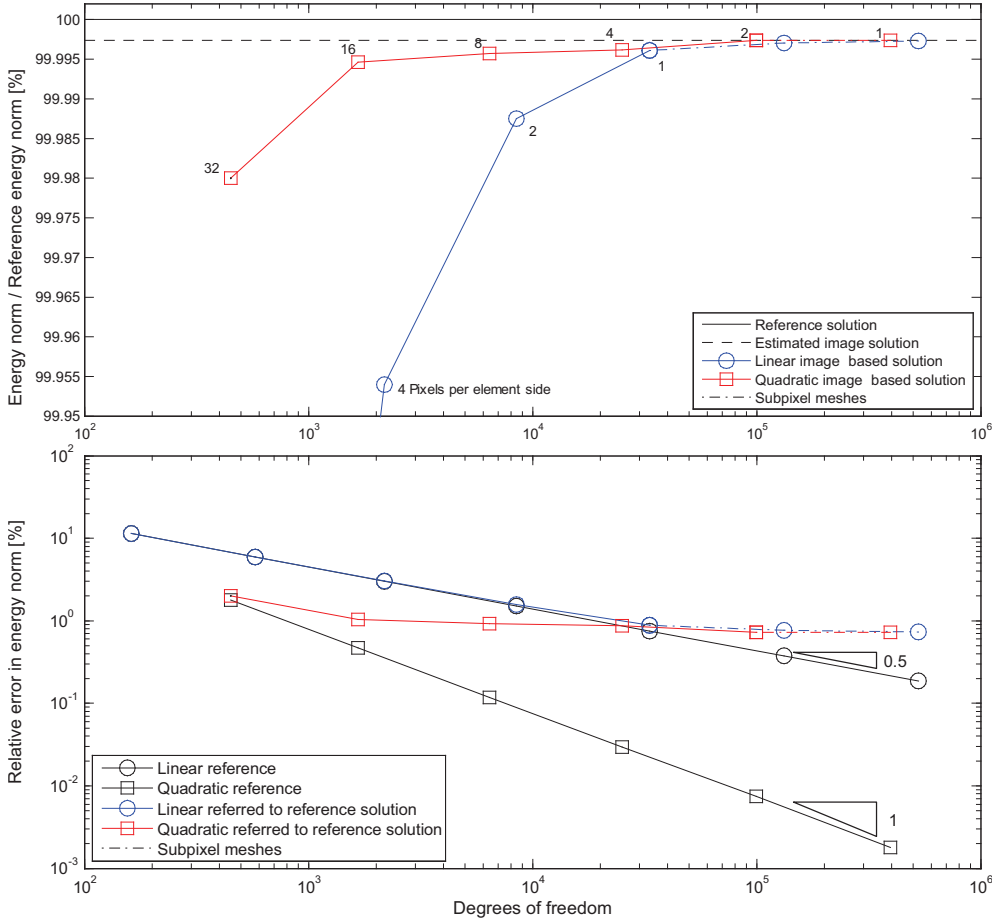
Figure 2.14: Relative energy norm (top) and error (bottom) convergence of the problem shown in figure 2.12b with uniform mesh refinement and image resolution of 128 × 128 pixels.

strain energy curves for the continuous model therefore no asymptotic branch can be found for the error evolution.

From the analysis of the three problems we deduce that the relationship between the exact solution of the exactly defined problems and that of the corresponding pixelised models is strongly problem-dependent.

As in the case of Figures 2.8 and 2.13, the error behaviour in the case of linear interpolation in Figure 2.14 follows the theoretical convergence path of the continuous model provided that the meshes are coarser than the bitmap. Once the mesh is refined beyond this limit the refinement stops enhancing the solution. The same happens for much coarser quadratic meshes.

As in the previews case, this is an intrinsic bitmap model error which cannot be reduced by either decreasing the element size or increasing the polynomial order of the interpolation functions. In contrast to the model in section 2.3.1, in this case the model error is related to the discontinuous elastic property representation instead of the boundary inaccurate definition.

2.3.2. Image resolution effect

In this section we analyse the effect of the image resolution on cgFEM results by comparing the convergence behaviour for uniform refinement of pixelised models of 128×128, 256×256, 512×512 and 1024×1024 pixels. These were obtained from the geometrical model in Figure 2.7a following the same procedure as in Section 2.3.1.1.

Figure 2.15 shows the evolution of strain energy versus the number of degrees of freedom for linear (p=1) and quadratic (p=2) interpolation functions. To make the comparison easier, the graphs are in the same scale. The convergence for the geometrically-defined cgFEM model is a solid black curve and the analytical solution is represented as an horizontal dashed line. In this case we only show results for super-pixel meshes with a minimum number of 1 pixel per element, that is, no sub-pixel mesh was used, in contrast to Section 2.3.1.1.

Figure 2.15 confirms the expectation that higher image resolutions guarantee results closer to the exact value of the non-pixelized problem. Similarly to Figure 2.8, all the curves intersect the exact solution and tend to higher strain energy values. These decreases getting closer to the exact value as the image resolution increases. Nevertheless, in this case the linear interpolation behaves better than the quadratic one as the corresponding strain energy values are closer to the exact solution.

The same behaviour can be observed in Figure 2.16 which shows the relative error in energy norm versus degrees of freedom. As in Section 2.3.1.1, the error was
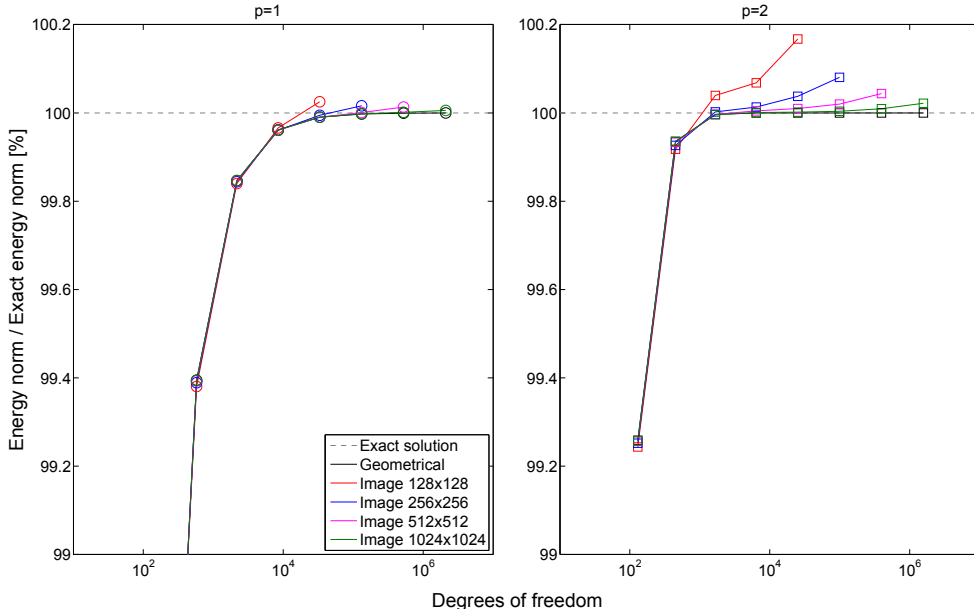
Figure 2.15: Relative energy norm for the model in figure 2.7 with different resolutions and uniform refinement. Left: linear interpolation. Right: quadratic interpolation.

calculated according to (2.7) using the benchmark problem exact solution. The black curves of Figure 2.16 represent the geometry-based *cg*FEM convergence curves with the theoretical slopes of 0.5 for linear and 1 for quadratic interpolation functions. We connected the error values obtained for images with different resolutions but the same number of pixels per element with thin black curves, which show the convergence behaviour of the pixelised problem to the analytical solution of the geometrical one as the image resolution increases.

A stable convergence is only recognisable in the cases in which the discretisation error is low compared to the modelling error, i.e. for linear meshes with one pixel per element and, more clearly, for quadratic meshes with eight or fewer pixels per element. The asymptotic part of the curves tends to appear earlier with respect to the most refined mesh, as the image resolution increases. Linear elements show proper behaviour until 2×2 pixels per element for all the considered resolutions. The case of quadratic elements is less stable and predictable as they lose the proper convergence rate for a variable number of pixels per element.
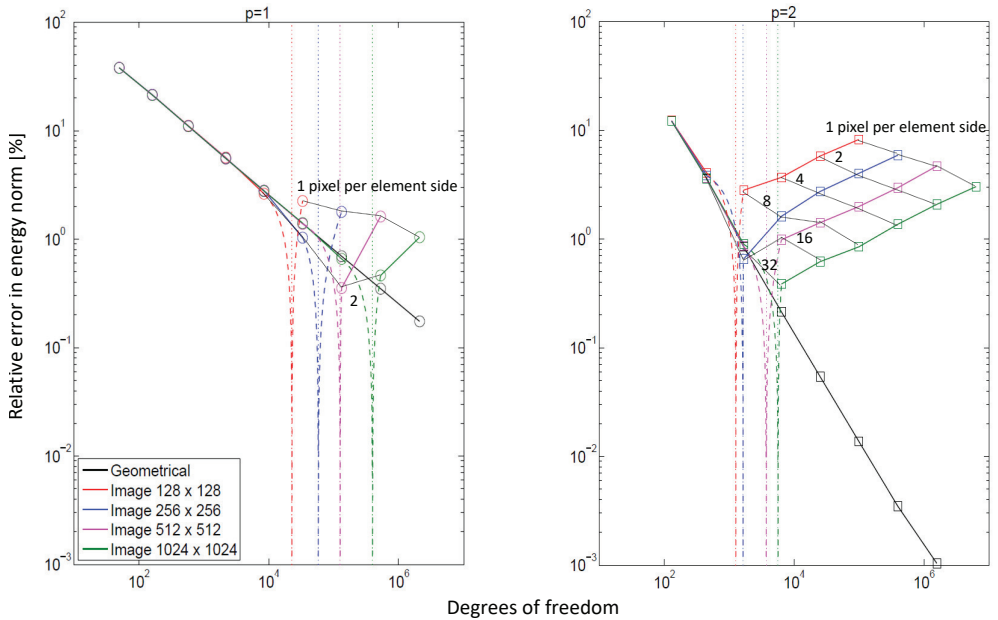
Figure 2.16: Relative error in energy norm for the model in figure 2.7 with different resolutions, degree and uniform refinement. Left: linear interpolation. Right: quadratic interpolation.

2.3.3. Conclusions

According to these results, a limit exists beyond which mesh refinement stops to be effective and looses the theoretical convergence slope. This is due to the fact that enriching the FE solution only affects the discretisation error whereas, because of the pixelized nature of the model, the model error remains unaffected as it only depends on the image resolution. Quadratic shape functions reach this limit for coarser meshes than linear ones, as they guarantee a lower discretisation error for the same element size, in problems characterised by smooth solutions.

Taking into account this phenomenon, we consider sensible to use linear interpolation functions for *cg*FEM as the convergence behaviour over the mesh refinement is closer to the theoretical one for geometry-based problems in all the numerical examples presented and, especially in the case of strong discontinuities, see Figure 2.15.

Quadratic shape functions can lead to models in which, the increase of the computational cost, degrees of freedom, increments the error in energy norm instead of reducing it.

With these and the previous results we can conclude that, in general, linear elements guarantee a reasonable convergence rate as long as the elements contain a number of pixels higher than what we can call the reliability limit that would be 2×2 or 4×4 pixels, depending on the problem and the image resolution. This implies that, if our target solution is the exact continuous one, which in the general case is unknown and cannot be estimated by FE refinement, it may be convenient to carry out simulations with super-pixel meshes. This also means that in traditional pixel-based methods the increase of computational cost does not correspond to the accuracy enhancement expected in geometry-based FE. In addition the availability of a higher number of valid mesh levels for which the theoretical convergence rate is kept makes linear interpolation function more suitable for h-refinement.

Taking into account these considerations, all the problems presented from now on are solved with linear elements.

2.4. Numerical results

In this section we present some simulations carried out on actual medical images by using image-based cgFEM with linear interpolation and meshes h-adapted on the basis of material property heterogeneity evaluations. Section 2.4.1 shows the influence of the heterogeneity index I_R^e index value on the mesh refinement. Section 2.4.2 will consider a 2D X-ray scan to study the performance of different integration techniques comparing uniform and colour-based h-adapted meshes. Section 2.4.3 will show an application in 3D for which the model is obtained from the CBCT scan of a human jaw.

2.4.1. Effect of the heterogeneity index on mesh adaptivity

Figure 2.17 shows the dependency of the mesh density on the heterogeneity index I_R^e, see (2.6), for the problems described in details later on in Sections 2.4.2 and 2.4.3. The mesh density is quantified by the index $\sqrt[D]{DOF/DOF_{max}}$.
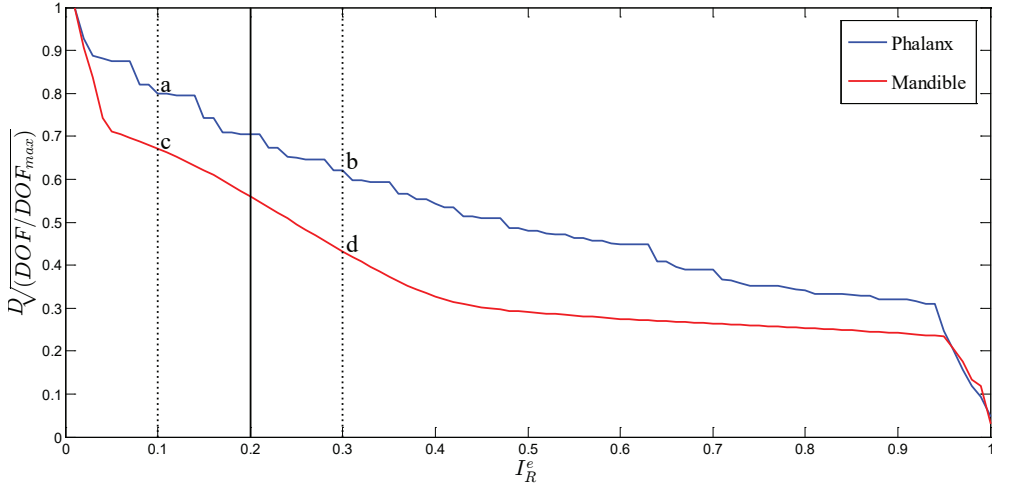

Figure 2.17: Effect of prescribed value of I_R^e on the number of degrees of freedom.

The definition of the density index makes it possible for us to obtain an estimator independent from the problem dimensionality D. The index is computed on the basis of the problem degrees of freedom DOF and DOF_{max}, the number of degrees of freedom of a corresponding *voxel-based* uniform mesh, in which each voxel corresponds to a Finite Element. The values referring to the problem in Section 2.3.1 are represented in blue whereas those for the models in Section 2.4.3 are in red.

Both curves show how a value of 0.2 for the index I_R^e leads to a range in which the mesh is at the same time sensitive to the parameter but also stable. This makes it possible for the user to have control over the final mesh.

Figures 2.18a to 2.18d show the meshes corresponding to the I_R^e values of 0.2 ± 0.1 highlighted in Figure 2.17.
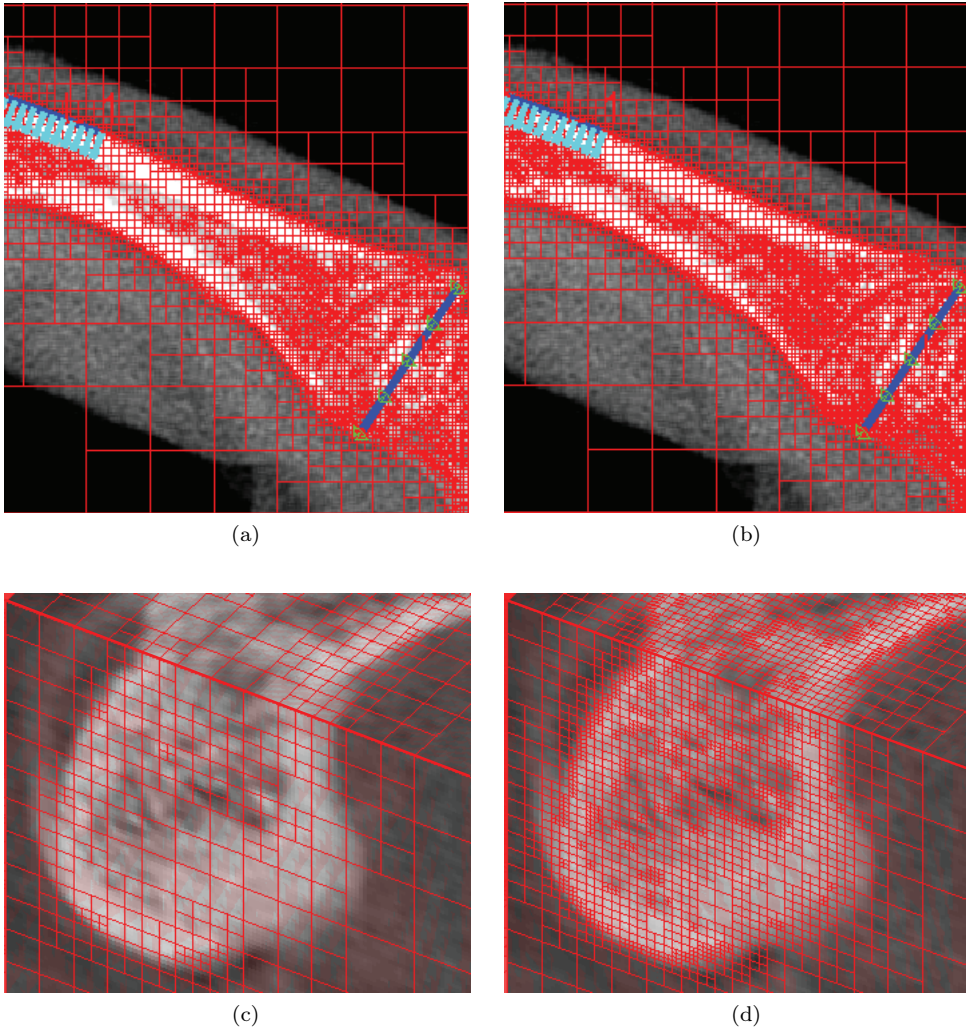
Figure 2.18: *h*-adapted refinement sensitivity. Phalanx model of Section 2.4.2. (a) $I_R^e = 0.3$; (b) $I_R^e = 0.1$. Mandible model of Section 2.4.3. (c) $I_R^e = 0.3$; (d) $I_R^e = 0.1$.

2.4.2. *cg*FEM application to 2D X-ray scan. Quadrature rule influence

The goal of this section is to evaluate the performance of the integration procedures described in Section 2.2.

To do so, we study the energy norm convergence for both uniform and h-adapted meshes obtained from an actual X-ray scan. This is the 2D phalanx model shown in Figure 2.19 simulated under plane strain.

We created a piece-wise linear, C_0 continuous relationship which provides the Young's modulus on the basis of the pixel intensity value. This function was obtained by interpolating the values extracted from the literature shown in Table 2.2, see [50] and [51]. All the pixels are assigned a constant value of the Poisson's ratio of 0.3.

| Material	Air	Muscle	Bone 1	Bone 2
Grey level	0	150	190	255
E [GPa]	0.000	0.645	14.000	14.200

Table 2.2: Material Properties referred to Figure 2.19.

Figure 2.19a shows the area of interest extracted from the X-ray scan whereas Figure 2.19b shows the curves defined on the model for the imposition of the Neumann and Dirichlet boundary conditions represented as cyan arrows and green triangles respectively. The former impose a uniform pressure value 1 MPa and the latter null displacement on the corresponding curves.

The h-adapted mesh was obtained by recursively splitting the elements for which $I_R^e \leq 0.2$, see (2.6), starting with an initial uniform mesh of level 4 and refining up to the 8th level of the Cartesian structure.

At each refinement step, the elements exceeding the assigned value of I_R^e are split into 4 elements. After that a recursive check is carried out on the neighbours of the new elements to identify level gaps of more than one level between contiguous elements. In these cases, the coarser elements are split in turn to guarantee that the difference between contiguous elements is of one level at the most, in the mesh used for the FE calculation.
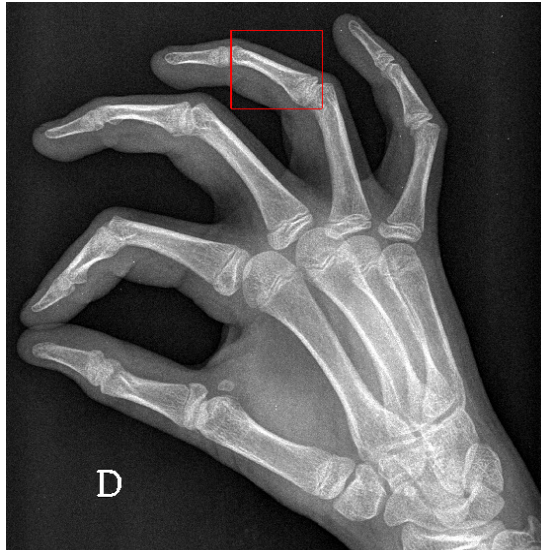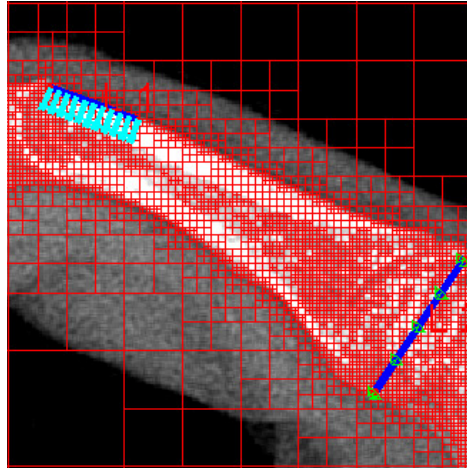
(a)
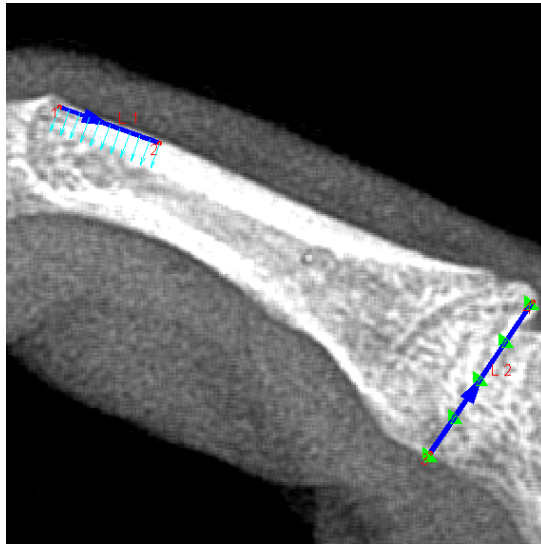
(b)

Figure 2.19: Phalanx simulation. (a) Hand X-ray image; (b) Phalanx image used in the simulation with the curves created for the boundary conditions imposition.

(a)
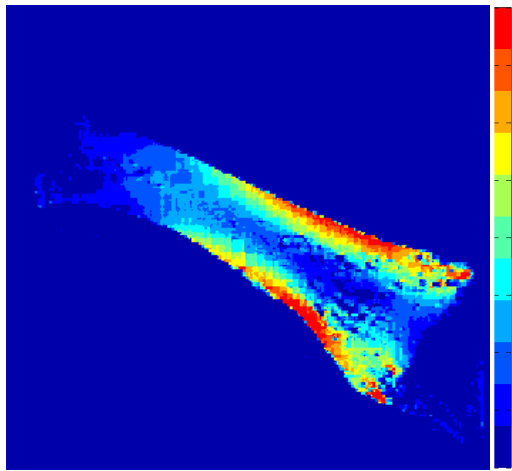
(b)

Figure 2.20: Phalanx simulation. (a) *cg*FEM mesh obtained by range evaluation guided *h*-adaptivity; (b) von Mises stress distribution in MPa.

It is worth highlighting how the heterogeneity-driven *h*-refinement manages automatically capturing the tissue boundaries despite the fact that no explicit segmentation was applied.
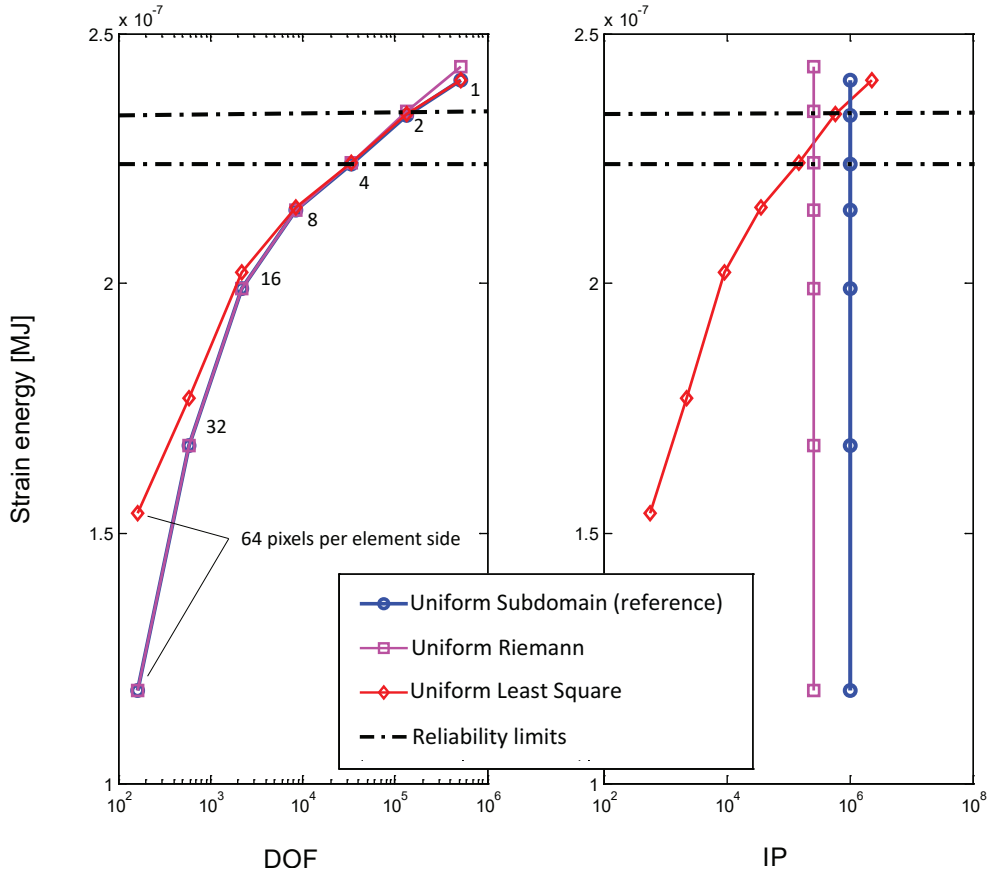
Figure 2.21: Strain energy versus the number of degrees of freedom (left) and integration points (right) for the uniform refinement of the model in Figure 2.18 with different integration schemes.

Figure 2.20a shows the von Mises stress field corresponding to the mesh in Figure 2.20b.

Although the model is not realistic, both because it is a 2D representation of a three dimensional body and because the X-ray absorption along the third direction makes it impossible to properly distinguish the different absorption rates, the stress distribution looks consistent with the body load condition.

Figure 2.21 shows the uniform refinement convergence for the quadrature procedures detailed in Section 2.2. The charts represents the strain energy versus the number of DOFs and integration points (IP) in the first and second charts respectively. On the one hand, the number of DOFs affects the hardware requirements and computational time necessary to solve the FE system of equations. On the other hand, the number of IPs has a strong influence on the computational cost at the integration stage.

The dash-dotted horizontal lines in Figure 2.21 represent the mesh refinement range (between 2×2 and 4×4 pixels per element) for which we observed in the previous numerical simulations that the solution diverges from the theoretical behaviour and the mesh refinements stops enhancing the result.

In Figure 2.22 we compare the behaviour of uniform (dashed) and h-adapted (solid) meshes in terms of strain energy versus degrees of freedom.

In both cases, the blue curves refer to the integration by subdomain decomposition, see (2.3), the red ones to the Riemann sum based integration scheme, see (2.2), and the magenta curves to the integration based on least square fitting, see (2.4) and (2.5).

Among the schemes presented in this chapter, the integration by subdomain decomposition is the one we take as a reference to study the convergence behaviour as it uses a Gauss quadrature appropriate to the polynomial degree of the integrand. In Section 2.3, we assumed that the divergence from the theoretical slope is not due to the integration technique but to the inaccuracy of the underlying pixelized model. Compared to the other quadratures presented, this scheme is the most expensive, in the general case, since the overall number of integration points it requires is the product between the number of pixels in the model and that of Gauss points per integration subdomain. This also implies that it is independent from the mesh refinement and, as a consequence, the computational cost associated to the element stiffness matrix integration is the same for coarse and refined meshes.

In this section the integration by subdomain decomposition is used as a reference to evaluate by comparison the behaviour of the other integration techniques proposed for the image-based cgFEM.

In the numerical examples shown in Section 2.3 the use of linear shape functions guarantees that the difference between the image and geometry-based models is negligible provided that the number of pixels in each element of the mesh is equal or higher than 4×4. In the cases analysed, the theoretical error convergence slope is
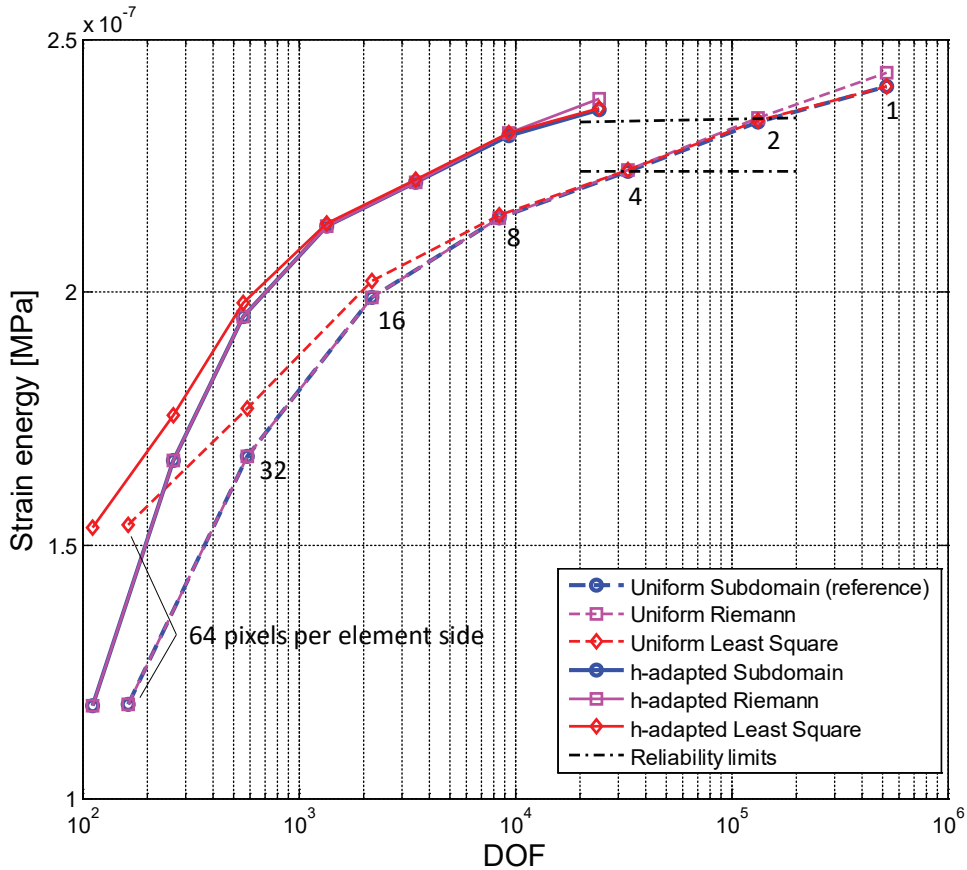
Figure 2.22: Strain energy versus number of degrees of freedom for uniform and h-adapted refinement of the model in Figure 2.21 for different integration schemes.

lost between 4×4 and 2×2 pixels per element. We consider these mesh refinement values as reliability limits. These are plotted as black dash-dotted horizontal lines corresponding to the strain energy of the model integrated by subdomain decomposition.

As shown in Figures 2.21 and 2.22, the Riemann and subdomain decomposition integration schemes have a similar accuracy below the upper reliability limit. Nevertheless, the Riemann scheme uses one-forth of the integration points of the domain decomposition scheme.

If the meshes are finer than the upper reliability limit, the strain energy overestimation of the Riemann quadrature is due to a loss of accuracy as it uses fewer and fewer integration points per element as the mesh gets finer.

In contrast, the least square-based integration technique provides strain energy values higher than the other two techniques for coarse meshes. The overall integration point number is lower than in the other techniques, in which it is constant, but it grows along the refinement process.

As shown in Figure 2.22, for h-adapted meshes we find the same pattern as in uniform refinement with the exception of a general reduction in the overall number of degrees of freedom which guarantees a lower computational cost for a similar level of strain energy.

The accuracy of the results provided by the LS technique is similar to the reference integration scheme for meshes contining less than 16×16 pixels per element. The LS interpolation overestimates the strain energy for coarser meshes. Even though it cannot be considered a general rule, in this particular problem the overestimation of the strain energy makes the result closer to the convergence value than the other integration schemes.

From the point of view of the computational cost, the LS technique requires fewer integration points for meshes refined below the lower reliability limit (with more than 2×2 pixels per element). In addition, since the number of integration points per element is constant (as in the case of geometry-based cgFEM inner elements), the $\mathbf{B}$ matrix has to be evaluated for one element only and can be scaled for elements belonging to different levels of the Cartesian structure. In Riemann sum and integration subdomain decomposition-based quadratures, in contrast, the $\mathbf{B}$ matrix evaluation has to be carried out for an element of each of the levels involved in the mesh.

On the basis of what was shown in figure 2.22, we consider the LS the most suitable technique for h-refined models (provided that appropriate limits for the element size and maximum heterogeneity allowed are properly chosen) and an effective way to reduce the computational cost in the context of heterogeneity-based h-adaptivity.

2.4.3. A 3D *cg*FEM jaw bone model

As a mere example of efficiency of the meshing process, in Figure 2.23 we show one eighth of an *h*-adapted model obtained from a cone beam CT (CBCT) without previous segmentation. This consists of about 2.8 million nodes and was obtained in 63 seconds with an Intel(R) Core(TM) i7-3770K 3.50 GHz and a RAM of 16 GB of $451 \times 451 \times 451$ voxels.
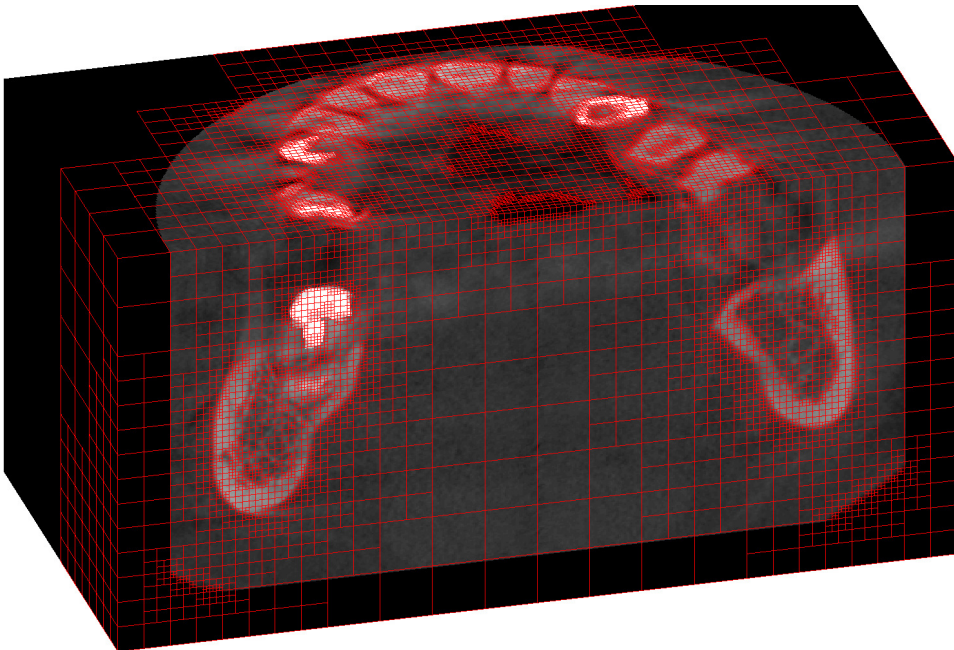

Figure 2.23: One eighth of a *h*-adapted mesh of an unsegmented dental CBCT scan.

In many cases, even in 3D CT scans, Hounsfield scale alone is not sufficient for distinguishing different kinds of biological tissue as very different elastic properties can correspond to the same HU level depending on the location. This makes the model in Figure 2.23 unsuitable for numerical analysis. Furthermore, this particular volumetric image is a Conic Beam CT scan (CBCT), which is preferred for a number

of applications because it reduces the X-ray doses patients receive but is expressed in a specific 16 bits grey scale instead of in Hounfield as CT scans.

In order to obtain a suitable model, we carried out a segmentation of the bony part of the CBCT, see Figure 2.24.

Grey level	0	227	228	1500	2000	4095
E [GPa]	10^{-4}	10^{-4}	0.5	1.5	7	30

Table 2.3: Material Properties referred to Figure 2.19.

In particular this is a $451 \times 451 \times 451$ isometric CBCT with cubic voxels having a side of 0.2 mm. The image was firstly reshaped to make it perfectly fit the hierarchical structure of Cartesian grids. To do so, pixels with a value corresponding to null Young's modulus were added to the scan. After that, a semi-automatic segmentation was used. This is based on thresholding, dilation and erosion and provides a logical matrix used to exclude the elements which only contain irrelevant voxels, see Figure 2.24a.

In the simulation, all the voxels were assigned the same Poisson's ratio value of 0.3 and the Young's modulus was computed by using a C_0 continuous, piecewise linear interpolation of the values in Table 2.3.

The problem of converting CBCT grey scale to the Hounsfield one, see [52], exceeds the purpose of this thesis, consequently, the Young's modulus values in Table 2.3 were extracted from the literature.

To h-adapt the mesh we set a value of $I_R^e = 0.2$. The initial mesh was a uniform grid corresponding to the level 2 of the nested Cartesian grid structure. The maximum level allowed was 8, which corresponds to elements containing $2 \times 2 \times 2$ voxels, see Figure 2.24b.

The element stiffness matrices were integrated by using LS-based technique, see Section 2.2.1. Figure 2.25 shows the problem boundary conditions. On the green surface all the degrees of freedom were constrained and on the red square of 100 mm^2 a pressure of 1 Mpa was applied.

The von Mises stress field is shown in Figure 2.26 for the model cut by the grey plane represented in Figure 2.25. Figure 2.26 shows the expected stress distribution

(a)
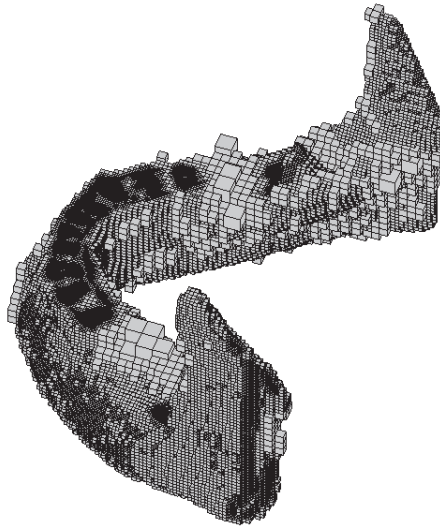
(b)

Figure 2.24: Jaw CBCT scan based model. (a) Segmented jaw; (b) FEAVox *h*-adapted mesh.
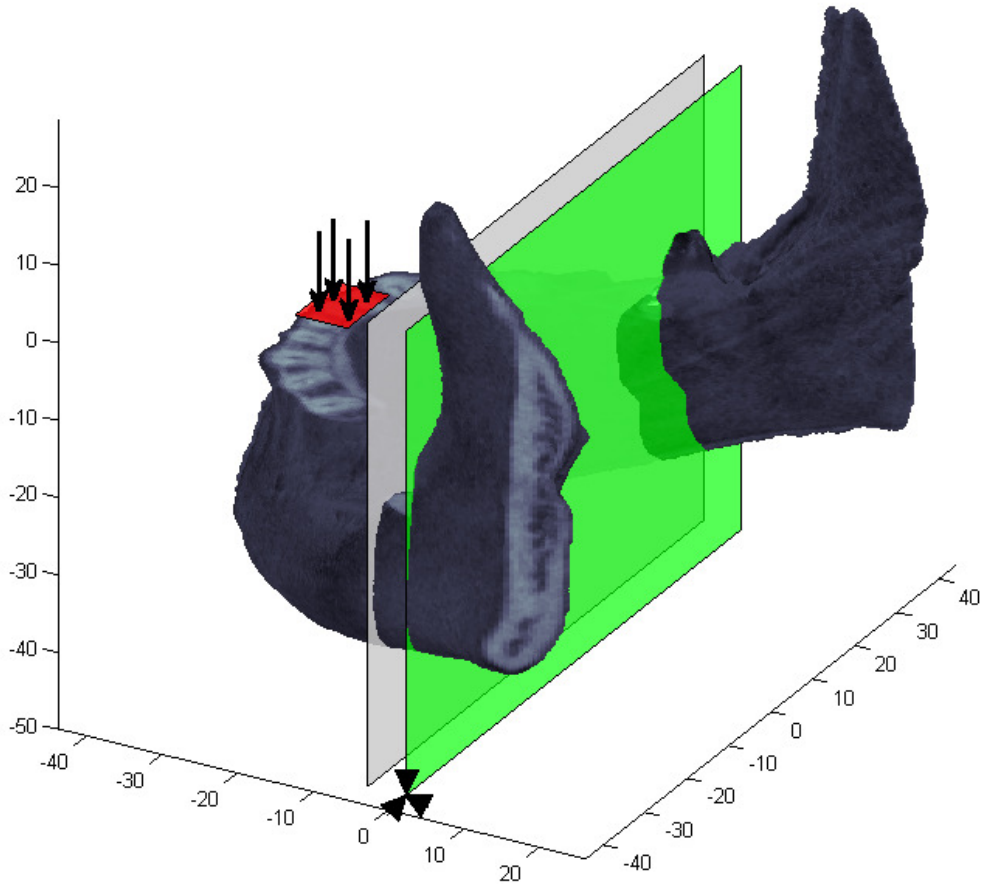
Figure 2.25: Boundary conditions for the problem in Figure 2.24a. Lengths are expressed in mm.

due to bending in the cortical bone and the area locally affected by the pressure application.

The model presented in this case study was obtained from a clinical CBCT scan and is characterised by the complexity and computational cost typical of actual simulation in the biomechanical field. Even though the software is implemented in MATLAB®, which is affected by the typical slowness of interpreted languages, it can handle problems of this size on a regular PC thanks to the characteristics of *cg*FEM.
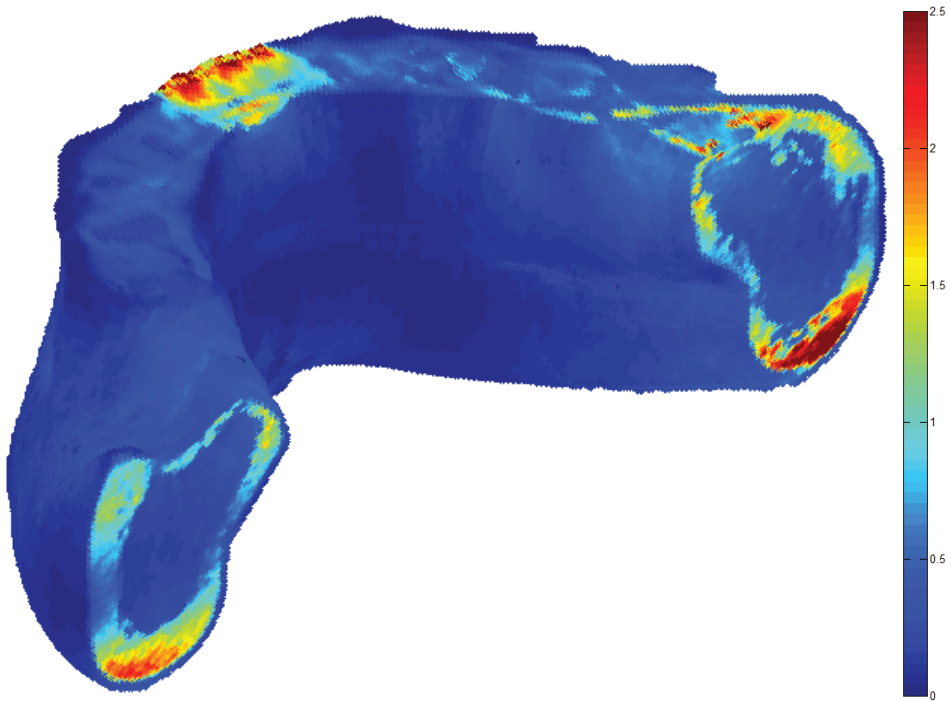
Figure 2.26: von Mises stress field expressed in MPa for the problem in Figure 2.24.

In particular the mesh creation and the integration of the element stiffness matrices took advantage of the speed provided by the hierarchical Cartesian grid structure and the LS integration technique respectively whereas the computational cost of the solution of the system of equations was reduced by the *h*-adaptive strategy and the DOF reordering made possible by the *a priori* knowledge of the mesh structure. This last aspect was exhaustively treated in [32] and [53].

Chapter 3

Material Characterisation

3.1. Introduction

Computational characterisation of materials from CT scan data is currently a relevant area, for a variety of reasons, both in industry as well as in medicine. On the one hand, modern structural components rely, to a great extent, on the behaviour of their constitutive materials. These have an unprecedented influence on the design solutions as the industrial processes to change their macroscopic response by intervening on their micro and mesostructures are both technologically and economically feasible [54], [55].

On the other hand, as bio-signal and image-based computational techniques gain ground in medical applications, the assessment of the macroscopic behaviour of different kind of biological tissues (typically heterogeneous and structured at different length scales, [56] and [57]) by the use of numerical techniques can potentially be a powerful tool in the diagnosis of certain pathological conditions, such as osteoporosis.

In addition to being potentially cheaper (and non invasive in the case of *in vivo* samples) compared to actual mechanical tests, computational characterisation also permits to apply load conditions which are hard or impossible to reproduce on physical samples but, nonetheless, may be fundamental to understand the behaviour of structured materials especially when they distance from isotropy.

Even though machines capable of providing volumetric images with the required resolution are not as common as mechanical testing machines, CT scan-based virtual characterisation of materials is still competitive with experimental testing as it is non destructive, requires a lower number of specimens and a smaller amount of human intervention.

In this chapter, we focus on the characterisation of solid cellular materials. These have a vast range of applications in a number of different industrial fields [58] primary to reduce the weight of mechanical components but also to increase their impact absorption capabilities, enhance acoustic and thermal isolation, create stiff filters, depending on the specific use.

Lately, due to the recent success of 3D printing technologies, the interest in solid cellular materials has grown even in applications for which reducing weight is of secondary importance, such as biomedical engineering.

In trauma, orthopaedics and dental implantology, for instance, porous materials promise to reduce implant failure rates [59] leading, on the one hand, to devices with bio-mimetic mechanical properties less likely to produce stress shielding, [60], [61], and, on the other hand, to surfaces with enhanced osteoinducing properties capable of promoting secondary stability [62], [63].

Due to the presence on the market of equipments capable of providing fine resolution images of human trabecular bone [64], [65], the mechanical characterisation of solid foams from images is also considered a suitable way to assess bone quality and, therefore, the likelihood of osteoporotic fractures, as it is known that loss of connectivity in the cancellous structure has a key role in the phenomenon [66].

As complex structure of solid foams can lead to anisotropic behaviour [67], it is common to use the same homogenisation procedures developed for heterogeneous, potentially anisotropic composite materials [68].

By far, the most common numerical homogenisation technique consists in using FEA to virtually test a sample of material, the so called Representative Volume Element (RVE), [69], [70], [71].

After a short introduction to numerical homogenisation in Section 3.2, we propose the *cg*FEM virtual characterisation technique, which is a powerful automatic tool to obtain homogenised properties of heterogeneous materials from RVEs described by volumetric images. We apply it to solid foams in small deformation regime using a linear elasticity model. The *cg*FEM virtual characterisation technique includes one of the most effective tools for the reduction of the RVE size, the window method [72], which will be treated in Section 3.3. Section 3.4 explains the procedures we followed to obtain experimental results for printed PLA foam samples to be used for the model validation. It also describes how we obtained and preprocessed the μCT scan used in the simulations. *cg*FEM virtual characterisation also includes strategies for the accurate definition of the relation between the local apparent density and the pixel intensity value in solid foams, Section 3.5, as well as a simple method to properly relate apparent density and Young's modulus avoiding the stiffness overestimation introduced by establishing a direct proportionality between them, in Section 3.6. Finally, in Sections 3.7 and 3.8 the effect of the window thickness is studied and the results obtained with the *cg*FEM virtual characterisation are compared with the experimental data and semi-empirical formulae from the literature.

3.2. Numerical characterisation of heterogeneous material in linear elasticity

For the estimation of the RVE constitutive relations in linear elasticity, we assume the displacement and strain fields to be small enough and the load imposition quasi static. Consequently we can neglect both thermal and dynamic effects and consider the stress-strain relationship linear. Similarly, we also assume the material to be free from initial stress or strain,

These hypotheses lead to the familiar formulation

$$\boldsymbol{\sigma} = \mathbf{E} : \boldsymbol{\epsilon} \tag{3.1}$$

The well known linear relation of the second order 3×3 strain and stress tensors and the forth order tensor $\mathbf{E}$ containing the 81 material constants. Due to the symmetry of the Cauchy stress and strain tensors, their order can be reduced and the number of material constants decreased to 36. Therefore (3.1) can be written in Voigt notation as:

$$
\begin{Bmatrix} \sigma_{11} \\ \sigma_{22} \\ \sigma_{33} \\ \sigma_{12} \\ \sigma_{23} \\ \sigma_{31} \end{Bmatrix}
=
\begin{bmatrix}
E_{1111} & E_{1122} & E_{1133} & E_{1112} & E_{1123} & E_{1113} \\
E_{2211} & E_{2222} & E_{2233} & E_{2212} & E_{2223} & E_{2213} \\
E_{3311} & E_{3322} & E_{3333} & E_{3312} & E_{3323} & E_{3313} \\
E_{1211} & E_{1222} & E_{1233} & E_{1212} & E_{1223} & E_{1213} \\
E_{2311} & E_{2322} & E_{2333} & E_{2312} & E_{2323} & E_{2313} \\
E_{1311} & E_{1322} & E_{1333} & E_{1312} & E_{1323} & E_{1313}
\end{bmatrix}
\begin{Bmatrix} \varepsilon_{11} \\ \varepsilon_{22} \\ \varepsilon_{33} \\ 2\varepsilon_{12} \\ 2\varepsilon_{23} \\ 2\varepsilon_{31} \end{Bmatrix}
\tag{3.2}
$$

The material compliance matrix in (3.2) describes the behaviour of a generic anisotropic material under infinitesimal strain conditions and is symmetric due to the first thermodynamics principle. As a consequence the maximum number of independent elastic coefficients necessary for its definition can be additionally reduced to 21 for a fully anisotropic material. Nonetheless, under certain circumstances the number of constants decreases as in the case of monoclinic and orthotropic materials. These are characterised by 13 and 9 constants respectively if a convenient reference system is used. If this is oriented along the symmetry planes, the shear stress components will only depend on the corresponding strain components and will be uncoupled from the other ones. When this condition is independent from the reference system orientation, the material is isotropic and the number of necessary constants is 2.

Numerical homogenisation is commonly based on (3.3), known as the Hill's condition [73], which provides the criteria for the selection of a statistically representative

volume element (RVE) Ω.

$$\langle \boldsymbol{\sigma} : \boldsymbol{\varepsilon} \rangle_{\Omega} = \langle \boldsymbol{\sigma} \rangle_{\Omega} : \langle \boldsymbol{\varepsilon} \rangle_{\Omega} \tag{3.3}$$

Where $\langle \ \rangle_{\Omega}$ is the mean value over the domain Ω.

(3.3) is satisfied by Kinematic uniform boundary conditions (KUBC) on the RVE boundary, see (3.4) and Figure 3.1. .

$$\mathbf{u}|_{\partial\Omega} = \langle \boldsymbol{\varepsilon} \rangle_{\Omega} \cdot \mathbf{x} \tag{3.4}$$

Static uniform boundary conditions (SUBC) on the boundary also satisfy the Hill's condition, (3.5).

$$\mathbf{t}|_{\partial\Omega} = \langle \boldsymbol{\sigma} \rangle_{\Omega} \cdot \mathbf{n} \tag{3.5}$$

In (3.4) and (3.5), $\mathbf{x}$ and $\mathbf{n}$ are the position of the domain boundary $\partial\Omega$ and unit vector normal to it.

The application of one of the load conditions described in (3.4) and (3.5) to a statistically representative RVE provides an approximation of the behaviour of a microscopic sample located in the core of a large sample. The uniform boundary conditions descends from the mandatory requirement that the sample is small enough compared to the structure to which it belongs and large enough to have small boundary field fluctuation [74].

Given a heterogeneous structure and the properties of each of component, Material numerical characterisation permits to obtain the overall material compliance matrix if the RVE is representative.

We assume the strain ε and stress σ fields at each point of the RVE Ω under a given load condition to consists of a fluctuation $\tilde{}$ about an average value $\langle \cdot \rangle_{\Omega}$, see (3.6)

$$\boldsymbol{\varepsilon} = \langle \boldsymbol{\varepsilon} \rangle_{\Omega} + \tilde{\boldsymbol{\varepsilon}}; \quad \boldsymbol{\sigma} = \langle \boldsymbol{\sigma} \rangle_{\Omega} + \tilde{\boldsymbol{\sigma}} \tag{3.6}$$
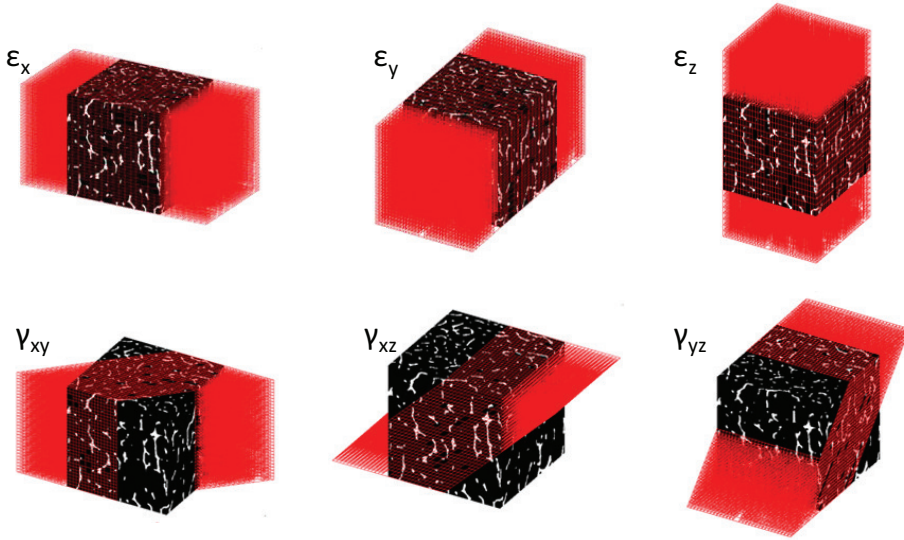
Figure 3.1: Imposition of unit KUBCs on solid foam RVE.

The averaged values represent the behaviour of an equivalent homogeneous material.

Therefore numerical homogenization seeks the compliance matrix $\mathbf{D}$ relating the averaged strain and stress, see (3.7), if the Hill's Condition is satisfied.

$$\langle \boldsymbol{\sigma} \rangle_\Omega = \mathbf{D} \langle \boldsymbol{\varepsilon} \rangle_\Omega \qquad (3.7)$$

3.3. Window method in cgFEM

It is well known that the RVE size has a great influence on the results of heterogeneous material numerical homogenisation. The first reason is that RVE becomes statistically more representative of the material average structure and behaviour as

its size increases. The second one is that the set of boundary conditions, which has to guarantee a given mean strain or stress value in the RVE are generally inconsistent with the actual load transfer between the RVE and the surrounding heterogeneous material and consequently introduces a source of inaccuracy in the area close to the boundary.

This results, for instance, in an overestimation of the RVE stiffness in the case of KUBC (3.4) and in its underestimation with SUBC (3.5) [75]. Increasing the RVE size reduces its surface-volume ratio. For an infinite RVE this effect disappears and all the boundary conditions satisfying the Hills condition converge to the same result.
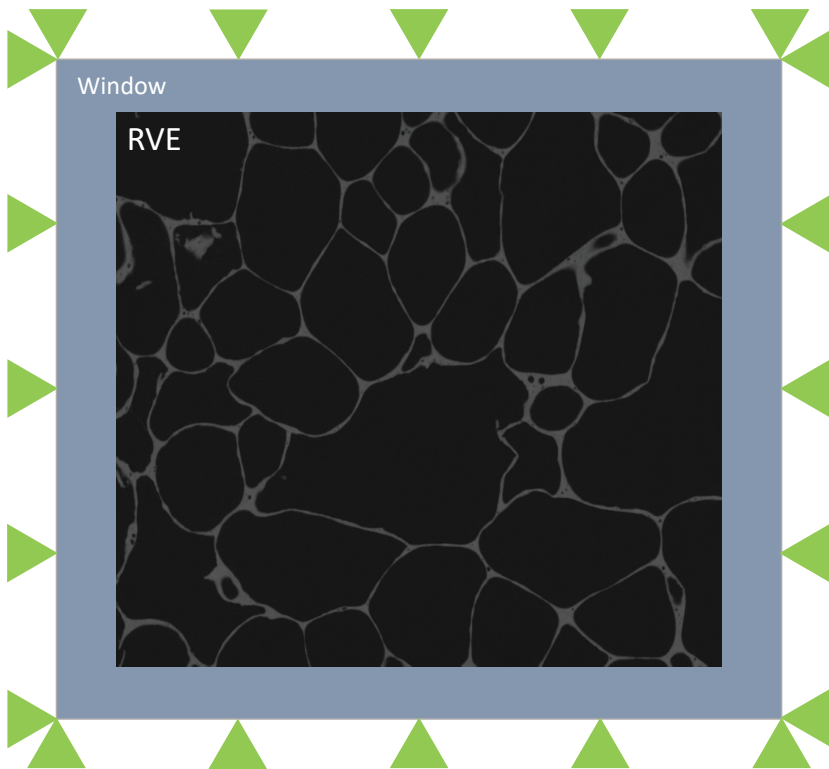
Figure 3.2: Schematic representation of KUBC imposition on an RVE with the window method.

In order to keep the RVE size small and, consequently, the computational cost of the

simulation low, we use the window method proposed in [72] for the homogenisation of CT scans of concrete samples with a uniform voxel-based FE mesh and applied in [68] for the numerical characterisation of solid foams with the FCM. The optimality of the method was theoretically and numerically proved in [76].

The objective of every homogenisation method is the determination of the constitutive coefficients of a homogeneous material equivalent to the heterogeneous RVE. The window method consists in embedding the RVE into a larger volume of this equivalent material and applying the proper boundary conditions on the window external contour instead of the RVE boundary. As the coefficients of this homogeneous equivalent material are unknown, an iterative process is used for their evaluation.

In particular we apply KUBCs on the window external boundaries and compute the average stress in the RVE, see Figure 3.2. The procedure starts with the application of the rule of the mixture on the RVE to define the material property tensor which is assigned to the window elements as an initial guess. Then, the cgFEM model is created, distinguishing the elements on the RVE and those on the window. We solve the problem for the 6 KUBCs shown in 3.1, and compute the material elastic property tensor from the average values of the stress tensor in the RVE and the average strain conditions applied. This is then assigned to the element on the window for the following iteration until the Frobenius norm of the increment of two consecutive window compliance matrices decreases under a given threshold. This is 1% for the numerical examples in Sections 3.7 and 3.8.

It is worth mentioning that the further iterations are less expensive then the first one because neither the model has to be re-meshed nor the stiffness matrices for the elements on the RVE have to be computed again. Apart from the solution of the system of equations, each iteration only requires updating the stiffness matrices of the elements on the window, but this is inexpensive because they are proportional to each other by a scale factor known *a priori* and share the same material property matrix, therefore only one element is integrated, similarly to the inner elements in standard geometrical cgFEM, see Section 2.1.

3.4. 3D printed foam experimental testing

This section explains how we obtained the specimens for the experimental validation of the homogenisation method as well as the CT scan representing their structure.
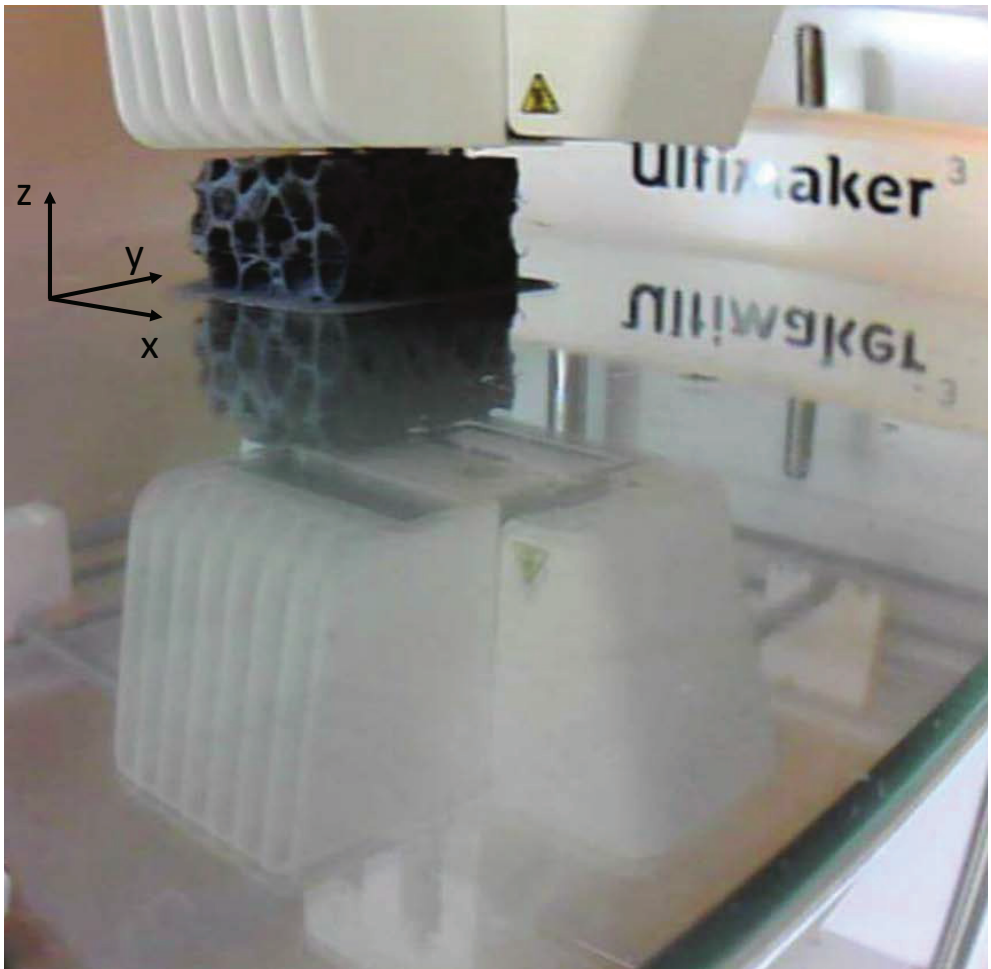

Figure 3.3: 3D printing process and coordinate system.

We started by segmenting the μCT scan of and ALPORAS aluminum foam specimen using the software 3DSlicer [77]. The segmentation mask was than treated to increase the cell wall thickness with Matlab® [78] and converted to a STL file.
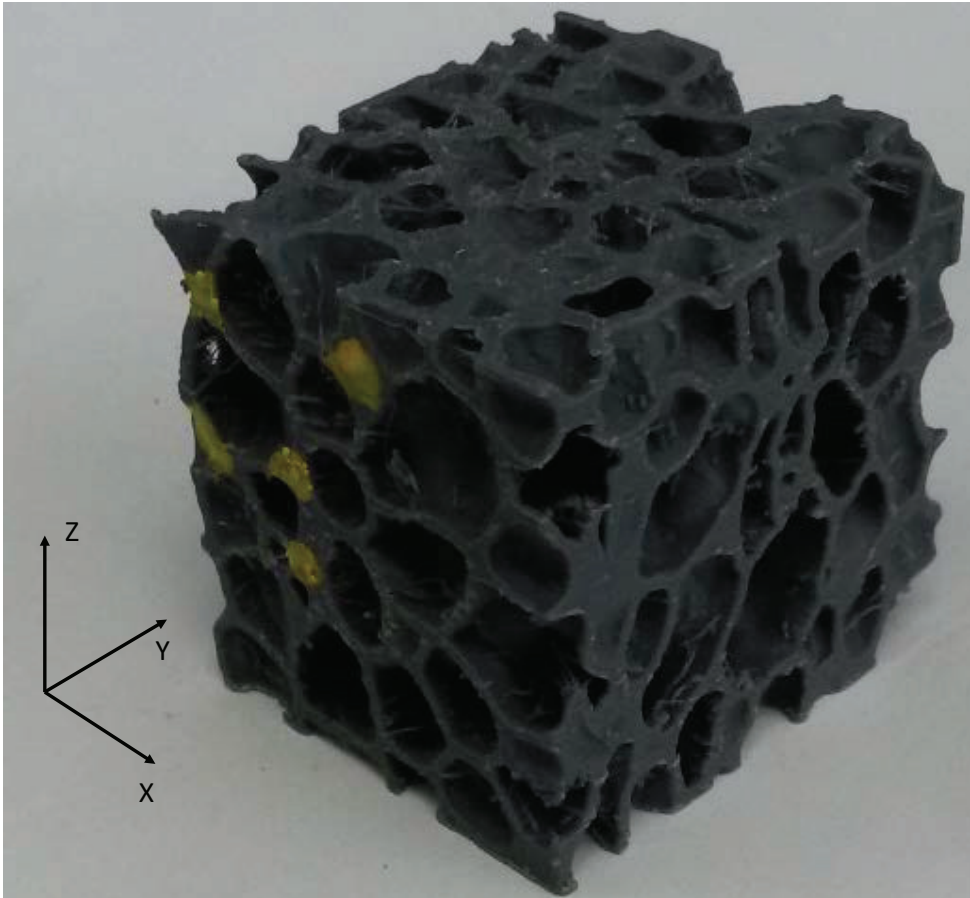

Figure 3.4: PLA 3D printed foam sample corresponding to Spec 5 (5 yellow marks) and coordinate system.

From this, Several PLA foam specimens, Figure 3.4, were printed form this geometrical model with the 3D Printer Ultimaker 3, see Figure 3.3. Then, we had one of the PLA specimens scanned with the MicroCT 80 by Scanco Medical [79] at a resolution of 29 μm.

The PLA foam CT scan was sub-sampled at $2 \times 2 \times 2$, $4 \times 4 \times 4$ and $8 \times 8 \times 8$ in order to reduce the computational cost of the simulation. The $4 \times 4 \times 4$ was used in the homogenisation process.

On the one hand, the process made it possible to have a reasonable number of similar specimens to test. The wall thickness increase was necessary to reduce the effect of the 3D printing machine precision on the specimen structure.

In comparison with the original Aluminium ALPORAS foam, the new specimens have thicker walls and smaller the pores. Therefore, these are better defined in the μCT for the same resolution in comparison to the original ALPORAS foam. The volumetric image was used for the numerical characterisation with cgFEM, whereas six specimens underwent displacement controlled uniaxial compression during two sessions with different testing machines.

In the following, we will describe the two test series, show the strain-stress curves corresponding to each test and identify the linear elasticity parts of the curves as the one providing a coefficient of determination R^2 of 0.999 for a linear fitting.

3.4.1. First group of tests: compression in z-direction

For the first test section, we used an electromechanical machine Ibertest ELIB 50, see Figure 3.5.

We tested two samples of 27.30 and 27.26 g respectively (Spec 1 and Spec 2 in Figures 3.6 and 3.7). The strain-stress curves for Spec 1 at loading condition and Spec 2 for both loading and unloading are shown in Figure 3.6.

The compression curves in Figure 3.6 show a non-linear behaviour in the first part typical of small mismatches between the machine plates and specimen contact surfaces, which are not perfectly parallel to each other. When, as the compression goes on, the surfaces start matching and the stress-strain relationship becomes linear in the small strain range in which the test was carried out.

Figure 3.7 shows the part of the curves used for the calculation of the Young's modulus in the linear elastic range.

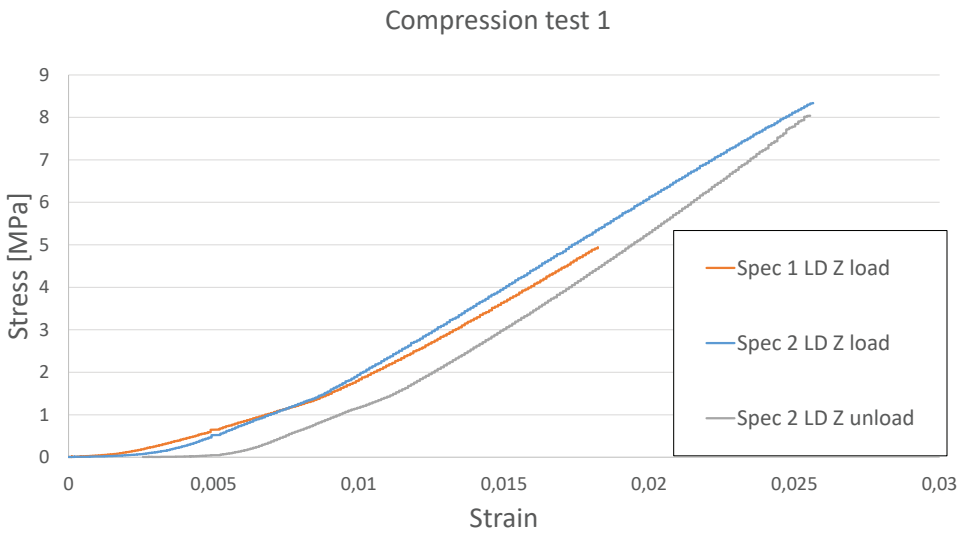Figure 3.5: Set up of the first PLA foam compression test series.

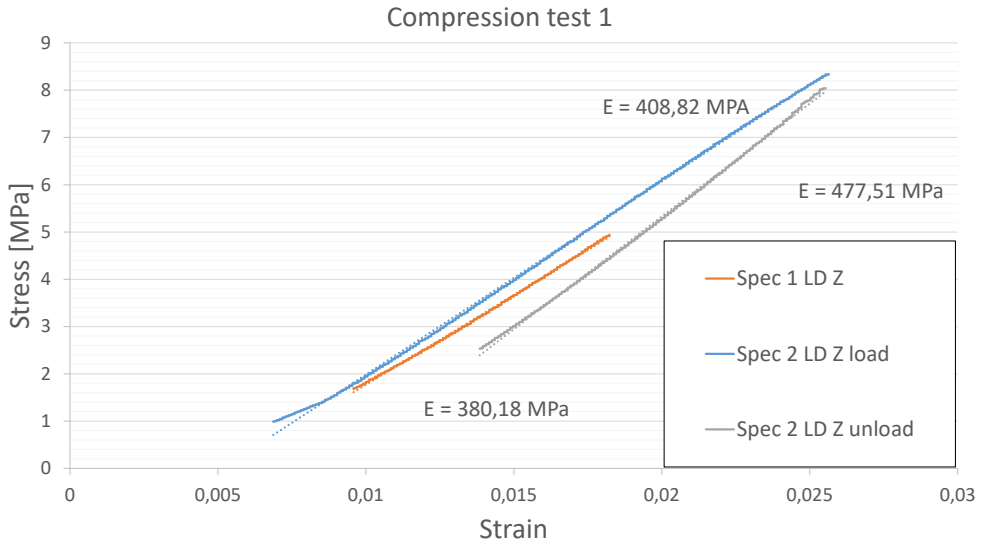Figure 3.6: Stress-strain curves from test 1.

Figure 3.7: Young's modulus calculation in test 1.

3.4.2. Second group of tests: compression in x, y and z directions

Five additional tests were carried out with a Mashimadsu Autograph AG-X Plus 100 kN machine, Figure 3.8.

The specimens weighed 27.3, 27.36, 27.33, 27.18 and 27.54 g respectively. For each specimen loading and unloading were taken into account, see Figure 3.9. We refer to each specimen with a number from 1 to 5 and the load direction (LD) according to the reference system shown in Figure 3.4.

For the first compression test we reused the first specimen of the first test series (called Spec 1 LD Z in both tests) as a pilot to choose the test range fo the other specimens, therefore, in that case, we reached the non linear part of the strain-stress relation, see the light blue curve in Figure 3.9.

The linear sections for loading and unloading are shown separately in Figures 3.10 and 3.11 with the corresponding Young's modulus values.
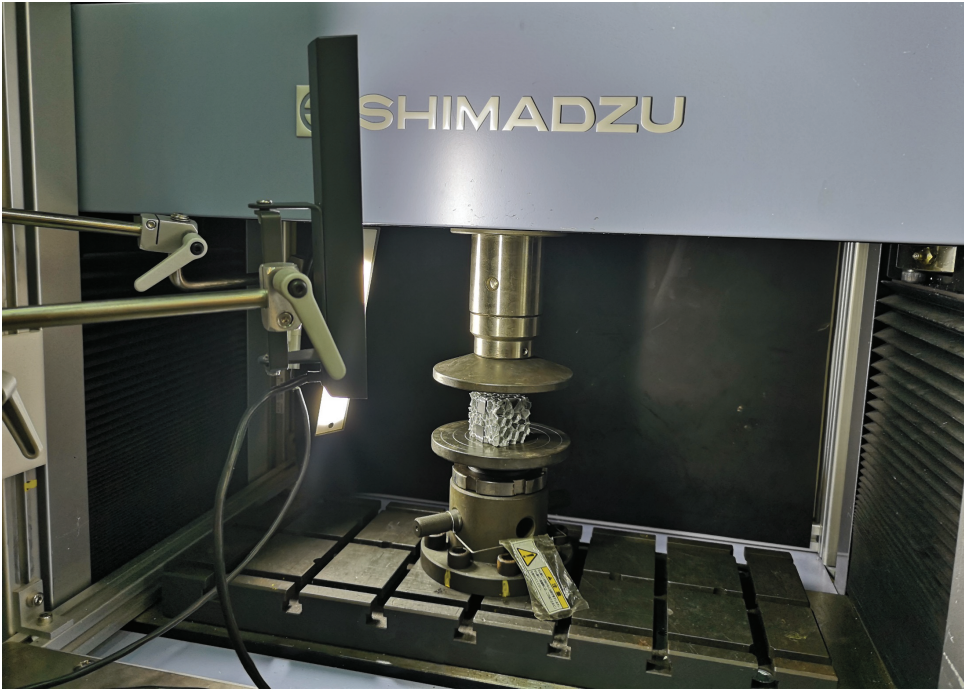
Figure 3.8: Set up of the second PLA foam compression test series.

Load Direction	X	Y	Z
Mean	346.86	414.46	453.01
Standard Deviation	-	162.69	70.05

(a) Young's modulus in MPa during load

Load Direction	X	Y	Z
Mean	504.50	495.49	536.98
Standard Deviation	-	161.42	53.77

(b) Young's modulus in MPa during unload

Table 3.1: Mean values and standard deviation for the test results in loading (a) and unloading (b) conditions.
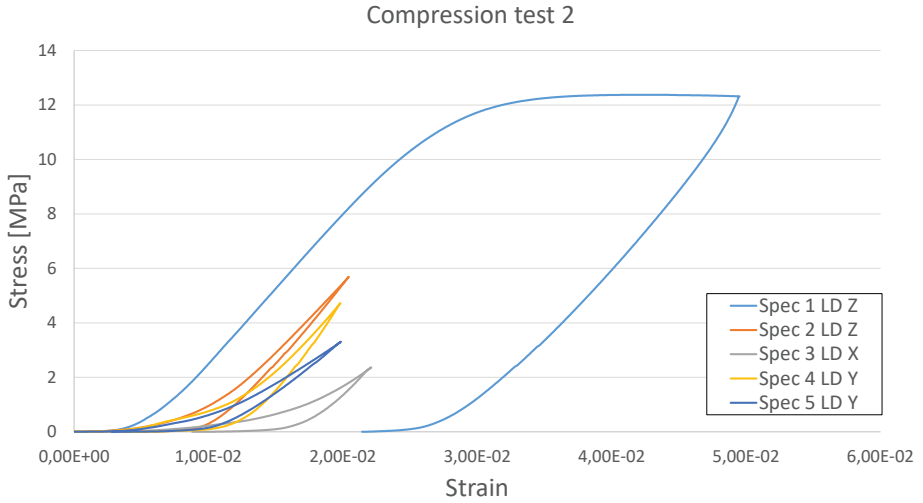
Figure 3.9: Stress-strain curves from test 2.
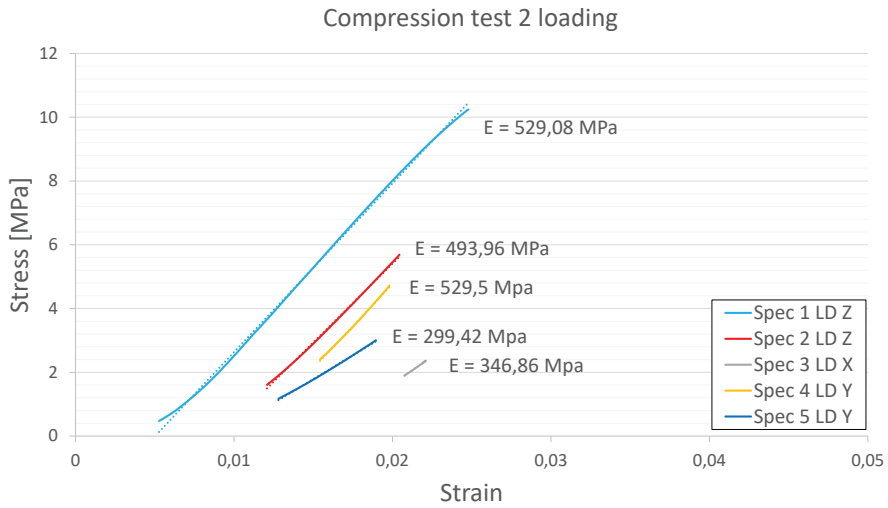
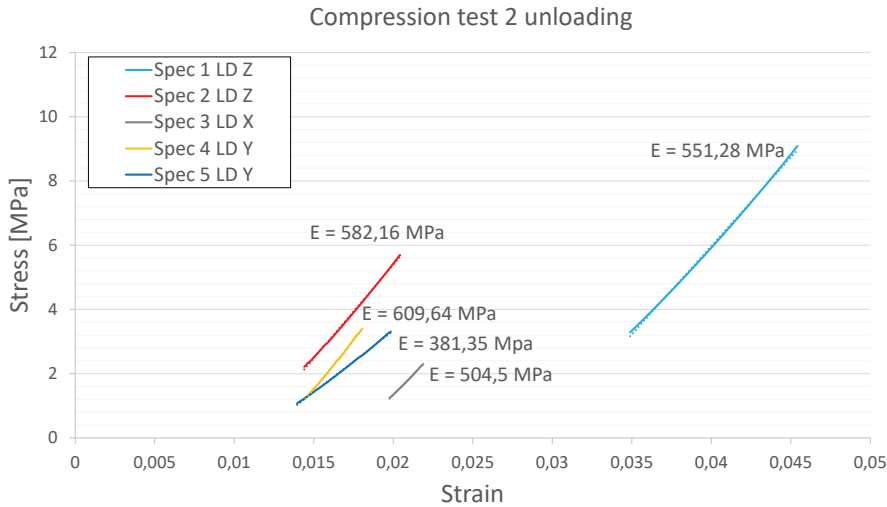Figure 3.10: Young's modulus calculation from test 2 loading.

Figure 3.11: Young's modulus calculation from test 2 unloading.

Tables 3.1 show the mean and standard deviation for the directional Young's modulus values obtained by the groups of tests in loading (a) and unloading (b) conditions.

In the following, we will take as a reference the Young's modulus values obtained in unloading conditions under the assumption that during the loading the behaviour of solid foams is biased by local effects, see [80].

3.5. Relation between density and pixel colour

In this section, we present a method for the determination of the relationship between the values of the pixels in the foam CT-scan and the corresponding relative density values.

For the sake of clarity, it is worth reminding that we had a 3D printed PLA foam sample scanned at a resolution of 29 μm, see Section 3.4. This was similar to the samples used in the experimental tests presented in the previous section. We obtained a $4 \times 4 \times 4$ sub-sample from the original μCT scan. All the computational results presented in this chapter refer to this lower resolution (116 μm) volumetric image.

We assume density is null below a lower pixel colour threshold and one over an upper one and consider the relative density to have a linear dependency with pixel colour between these two values, see Figure 3.12. This volume averaging for pixels on interfaces implies the hypothesis that, due to discrete spatial resolution of the CT scan, the radiodensity is linearly proportional to the amount of PLA in the volume corresponding to the respective pixel. This phenomenon is also known as tissue fraction effect and is only one of the two causes of the partial volume effect (PVE), the error affecting the accuracy of medical volumetric images at the interface between different materials [81]. The other phenomenon, included in PVE, is the convolution blurring due to the detector finite size and the image reconstruction process. This is the main responsible for the inaccuracy of the volume averaging assumption in general and increases with the radiodensity difference between the materials in the same pixels [82]. In our particular case, however, we consider that the sub-sampling we perform on the original μCT scan to reduce the computational effort required, mainly magnifies the inaccuracy due to the tissue fraction effect and, therefore, makes it possible for us to overlook the contribution of the convolution blur to the PVE. Consequently, we expect to introduce negligible sources of inaccuracy by considering the relation between pixel radiodensity and density linear.

This is represented as the slope in Figure 3.12, defined by two unknown parameters: the midpoint V_0 and the half-width Δ.

It is possible to determine the geometric locus which satisfies the specimen density in the V_0-Δ plane, by iteratively fixing V_0 and looking for the Δ value which corresponds to the specimen density.

Figure 3.13 shows an example of isodensity curves for sub-sampled volumetric images $2 \times 2 \times 2$, $4 \times 4 \times 4$ and $8 \times 8 \times 8$ times smaller than the original one. In the case of high resolution μCT scans sub-sampling is often necessary to reduce the computational cost of FE analyses. We use some considerations on the foam histogram, to complete the definition of the relation between pixel values and density.
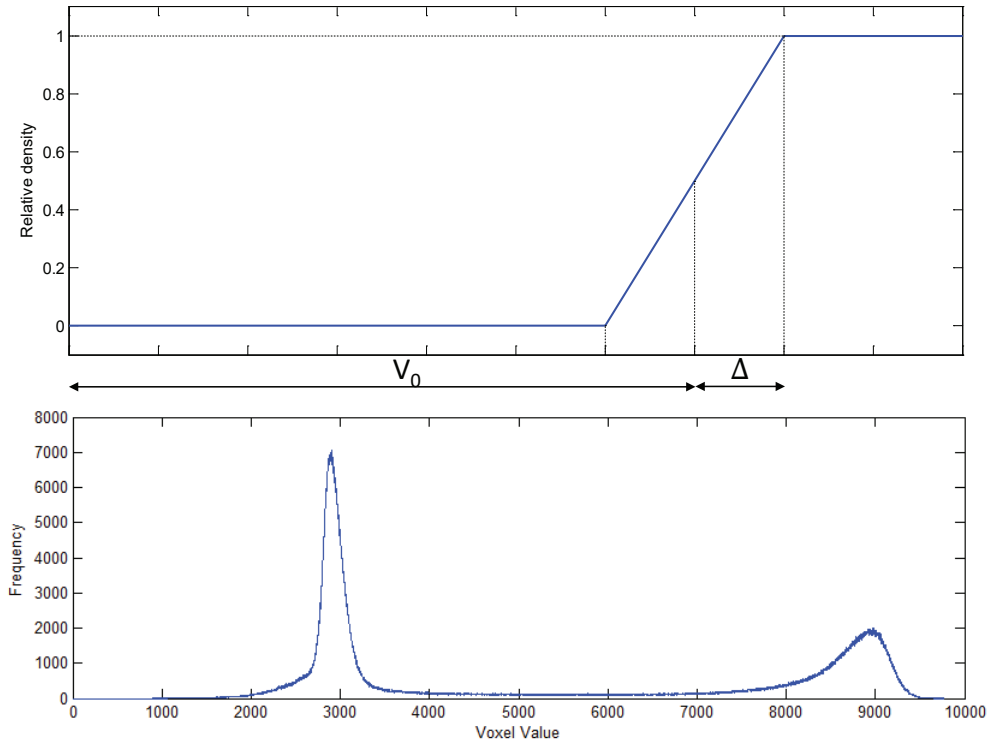
Figure 3.12: CT scan histogram and relative density.

The blue curve in Figure 3.14 represents the μCT scan histogram after the 4 × 4 × 4 sub-sampling. The left and right peaks are associated to Hounsfield values corresponding to air and PLA respectively. Since the pixels affected by the PVE have lower HU values compared to those in the bulk, we assume that these are the main responsible for the lack of symmetry of the frequency distribution about the PLA peak. This would be a symmetric Gaussian-type distribution about a mean value in the case the μCT scan represented solid PLA only. Similar hypotheses are common in thersholding of 2D images [83], CT scans [84], [85] and MRIs [86]. We obtain an estimation of this theoretical PLA pixel distribution by symmetry from the right half of the peak, see red dotted line in Figure 3.14 and a magnified representation in Figure 3.15.
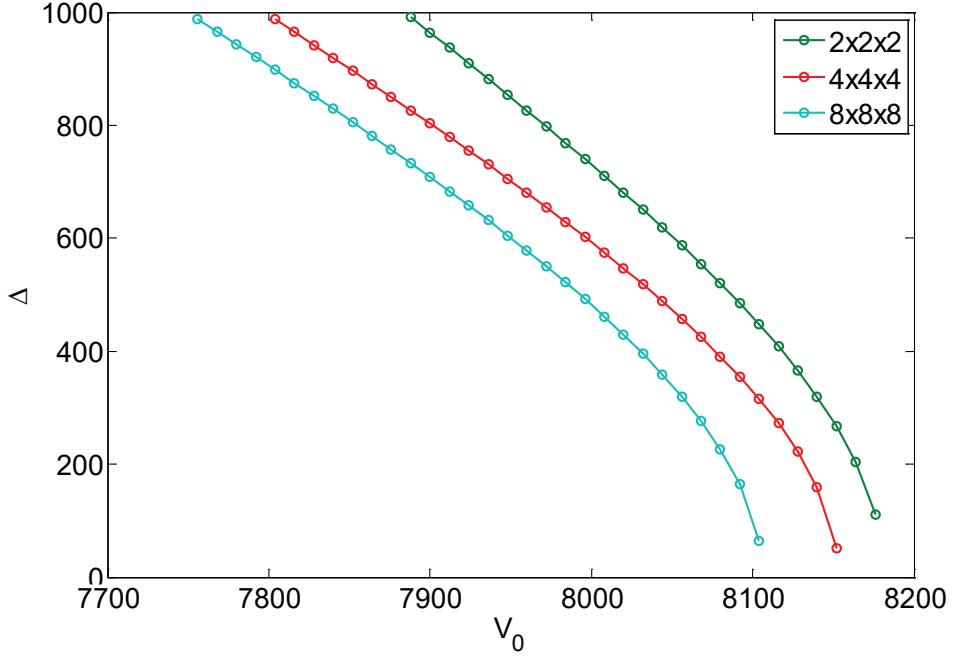
Figure 3.13: Geometrical loci satisfying the experimental specimen density for sub-sampled volumetric images.

It is impossible to completely distinguish the voxels affected by the PVE from those with a reduced HU value because of the normal distribution from the pixel value only. In spite of that, under the previous hypotheses, we can estimate the amount of voxels whose density would be underestimated, depending on the location of the right limit of the density slope $V_0 + \Delta$. By integrating the red dotted curve, the expected theoretical solid PLA distribution, we can estimate the percentage of pixels in the bulk taken into account correctly. Following this strategy, we distinguish two sources of error. On the one hand, we underestimate the stiffness contribution of solid PLA pixels classified as affected by PVE (part of the red curve to the left of $V_0 + \Delta$ in Figure 3.14). On the other hand, we overestimate the stiffness contribution due to the voxels affected by PVE classified as solid (difference between the blue and red lines to the right of $V_0 + \Delta$ in Figure 3.14.
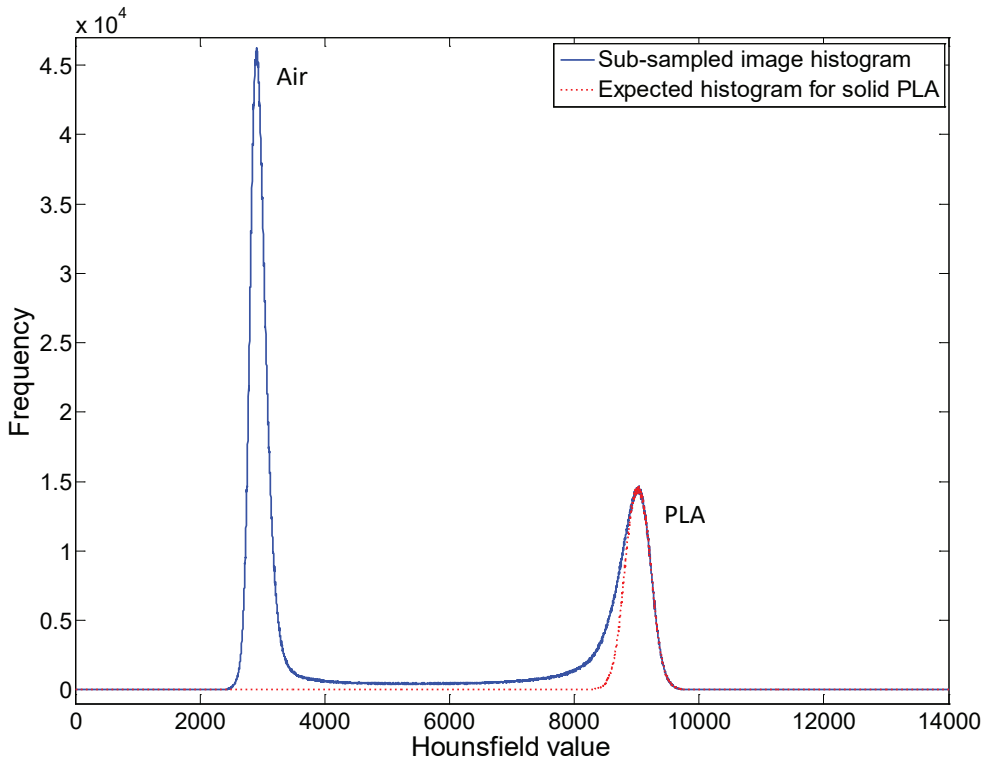
Figure 3.14: Histogram of the 4×4×4 sub-sampled CT scan and estimated theoretical pixel value distribution for a solid PLA sample.

Figure 3.16 shows the histogram analysis of the $4 \times 4 \times 4$ sub-sample of the PLA foam specimen scanned but not mechanically tested obtained as described in Section 3.4. The isodensity V_0-Δ curve in Figure 3.16a refers to the measured density value of the physical specimen. As shown in Figure 3.16b, for each point of this curve, only one couple of values is possible for the lower ($V_0 - \Delta$) and upper ($V_0 + \Delta$) limits of the density slope in Figure 3.12. Consequently, for each point of the isodensity curve, it is possible to compute the percentage of the solid PLA voxels properly classified
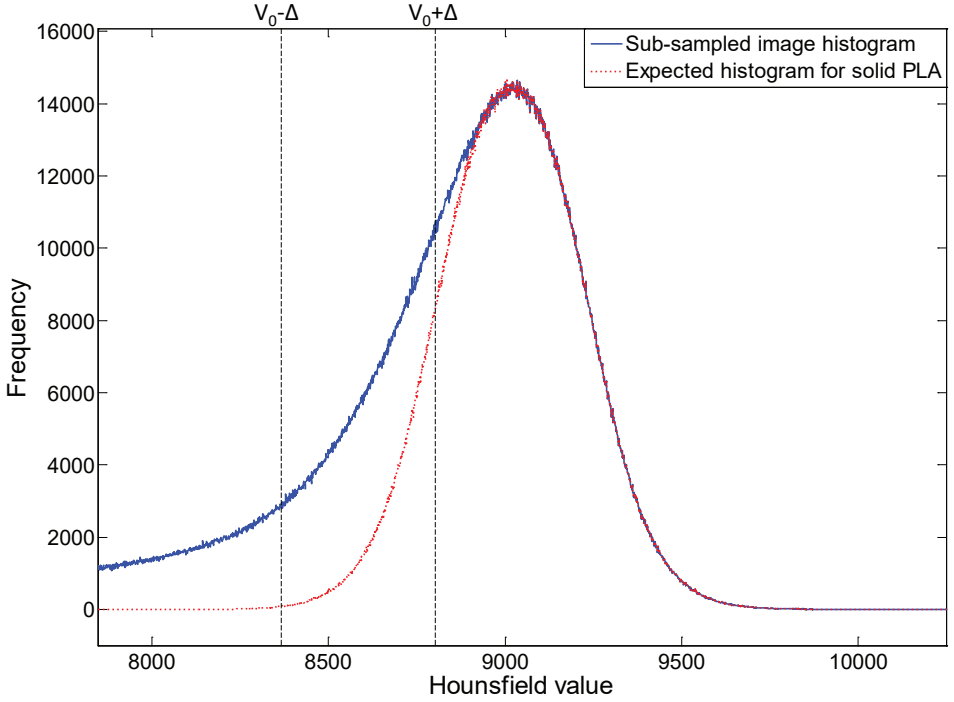
Figure 3.15: Magnification of PLA frequency peak in the histogram of the sub-sampled 4×4×4 CT scan in Figure 3.14.

by computing the ratio between the integrals of the red curve in Figure 3.15 in the intervals $[V_0 + \Delta, \infty)$ and $(-\infty, \infty)$.

The values of this estimated confidence on the proper treatment of the voxels in the bulk is shown in Figure 3.16c. It is worth reminding that when the confidence level increases, the number of pixels affected by the PVE classified as solid is expected to increase too. The values of V_0 and Δ for a confidence level of 68%, 95% and 99.7% are highlighted.

Figure 3.18 shows the relative density map corresponding to the three aforementioned confidence levels. The distributions in Figure 3.18a seems to capture the inner defects of the printed material better than Figures and 3.18b and 3.18c.
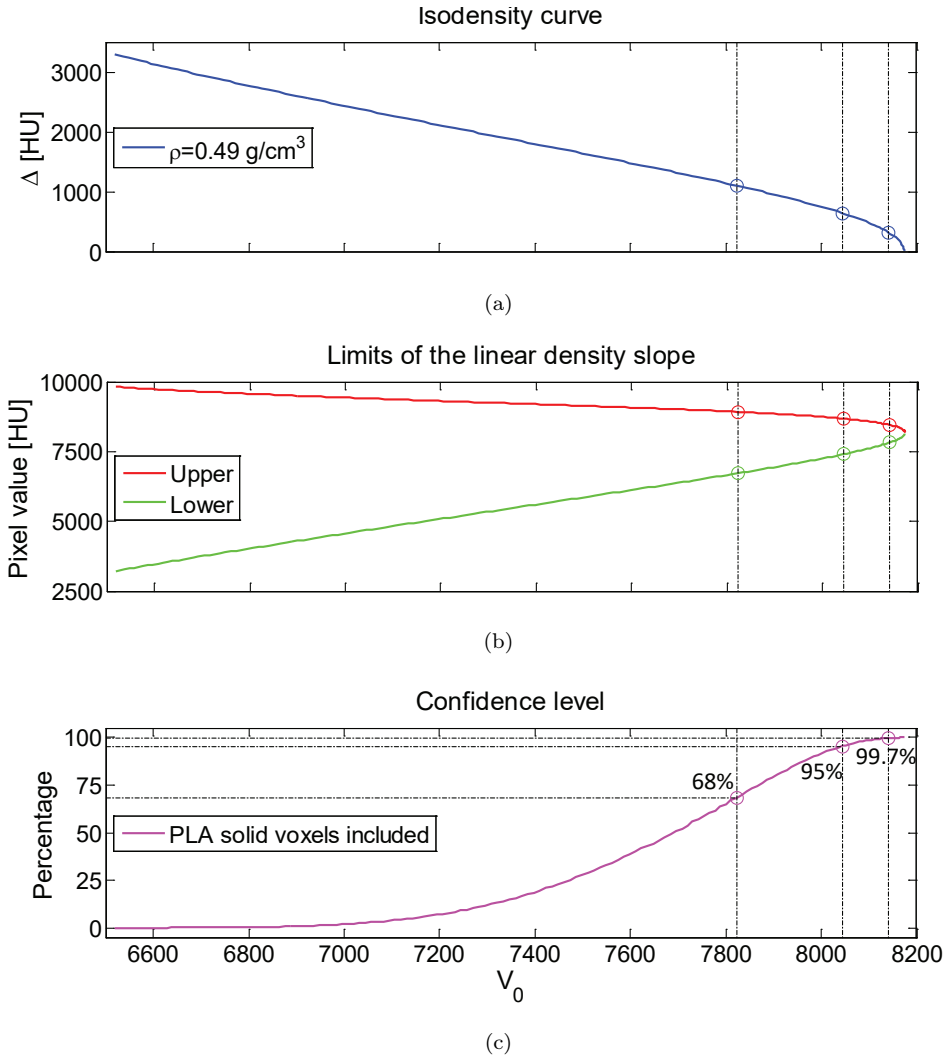
Figure 3.16: Results of the histogram analysis for the $4 \times 4 \times 4$ sub-sample of the PLA foam µCT. (a) V_0-Δ isodensity curve for the measured density of the physical specimen; (b) Upper $(V_0 + \Delta)$ and lower $(V_0 - \Delta)$ limits for linear slope of the ρ-HU relation; (c) Estimated percentage of solid PLA voxels properly classified.
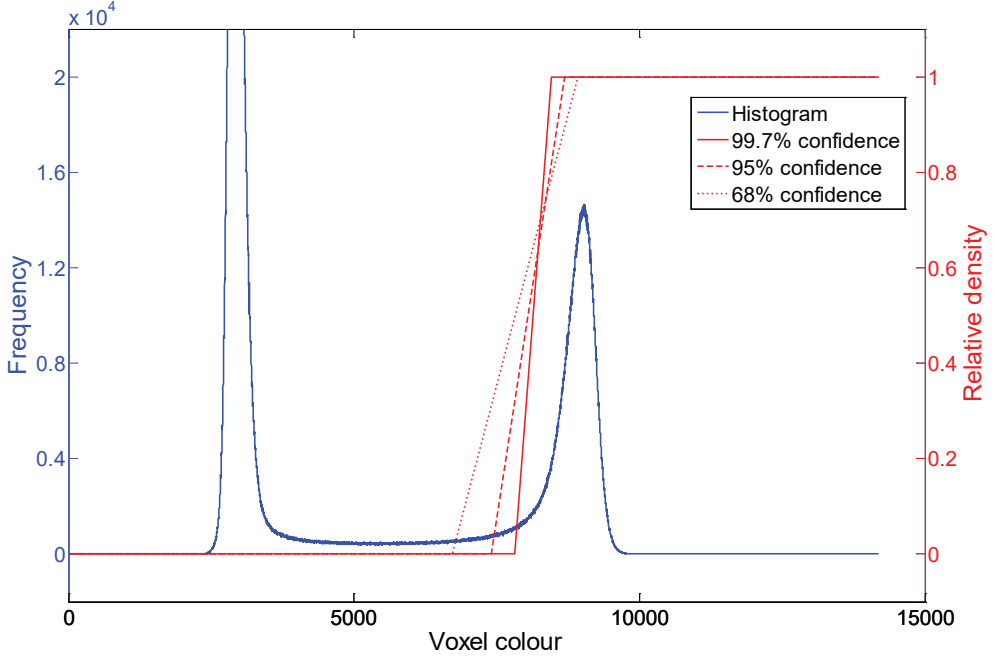
Figure 3.17: Rho-HU relation for different confidence levels.

In this case, we worked with the 27.30 g specimen, which has a density of 0.49 g/cm^3. Due to the great μCT size, which makes it extremely expensive to process it directly with *cg*FEM, we obtained a coarser volumetric image more suitable for computing by sub-sampling to an image $4 \times 4 \times 4$ times smaller. So far we have set a relationship between density and pixel colour which satisfies the experimental apparent density value of the specimen, see Figure 3.13, and depends on the parameters V_0 and Δ, see Figure 3.12. These also provides a similar relationship between Young's modulus and pixel colour under the hypothesis that this is linearly proportional to the density value in the range in which the image is affected by the PVE.
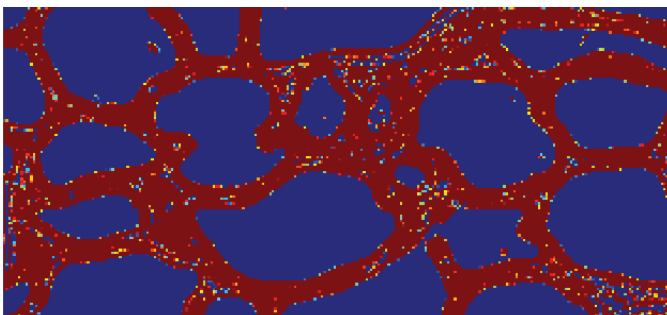
The specimen weight and volume make it possible for us to find the couples V_0-Δ, which guarantee the same density of the printed foam, assuming solid PLA density is 1.25 g/cm^3, see Figure 3.16.
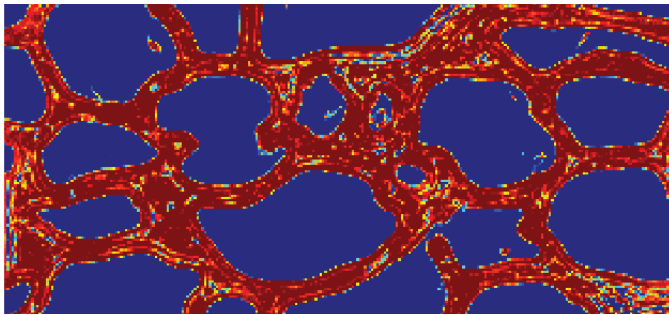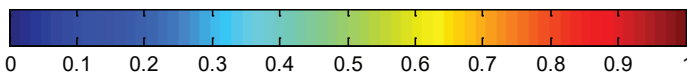
(a)
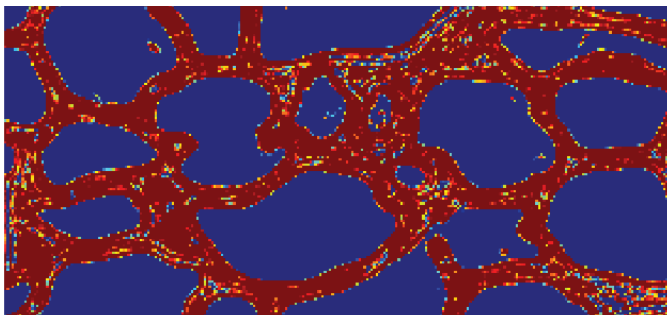
(b)

(c)

Figure 3.18: Part of the central slice in the x-y plane of the CT scan of the PLA foam specimen. Density map representation depending on the confidence level: (a) 68%; (b) 95%; (c) 99.7%.

3.6. Partial volume correction function

Assuming a PLA Young's modulus of 3.2 GPa, previously measured by tension test on homogeneous PLA specimens manufactured with the same 3D printer as the foams, and a Poisson's ratio of 0.36, taken from the literature [87], all the attempts to reproduce the experimental results moving on the iso-density curves resulted in severe stiffness overestimations. Our hypothesis is that the simple direct proportionality between density and Young's modulus is not suitable for images heavily affected by the PVE such as foams.

In this section we propose a Young's Modulus correction coefficient $\bar{\alpha}$ which makes it possible for us to take into account statistically the effect of the arbitrary orientation of the surface within the voxel, see Figure 3.24.

In this implementation of cgFEM, the material is considered isotropic at the level of the pixels, that is the $\mathbf{D}$ matrix computed at the pixel level is defined by the Young's modulus and Poisson's ratio only, in contrast to the elastic compliance tensor computed by the homogenisation analysis for the whole RVE which, in the general case, can be completely anisotropic. Consequently a simple tension on the pixel extracted from the rest of the image is independent from the load direction. In contrast, if we substitute the pixel with the underlying geometrical model the corresponding Young's modulus is highly directional. For the sake of clarity, we introduce the 2D example shown in Figure 3.19. We consider the tension test in the x direction on an intermediate grey level pixel, see Figure 3.19a, and assume the grey level value only depends on the PVE, that is all the underlying geometries with the same quantity of material provide the same colour of the pixel. For simplicity, we consider that the boundary of the material within the pixel is a straight line. This is called l and is defined by the angle β of its unit normal vector $\mathbf{n}$ with the x direction and by the intersection with the square diagonal d at the point P, see Figure 3.19b. The Young's modulus measured during the test would be null for $\beta=0°$, Figure 3.19c whereas it would perfectly follow the mix rule for $\beta=90°$ Figure 3.19e.

These can be considered as special cases of Ruess and Voigt bounds. Intermediate stiffness values can be found at different values of β for the same volume ratio, see Figures 3.19c to 3.19e.
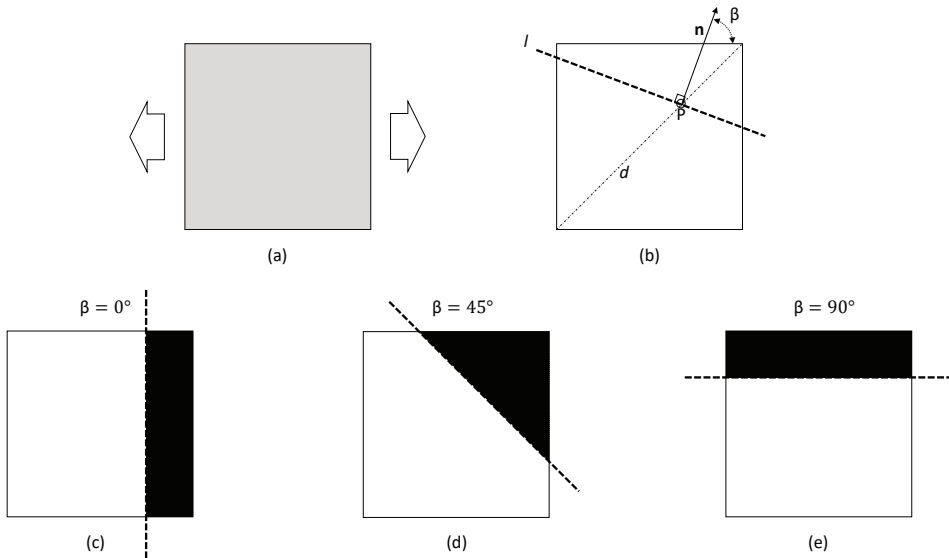
Figure 3.19: Scheme of pixel affected by partial volume effect. A pixel of a given grey level (a), can be the product of different intersection patterns with the plane l, (b), which share the same area but behave differently in the same load conditions, such as (c), (d) and (e).

To take into account this effect in pixels with density values below that of the core material, we introduce the partial volume correction function $\bar{\alpha}(\rho)$ having values between 0 and 1. This scales the Young's modulus to its average value along all the possible load directions for a given pixel density.

It is possible to compute $\bar{\alpha}$ by extending to the third dimension the example in Figure 3.19. For this purpose, we have cut out a polyhedron from a unit cube with an arbitrary plane, see Figure 3.20, and compute the vertical stiffness and volume of the polyhedron for a high number of positions and orientations of the intersecting plane. Finally we resample the relative density of the polyhedra (the ratio between their volume and the volume of whole cube) and for each density value, we averaged the vertical stiffness over all the possible plane orientations to obtain an estimation of $\bar{\alpha}(\rho)$.

In the following, we use some simplifications to approximate $\bar{\alpha}(\rho)$ numerically. As in the 2D case of Figure 3.19, we vary the intersecting plane by changing the direction of its normal and its intersection point with one of the cube space diagonals.
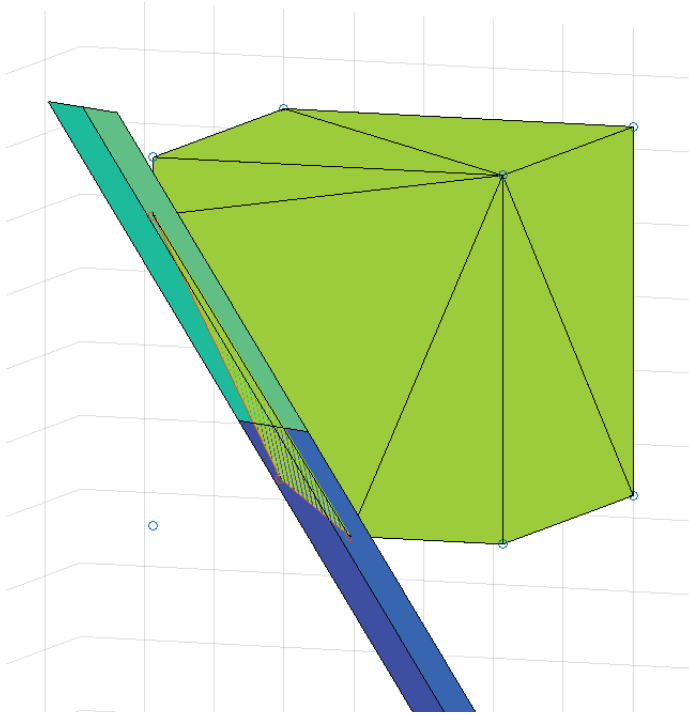
Figure 3.20: Polyhedron cut out by surface.

In contrast to the 2D example, in 3D we need 2 angles to define the plane direction. These are the polar angle ϕ and azimuth angle θ, see Figure 3.21.

We vary these angles between $0°$ and $85°$ with steps of $5°$ whereas consider equidistant intersection points on the cube space diagonal for the definition of the intersecting plane. For each intersection we compute the polyhedron volume in relation to the whole cube.

For each polyhedron cut out from the cube we approximate the overall vertical stiffness by using the well known simplified model for non-uniform bars under axial tension, see Figure 3.22.

Under the assumption that all the components of the stress tensor are negligible except the normal stress component in z direction σ, the Hooke's law is satisfied at the bar cross section for any value of z by
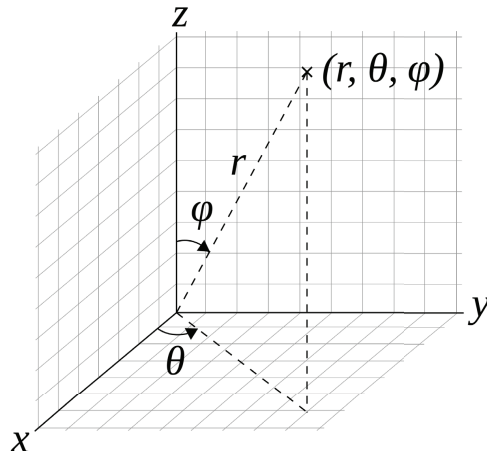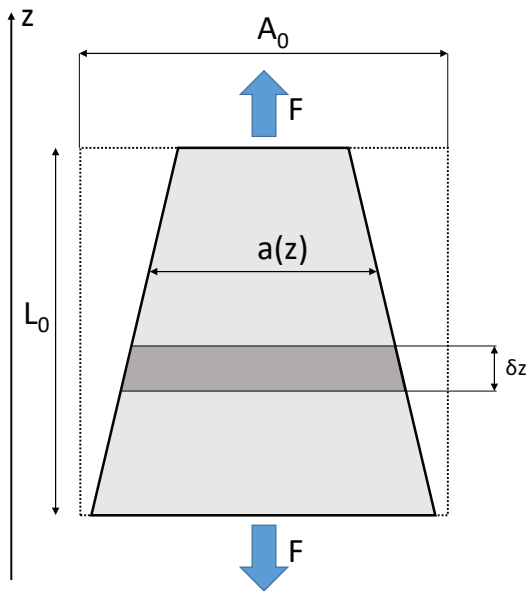
Figure 3.21: Spherical coordinate system.

Figure 3.22: Schematic representation of simplified model for non-uniform bars under tension.

$$\sigma(z) = E\varepsilon(z) \tag{3.8}$$

where ε is the normal strain in direction z and E the material Young's modulus. The corresponding element of infinitesimal thickness δz undergoes the length change δl:

$$\delta l = F\frac{\delta z}{Ea(z)} \tag{3.9}$$

where F is the external axial force and $a(z)$ the cross section area value at z. We obtain the overall length change of the bar by integrating (3.9) over the initial length L_0 and divide by L_0 to compute the average strain value in the z direction $\langle\varepsilon\rangle$:

$$\langle\varepsilon\rangle = \frac{F}{EL_0} \int_0^{L_0} \frac{dz}{a(z)} \tag{3.10}$$

If we consider the apparent tension value $\langle\sigma\rangle = F/A_0$ applied to the upper pixel surface, the average stress-strain relationship is

$$\langle\sigma\rangle = \frac{L_0 E}{A_0 \int_0^{L_0} \frac{dz}{a(z)}} \langle\varepsilon\rangle \tag{3.11}$$

(3.11) makes it possible for us to estimate the directionality coefficient α, which accounts for the reduction of the cube stiffness by scaling Young's modulus.

$$\langle\sigma\rangle = \alpha E\langle\varepsilon\rangle \tag{3.12}$$

The coefficient α depends on the cross section variation along z and, therefore, only on the intersection between the plane and the cube, which can be univocally defined by the pixel density, polar and azimuth angles.

$$\alpha(\rho, \phi, \vartheta) = \frac{L_0}{A_0 \int_0^{L_0} \frac{dz}{a(z)}} \tag{3.13}$$

The integral at the denominator of (3.13) is computed numerically by a first degree

Newton-Cotes quadrature. This uses 101 samples of the area values $a(z)$ of the intersections between the polyhedron and equidistant horizontal planes.

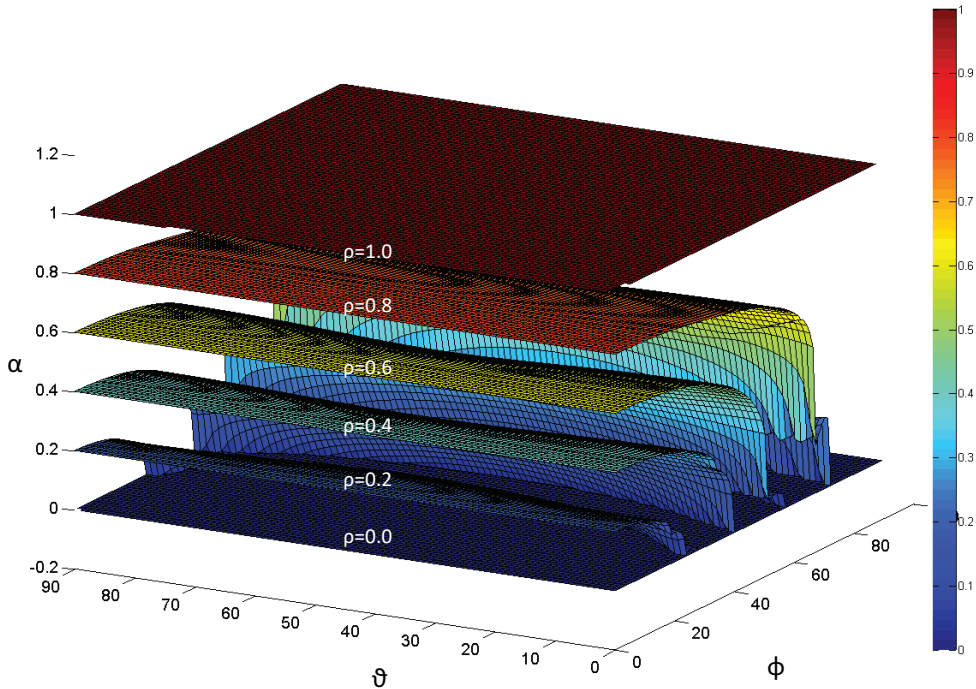The α values are then resampled at the desired values of ρ, see Figure 3.23

Figure 3.23: Dependency of α on cutting plane direction (ϑ and ϕ) and ρ.

As the relative position of the interface with respect to the load direction is not known *a priori*, we average α over the angles ϑ and ϕ defining the intersecting plane direction. To do so we resampled the results in ρ by defining 11 equidistant values in the interval [0,1] for ρ and, for each of them, we computed $\bar{\alpha}$, the arithmetic mean value of α.

The resulting partial volume correction function $\bar{\alpha}$ only depends on the pixel density, see Figure 3.24.

The $\bar{\alpha}$ coefficient is used to correct the piecewise linear relationship between Young's Modulus and pixel values accordig to 3.12. The dependence of the partial volume correction function and relative pixel density, defined as the ratio between the pixel density ρ and that of the material in the bulk ρ_b, versus pixel grey value is schematically shown in Figure 3.24.
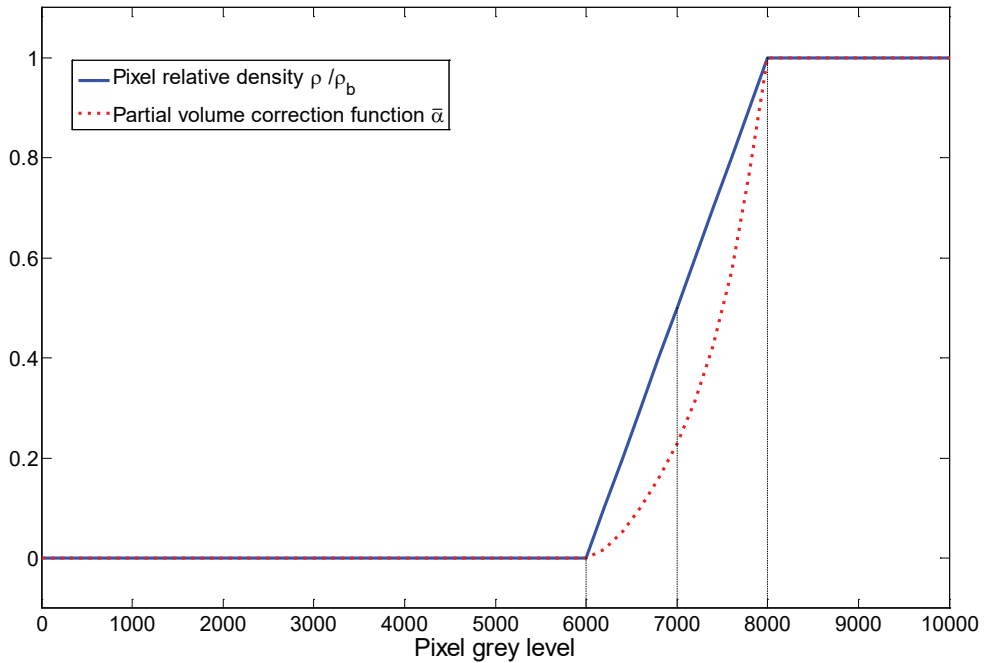

Figure 3.24: Example of pixel relative density and partial volume correction function vs grey level.

3.7. Analysis of the effect of the window thickness

In this section we focus on the sensitiveness of the *cg*FEM virtual characterisation technique to the window thickness, which depends on the level of the uniform Cartesian grid superimposed to the image before the mesh refinement process, see Section 2.2.3. When the initial uniform Cartesian mesh is created, not all the elements outside the CT scan are deleted. Instead, the most internal layer of them is kept whereas the other ones excluded. As a result, the mesh is surrounded by a constant thickness cubic shell of elements, which constitute the window. These window elements are not deleted throughout the refinement process, but they can be *h*-adapted led by the heterogeneity of bitmap elements nearby, which, in contrast, are treated as shown in Chapter 2.2.

The window elements are homogeneous but completely anisotropic in the general case. They all have the same elastic properties and are geometrically similar, like the inner elements in the *geometry-based* version of *cg*FEM and are treated in the same way, see Section 2.1.

We apply the displacement sets shown in Figure 3.1 to the external boundary of the window and compute the mean value of the stress tensor of the bitmap elements. Doing so, we obtain a column of the compliance matrix for each one of the six sets of Dirichlet conditions.

The resulting compliance matrix is then used for the window elements in the following step of the iterative process, which stops when the Frobenius norm of the difference between the compliance matrices computed at two consecutive steps is lower than 1%. We use the rule of the mixture to compute its starting guess values.

In our implementation of the window method, the window thickness is not arbitrary, its values in the numerical examples correspond to three typical levels for the initial Uniform Cartesian grid, level 4, 5 and 6, respectively. These led to the meshes shown in Figure 3.25 after the refinement process, carried out as in Section 2.4.1.

Figure 3.26 shows the sensitivity of some of the elastic properties obtained by homogenisation to the window relative thickness, i.e. the ratio between the window
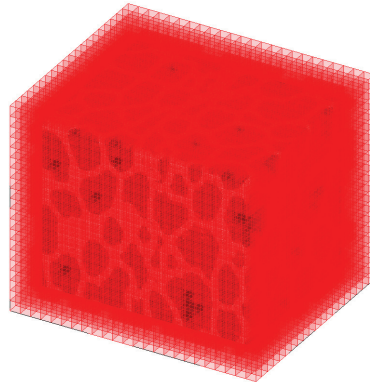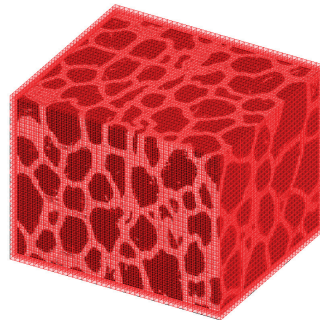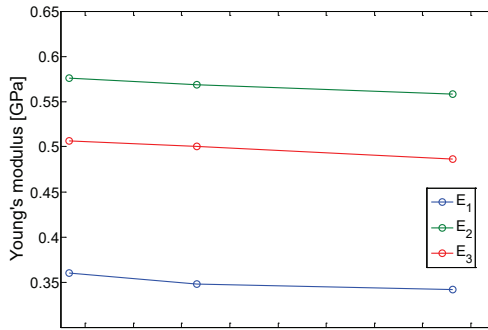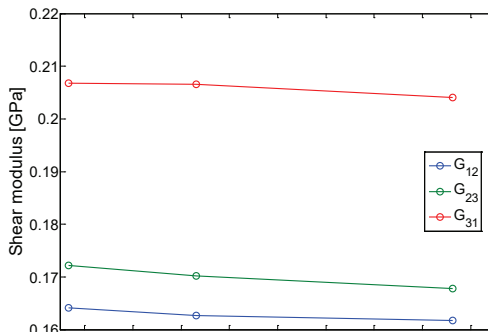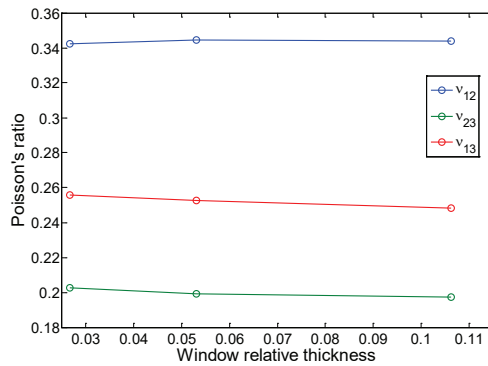
(a)
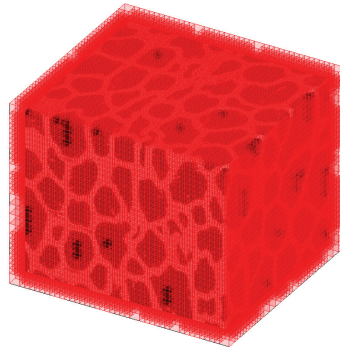
(b)

(c)

Figure 3.25: *cg*FEM meshes for different initial grid levels with the window method. (a) Level 4; (b) Level 5; (c) Level 6.

Figure 3.26: Dependency of the *cg*FEM virtual characterisation technique on the window thickness. (a) Young's modulus; (b) Shear modulus; (c) Poisson's ratio.

thickness and the side of a cube of the same volume as the RVE. The values of the relative window thickness so computed are 0.1063, 0.0531 and 0.0266 for the meshes shown in Figure 3.25 (a), (b) and (c), respectively.

All the meshes are refined up to level 7, which guarantees the number of pixels in each element is $4 \times 4 \times 4$ pixels at least. The relation between the pixel values and elastic properties was obtained for a confidence value of 99.7%, see Figure 3.17 applying the partial volume correction function $\bar{\alpha}$, see Section 3.6.

In the considered thickness range, the sensitivity of the Poisson's ratio as well as the Young's and shear moduli to the window thickness is very low.

3.8. Numerical vs experimental results

The bitmap element integration is carried out with the Riemann-based integration technique (2.2), a sensible choice due to the high amount interfaces in the CT scan.

Figure 3.27 shows the PLA foam Young's modulus values obtained experimentally, see Section 3.3, which are used for the comparison with numerical results obtained with the cgFEM virtual characterisation technique.

The circular and the square markers represent the Young's modulus values obtained by loading and unloading, respectively. The difference between these values is due to local non linear phenomena which are not included in the computation model, therefore we also plot the interval between them, as a dotted line, as it is reasonable to expect an intermediate value from the numerical simulations.

The tests can be distinguished by their colour, as reported in the legend. The horizontal axis in Figure 3.27 refers to the direction along which the specimen was loaded during the test (1, 2 and 3 for directions x, y and z, respectively).

We did not include the first test of the second group (corresponding as a light blue curve in Figures 3.9, 3.10 and 3.11). The corresponding results are not considered reliable as the specimen had already been tested (test one of the first group) and, during the load cycle of the second test, it entered the non linear elasticity range.

In Figure 3.27 the unload case of the Specimen 1 in the first group is missing, as it was not recorded during the test.
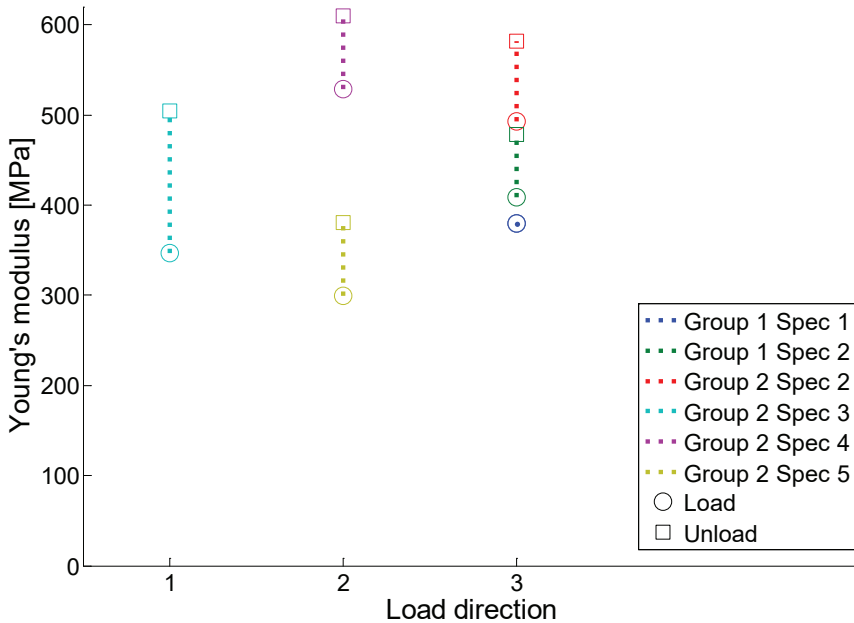
Figure 3.27: Young's modulus values obtained by mechanical testing of the PLA specimens.

The comparison between the experimental and the computational results is shown in Figure 3.28

We plot the *cg*FEM virtual characterisation results as horizontal segments at their respective value on the y-axis and centred on the corresponding direction, x-axis,

The black segment refer to values with the $\bar{\alpha}$ partial volume correction function, whereas for the red ones a piecewise linear relation between Young's modulus and pixel colour. The density-colour relationships for 99.7%, 95% and 68% confidence were used.

As a reference, in Figure 3.29 we also add some semi-empirical results for closed cell foams from the literature, as horizontal dotted lines. The black ones represent the results of Gibson and Ashby [88] obtained under the assumption of periodic structure.
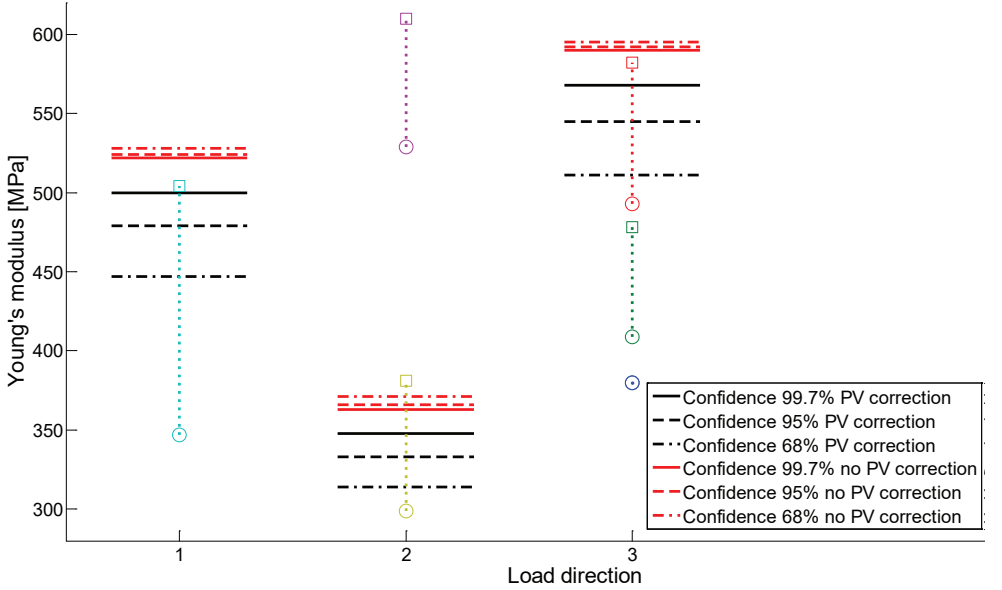
Figure 3.28: Comparison between the Young's modulus values computed with the *cg*FEM virtual material characterisation with and without the partial volume correction function and the experimental results in Figure 3.28.

$$\frac{E}{E_s} \approx \varphi^2 \left(\frac{\rho}{\rho_s} \right)^2 + (1 - \varphi) \frac{\rho}{\rho_s} \qquad (3.14)$$

with and $\nu \approx \frac{1}{3}$. E and ρ are the foam Young's modulus and density respectively, whereas the subindex $_s$ refers to the solid material. φ is the fraction of solid mass contained in the cell edges. Some typical reference values are $0.6 \leqslant \varphi \leqslant 0.8$ for thin wall cells and $0.01 \leqslant \varphi \leqslant 0.07$ for relatively thick wall cells.

The red dotted horizontal line represents the PLA foam expected Young's modulus values according to the formula proposed by Roberts and Garboczi for random closed cell structures [89].

$$\frac{E}{E_s} = 0.694 \left(\frac{\rho}{\rho_s} \right)^{1.54} \qquad (3.15)$$

It is worth noting that both models assume the foam to be isotropic and the pressure of the gas in the cells is neglected.
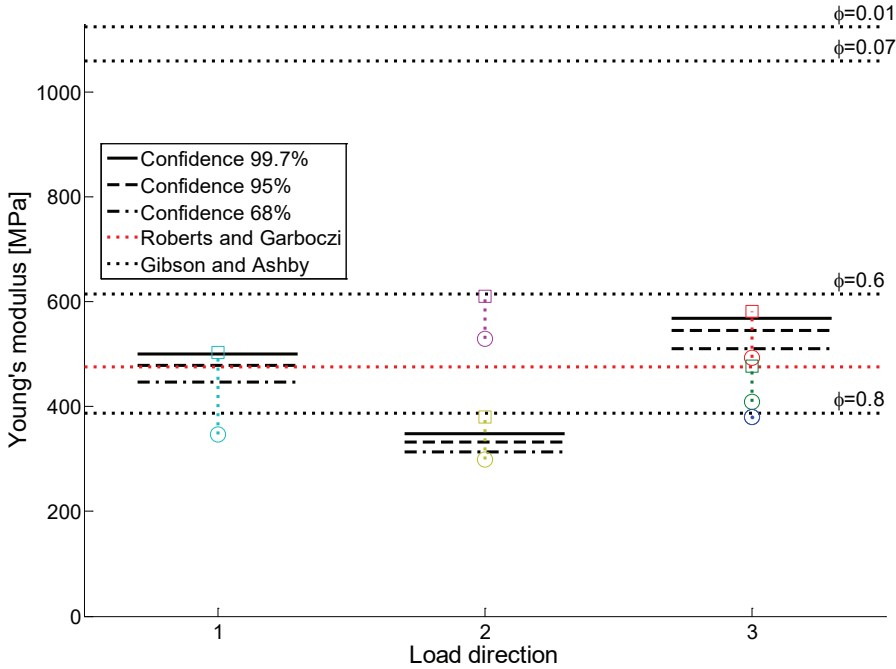
Figure 3.29: Comparison between the Young's modulus values obtained with the *cg*FEM virtual characterisation technique and the semi-empirical formulae in (3.14) and (3.15).

The high dispersion of the experimental results, in particular along the y-direction, makes it clear that more compression tests in all directions are necessary. In spite of that, however, the performance of *cg*FEM virtual characterisation appears reasonably good, especially when the partial volume correction function is used. This avoids the stiffness overestimation which appears when the Young's modulus is considered linearly proportional to the density.

The computed values are reasonable, as shown by the good matching with both the experimental results and semi-empirical formulae, in particular with Roberts and Garboczi's. Compared to these, which assume the foam is perfectly isotropic, our procedure can capture anisotropic behaviour, see Figure 3.30, which is not easily achievable even by mechanical testing. In addition, it is applicable to a much wider

range of heterogeneous materials provided their structure is available as a volumetric image.
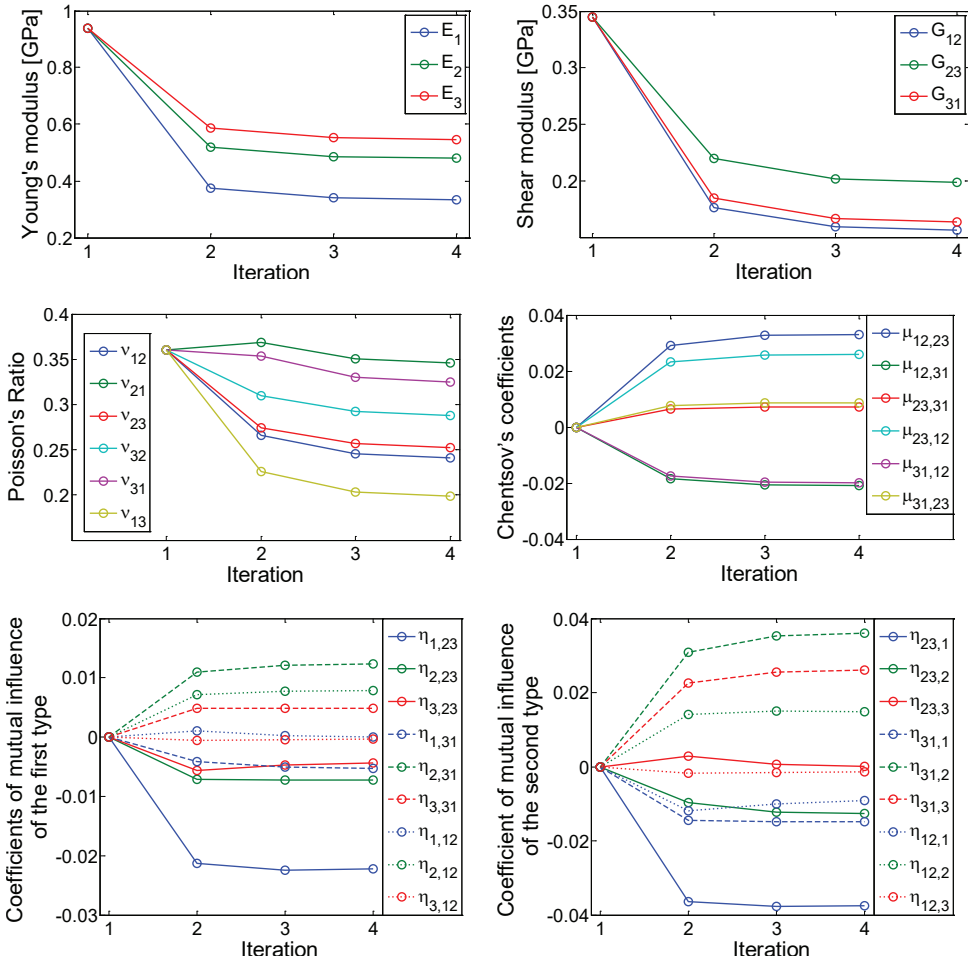
Figure 3.30: Convergence of the technical constants of elasticity over the iterations for a window thickness relative value of 0.0531 and confidence level of 95%.

Figure 3.30 shows the values of the technical constants of elasticity of the homogenised material at each iteration of the window method for the mesh in Figure 3.25a and a confidence level of 95%. The starting points represent the values for the isotropic material obtained by the mixture rule used as an initial guess. After the

first calculation, the window material assumes anisotropic characteristics and converges quickly.

It is worth mentioning that, throughout the process the FE mesh is constant, the only parameter that changes is the compliance matrix of the window elements, therefore the bitmap stiffness matrix has to be computed and assembled during the first calculation only. The integration of the window elements is inexpensive because it is only necessary to compute the element stiffness matrix for one of them and scale it, as in the case of the internal elements in the geometrical version of *cg*FEM, see Section 2.1. The system of equations, in contrast, has to be solved at each iteration.

Chapter 4

Implant Simulation

4.1. Implant simulation with *cg*FEM

A promising application of *image-based cg*FEM is related to the simulation of future implant behaviour.

The procedure is not new, instead it is common enough as testified by the presence on the market of commercial codes, such as Simpleware Scan IP [90], [91], or Materialise Mimics [92], [93], primarily devoted to this application.

The most common strategy to create a patient-specific FE model of a prosthetic device after implantation consists in obtaining a geometrical model from the patient volumetric image by using specific software and assemble the device and biological models together. The result can be meshed as a normal CAD model with standard FE codes, see Figure 4.1.

Again, as in the case of purely anatomical models, the most cumbersome and manual step of the process is the creation of the geometrical model from the volumetric image as well as the next step of manipulating and merging the geometrical models.
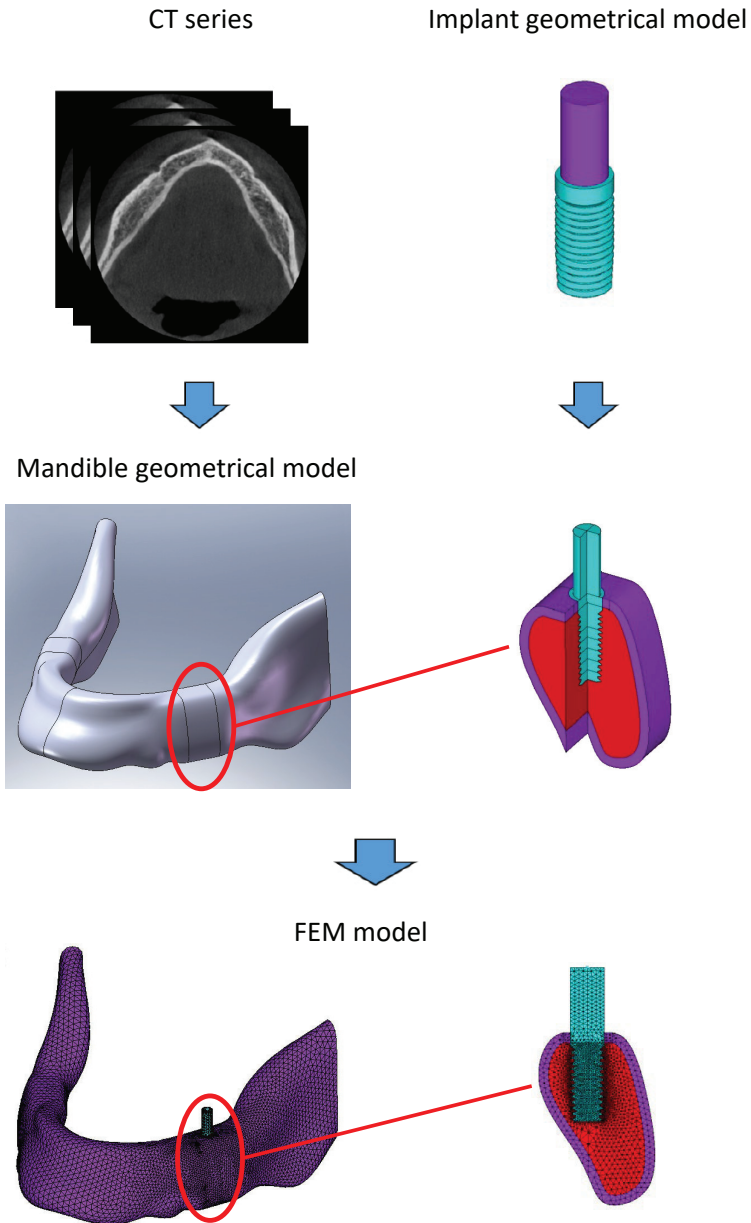
CT series   Implant geometrical model

Mandible geometrical model

FEM model

Figure 4.1: Example of standard implant modelling procedure.

In addition to this standard procedure, as *cg*FEM is capable of providing FE models from both geometry or images, it offers two additional alternative approaches:

- using the bitmap and the CAD to integrate the biological part and the prosthetic device, respectively, in the same FE mesh;

- pixelating the CAD model, superimposing it to the image and treating it as an additional object represented in the medical image.

The first option reduces the preprocessing work required for modelling and is presented in Section 4.2 whereas, the second one is presented in Section 4.3 and takes advantage of commercial codes which make it possible to obtain regular hexahedral meshes from CAD files and reduces the problem to a pure *image-based cg*FEM model.

The following sections show examples for both these procedures.

4.2. Merging image- and geometry-based *cg*FEM for patient specific simulation of future implants

In this Section, we present the details of a procedure which takes advantage of both *geometry-* and *image-based cg*FEM to simulate the effect of future implants and include local tissue information available in the image. The process starts with the image importation and reshape, see Figure 4.2a, in order to make them suitable for the mesh *h*-adaptive process.

The closed geometry representing the prosthetic device is then introduced or defined on the image space and immersed in the Cartesian grid structure which is overlapped to the bitmap, see Figure 4.2b. On the one hand, the pixels whose centre is contained inside the closed geometrical contour are deactivated because they correspond to the parts which have to be removed in order to insert the implant, see Figure 4.3a. On the other hand, the closed geometrical domain is assigned homogeneous material properties as in standard geometry-based *cg*FEM, see Figure 4.3a.
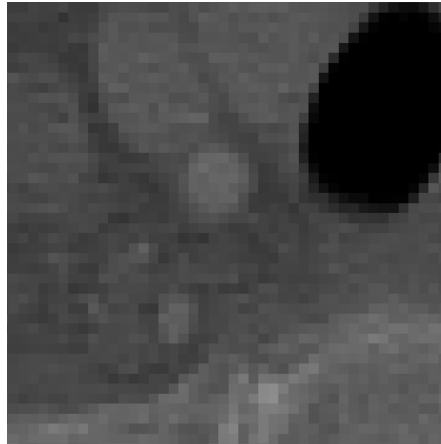
(a)
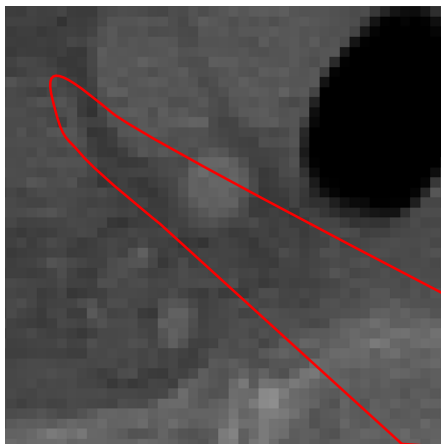
(b)

Figure 4.2: Prosthetic device modelling. (a) Bitmap domain; (b) Geometric contour defined on the bitmap domain.

Once the mesh has been created, three categories of elements are distinguished on the basis of their position with respect to the geometrical domain. As shown in Figure 4.3b, the elements of the hierarchical structure can be external to the geometrical boundary (light grey elements), internal (dark grey elements) or can lie on it (white elements).

(a)

■ Internal elements

□ Elements on the boundary

▨ External elements
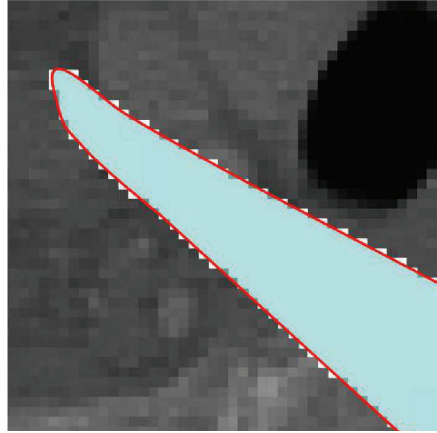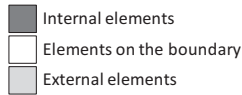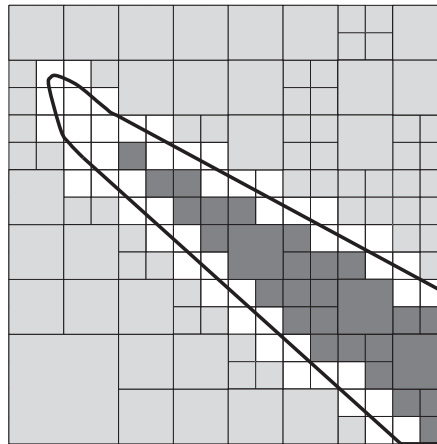
(b)

Figure 4.3: Prosthetic device simulation. (a) Geometric domain and active pixels corresponding to the prosthesis in 4.2; (b) Conceptual image of FEAVox mesh for the geometry-image mixed problem.

On the one hand, the elements inside geometrical domain have proportional stiffness matrices $\mathbf{k}^e$, as in the *geometry-based cg*FEM, see Section 2.1, and are treated
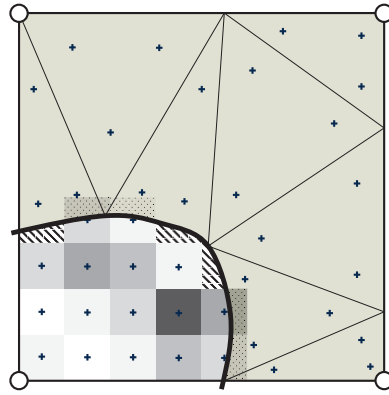
(a)
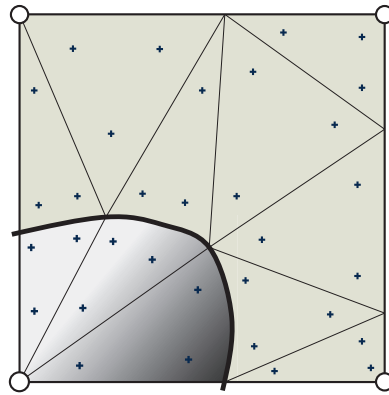
(b)

Geometrical domain		+	Integration points
Image property fitting			Gap between the integration schemes
Geometric boundary			Overlapping areas

Figure 4.4: Representation of the integration procedure adopted on the elements on the contour of a geometrical domain in FEAVox. (a) Riemann Sum approach; b) Least-squares fitting approach.

consequently. On the other hand, the external elements completely lie on the image and their integration follows the procedure described in Section 2. A new class of

elements appears when geometrical and bitmap models are combined: those partially lying on the geometrical domain and containing active voxels.

These are divided in triangular integration sub-domains on the geometric side, as in the *geometry-based cg*FEM while, on the side of the image, one of the the bitmap integration presented in Section 2.2 is applied only to the active pixels, see Figure 4.4.

It is to be noted that, if the Riemann sum or the subdomain decomposition based integration techniques are used, the intersection between geometry and bitmap is not null neither their union perfectly covers the original image, see Figure 4.4a, whereas this does not occurs in the case of least-squares fitting, see Figure 4.4b.

The sudden material change between prosthetic device and biological tissue is detected by the image refinement procedure, hence the mesh is refined in these areas and the inaccuracy associated to the excessive homogenization of the material properties is controlled.

4.2.1. Numerical examples

We will now present numerical examples for 2D and 3D medical images.

4.2.1.1. Hip arthoplasty 2D model

Figure 4.1 shows an application of the method to a 2D problem under plane strain condition. We performed a FE calculation, which simulates the effect of a hip prosthetic device in a femur.

An X-ray image of a femur was used for this purpose, see Figure 4.5a. It was cut out in order to delete the hip joint. The NURBs-based 2D contour was used to define the domain representing a short-stem arthoplasty, see Figure 4.2b. A straight line was defined at the bottom of the X-ray scan to impose a null displacement Dirichlet boundary condition. The implant joint was loaded with a parabolic pressure distribution reaching a maximum value of 10 MPa at the centre of the loaded arc and decreasing to zero at the edges.

The material properties were taken from references [50] and [51] and are shown in Table 4.1.

(a)   (b)
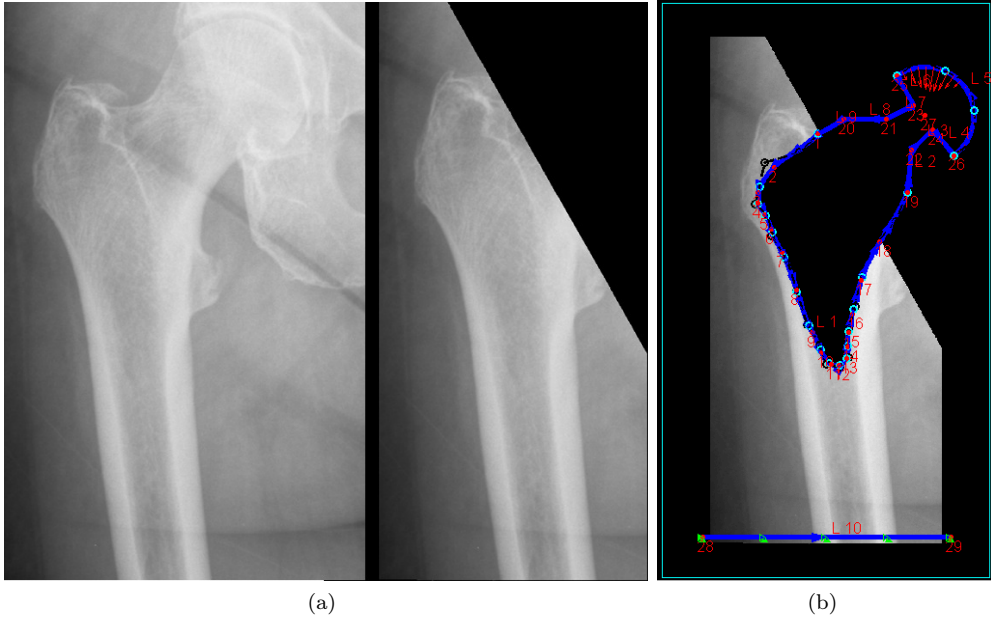
Figure 4.5: Hip implant *cg*FEM model. (a) X-ray of a femur and the same image with the joint removed; (b) Device geometry definition and boundary conditions.

Material	E [GPa]	ν	Gray level
Titanium	116.000	0.32	–
Bone	14.200	0.30	255
Muscle	0.645	0.43	150
Air	0.000	0.0	0

Table 4.1: Material Properties referred to Figure 4.5.

For the creation of the FE model, the bitmap and the geomety were immersed in an initial uniform mesh of level 5 and then an h-adaptive refinement was performed by imposing a value of 0.2 for I_R^e and of 9 for the maximum refinement level allowed. The resulting analysis mesh is shown in Figure 4.6a. Note that although the different living tissues have not been explicitly segmented, the mesh refinement process automatically identifies the boundaries of the tissues and refine the mesh to properly capture their geometry.

The von Mises stress field induced on the system prosthesis-bone by the load is shown in Figure 4.6b.

(a)

(b)
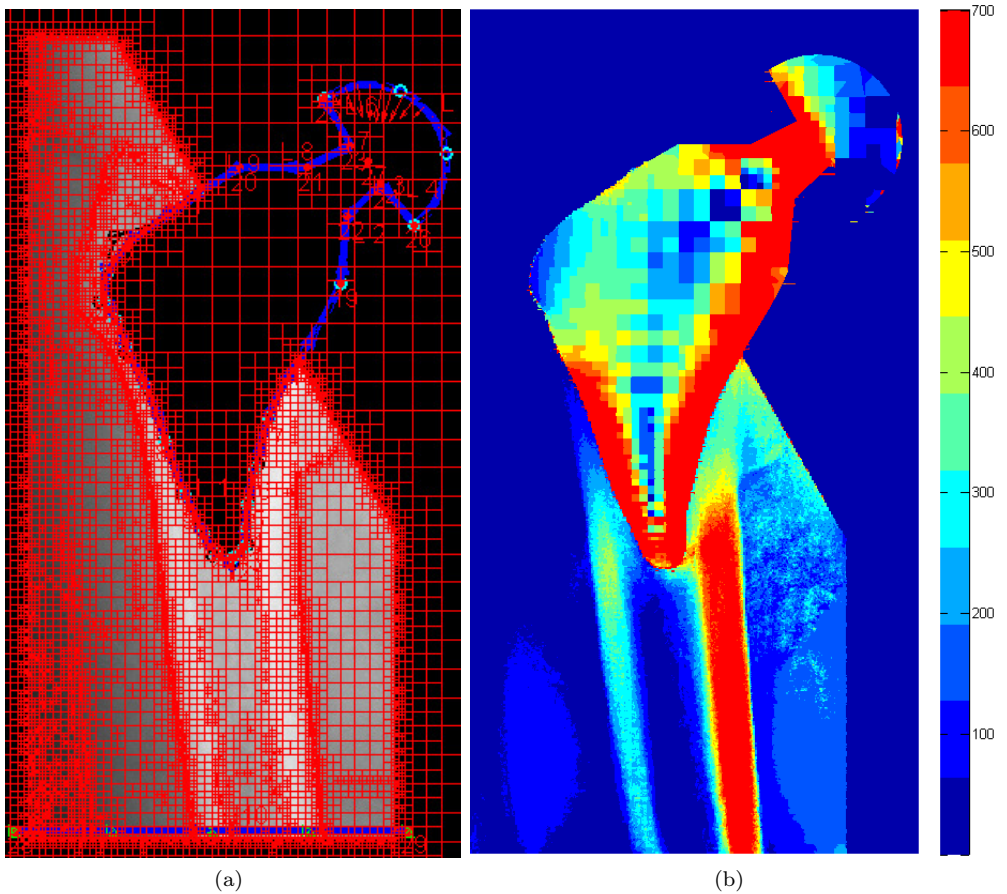
Figure 4.6: Hip implant *cg*FEM model. (a) *h*-adapted mesh; (b) von Mises stress field at the integration points in MPa.

Considering the limitations of the image, the von Mises stress field obtained is reasonable. The compression-bending appears in the stress distribution with higher

values near the edges of the prosthetic device and of the bone and the transfer of momentum from the device to the human tissue. The stress concentration at the neck of the prosthesis was captured.

4.2.1.2. Spinal fusion 2D model

We also present the 2D plane strain simulation of a fixation system used in spine fusion surgeries, see Figure 4.7.

<div align="center">(a)   (b)</div>
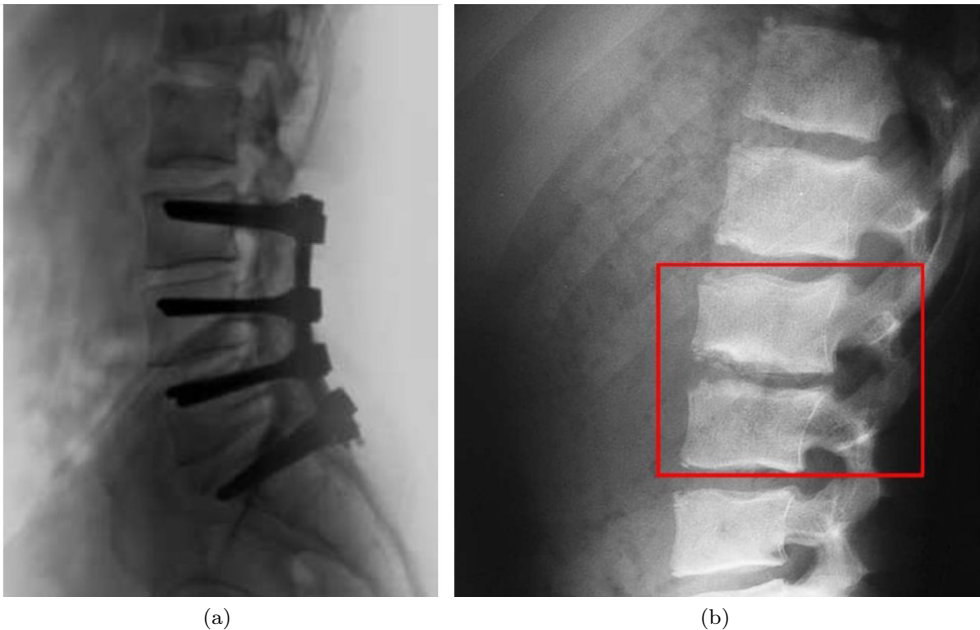
Figure 4.7: Spinal fusion example. (a) Spine implant; (b) X-ray scan region used in the spine impant simulation.

In this case we used the X-ray scan region highlighted in Figure 4.7a. We removed the intevertebral disc and directly defined the implant on the image. As in the previous case the pixels with a centre lying inside the implant domain were automatically deactivated. Additional lines were added to apply null displacement Dirichlet conditions

(a)   (b)
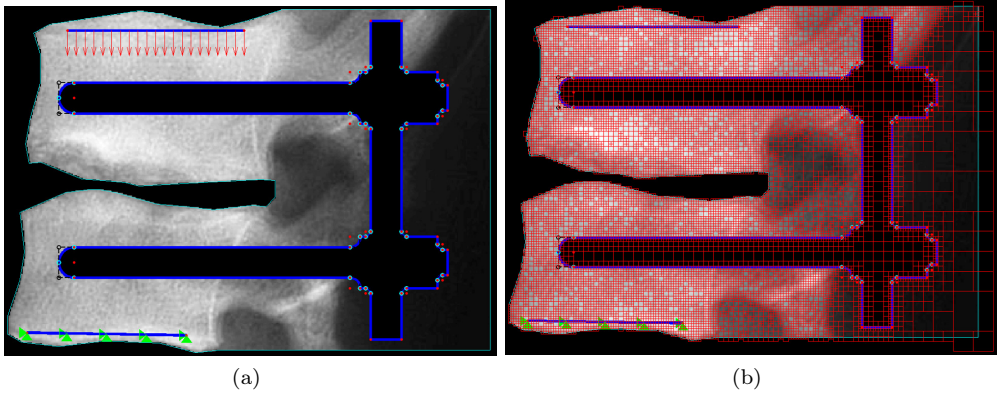
Figure 4.8: Implant fusion modelling stages. (a) Model boundary conditions; (b)
*cg*FEM mesh.

at the bottom of the model and a constant pressure of 1 MPa on the top, see Figure
4.8a.

Figure 4.9: Von Mises stress field.

The material properties were the same as in the previous case. Figure 4.8b shows
the *h*-refined mesh and 4.9 the von Mises stress field. The latter shows the typical
bending pattern in the implant and the load transfer from the vertebrae to the rods.

4.2.1.3. Dental implant 3D model

In this example, a 3D CAD model representing a simplified dental implant is combined with a jaw cone beam computed tomography (CBCT) scan following the procedure described in this section.

CBCT is a volumetric imaging technique especially popular in dentistry. By using conic divergent X-rays, CBCT makes it possible for clinicians to reduce the irradiation doses received by patients by more than 90% in comparison to standard CT scans. This is obtained at the cost of a higher number of artefacts and a lower reliability in the correlation between pxel intensity values and local bone mineral density.

We use the 3D NURBs-based CAD model of a simplified dental implant, see Figure 4.10b and the subregion highlighted in Figure 4.10a of the segmented jaw CBCT scan used for the simulation in Section 2.4.3.

The CAD model was immersed into the portion of the CBCT scan, the voxels contained in the device volume were deactivated in the corresponding logical sub-matrix from the segmentation process. The assembly and the corresponding h-adapted FE mesh are shown in Figure 4.11. Homogeneous Dirichlet Boundary conditions are enforced upon all the DOFs of the nodes lying on the green surfaces in Figure 4.11a and a distributed load with components of -2 MPa in the y and z directions is applied on the CAD model surface highlighted in red.

The bitmap and the geometry were initially immersed in a uniform mesh of level 4 and then an h-adaptive refinement was performed by imposing $I_R^e \leq 0.2$. The maximum refinement level allowed was 5.
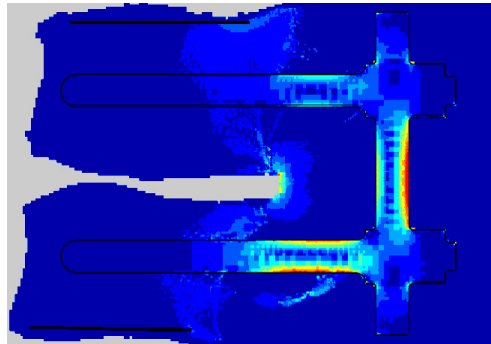
The same material properties as in the previous problem were used for the CBCT scan, see Section 2.4.3, except for the prosthesis which was assumed to be made of titanium and, as a consequence, was assigned a Young's modulus and a Poisson's ratio of 110 GPa and 0.32 respectively. The least-square integration scheme was used for the CBCT scan. In the elements cut by the CAD model the integration was performed by decomposition in tetrahedral subdomains on both sides of the interface, see Figure 4.4b. The subdomains on the interface were integrated by using the NEFEM-integration techniques as described by [34].

Figure 4.12a shows the von Mises stress distribution of the assembly. In order to make visible the stress distribution inside the bone, the CBCT scan was cut with the grey plane shown in Figure 4.11a and only the front of the bitmap is shown. The von
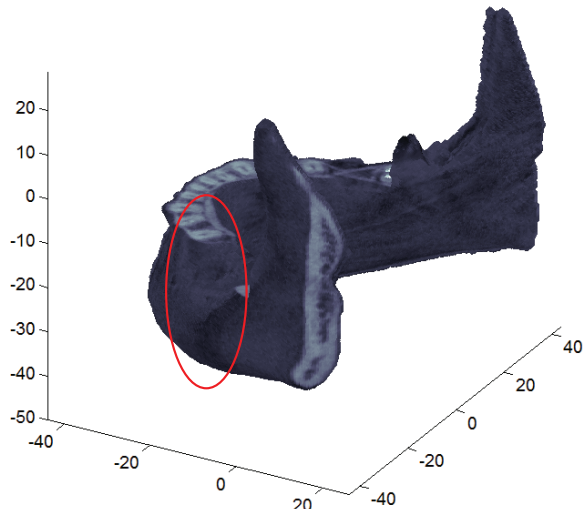
(a)
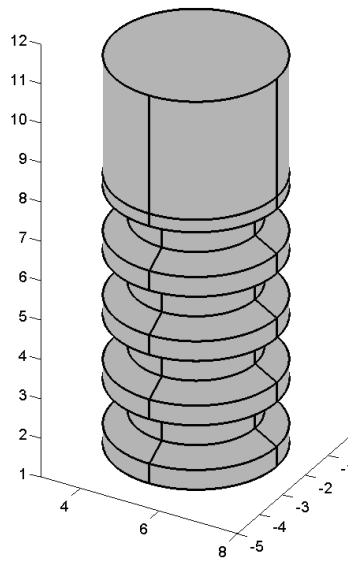
(b)

Figure 4.10: Dental implant simulation model components (position is expressed in mm). (a) Part of the CBCT, see Figure 2.24, used in this simulation; (b) Screw simplified CAD model.
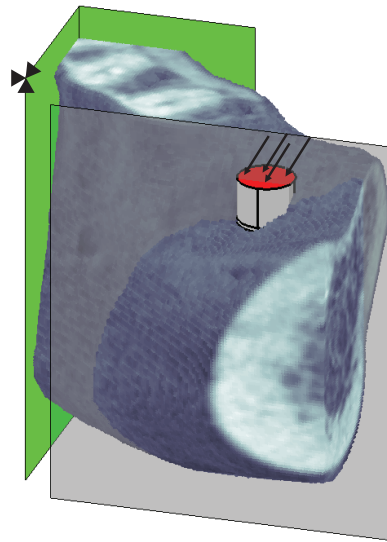
(a)
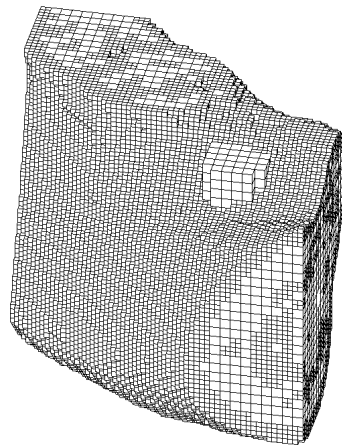
(b)

Figure 4.11: Jaw CBCT scan based model. (a) Segmented jaw with boundary conditions; (b) FEAVox h-adapted mesh.

Mises stress distribution in the prosthetic device is magnified in Figure 4.12b. The
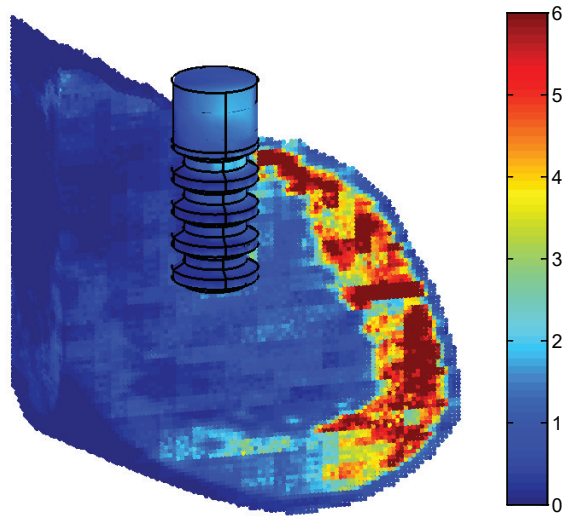
(a)
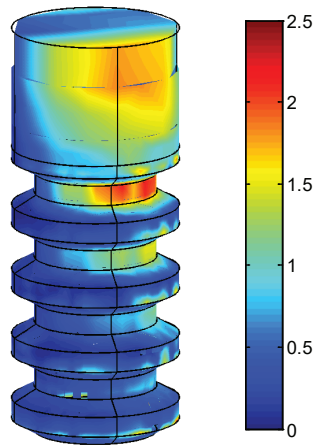
(b)

Figure 4.12: Dental implant von Mises stress field expressed in MPa. (a) Front section of Figure 4.11a; (b) Prosthetic device detail.

typical load transfer between the implant and the cortical bone at the implant upper threads and the lower stress state at the interface between the deep trabecular bone

and the screw tip are visible. The stress map is plotted differently for the CBCT scan and and the CAD model. In the former the strain values are computed at the centre of the pixels and the $\mathbf{D}$ matrix associated to the pixel is used to compute the stress in that position. In the latter, in contrast, we use the SPR technique to obtain a C_0 continuous stress field. For representation purposes only, this is computed at the vertices of the external faces of the integration tetrahedra, represented as finer facets. This example shows how suitable *cg*FEM is for the simulation of osteointegrated implants in a patient specific framework. The method makes it possible to directly locate the implant CAD model on the volume of the bitmap model of the mandible to obtain a conjoined model. On the one hand, *cg*FEM eliminates the necessity of further manipulation of the models and, on the other hand, it takes advantage of the specific strengths of each of them: the detailed spatial distribution and the elastic properties provided by the CT scans exact geometrical representation of the CAD.

4.3. Pixelation of CAD models

In this section we follow a different procedure to introduce implants in *image-based* *cg*FEM models. Instead of directly combining the image and the geometrical information as in the previous section or a CAD model obtained from image segmentation with the implant one, as in the vast majority of the applications, we introduce the implant information into the medical image and directly use the *image-based* version of *cg*FEM. This procedure includes a preliminary stage, at which we use the pre and post-processing commercial software GiD [94], [95], [96] combined with an in-house Matlab-based preprocessing code. The latter makes it possible to manually locate the implant in the CT scan, as it is usually done in surgical planning, and provides the solid body motion parameters which are used by GiD to convert the implant model into a uniform Cartesian mesh which perfectly fits the CT scan spatial distribution by using GiD Cartesian meshing tool. The corresponding voxels in the CT scan are assigned the Hounsfield scale values corresponding to titanium. The resulting volumetric image is suitable for *image-based cg*FEM simulations. Figures 4.13 and 4.14
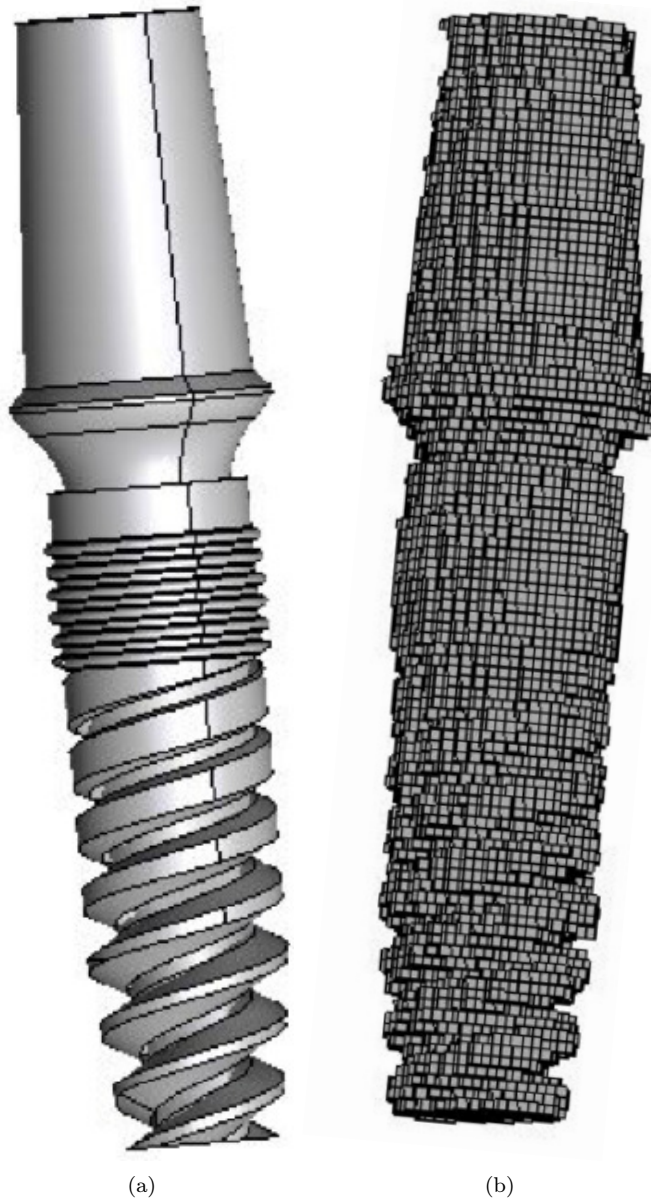
Figure 4.13: Dental implant. (a) CAD model; (b) Voxelised model.
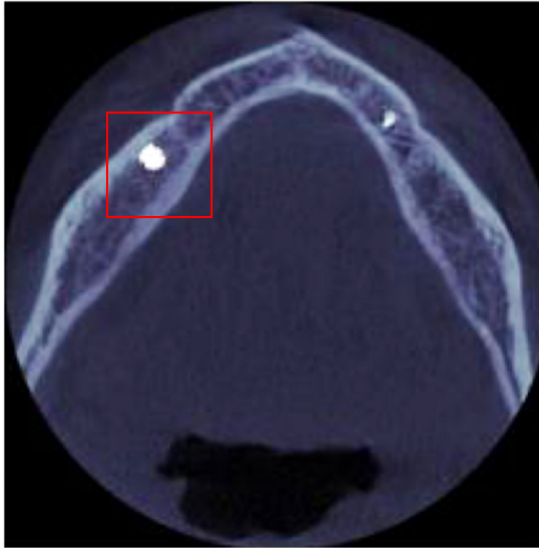
(a)

(b)

Figure 4.14: Dental implant position. (a) Axial plane; (b) Sagittal plane.

show the pixelization of a dental implant and the final CT scan containing the implant in the proper position respectively.

The procedure is obviously less accurate in the geometrical representation of the prosthetic device, which is pixelized at the same resolution as the CT scan, nevertheless we consider it to be precise enough for the application addressed in the following section.

4.3.1. Application to preoperative assessment of dental implant stability

In this section, we propose an image-based biomarker for the preoperative assessment of bone quality, which will provide information about whether the area, which will host the future implant, guarantees the proper stability to the device or not.

The biomarker is based on the assumption that bone elastic behaviour in the area surrounding the implant has a prominent role in its stability and a strong effect on its vibrational behaviour [97].

We compute the isolated device natural vibration modes and quantify the surrounding bone quality by analysing the effect of its stiffness on the natural frequencies. We do not include the mass in the model of the bone because the simulation of the actual vibrational physical behaviour of the implant exceeds the scope of this work and would probably make it harder by introducing a great amount of new low frequency modes not related to the implant stability.

The natural frequencies associated to the deformation modes of a metal implant are expected to be much higher than those of the surrounding bone due to difference of stiffness, as a consequence the low frequencies would have to be discarded. On the other hand, we are not interested in simulating the implant-tissue behaviour, but only to determine a bone quality parameter.

To achieve this goal, we base our method on the evaluation of the implant natural frequencies alone introducing the contribution of the surrounding biological material to the system stiffness ignoring its density.

In the following, we use the Riemann sum integration, see Section 2.2 for the integration of both the element stiffness and the mass matrices $\mathbf{k}^e$ and $\mathbf{m}^e$. The element mass matrix, see Equation 4.1, is written as a function of the FE discretisation

Device f_1 f_2

Modes and natural frequencies

(a)

Device in bone $f_1 + \Delta f$ $f_2 + \Delta f$

Modified modes and frequencies

(b)
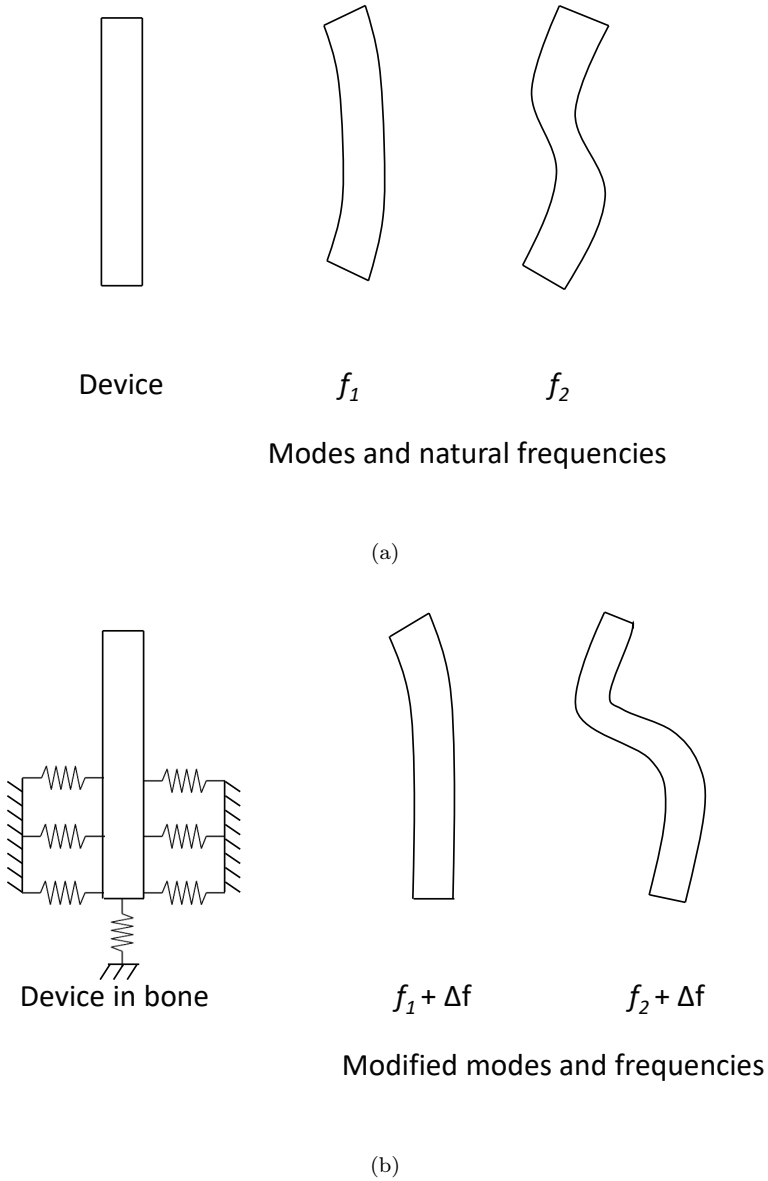
Figure 4.15: Scheme of implant natural frequencies and modes change due to the surrounding bone. (a) Free device; (b) Implanted device.

functions $\mathbf{N}(\boldsymbol{\xi}_i)$ computed at the centres of the voxels, the determinant of the Jacobian matrix $| \mathbf{J}(\boldsymbol{\xi}_i) |$ of the element and the quadrature constant weights w_i and the density ρ associated to each pixel.

$$\mathbf{m}^e \quad = \quad \sum_{i=1}^{IP} \rho(\boldsymbol{\xi}_i)\mathbf{N}^T(\boldsymbol{\xi}_i)\mathbf{N}(\boldsymbol{\xi}_i) \mid \mathbf{J}(\boldsymbol{\xi}_i) \mid w_i$$

(4.1)

In all the simulations in this section, the value of ρ is 4506 kg/m^3 inside the device, which is assumed to be made of titanium, whereas outside the implant ρ is considered null.

We follow the well known procedure of writing the unconstrained and unloaded dynamic problem

$$\mathbf{M\ddot{u} + Ku = 0}$$ (4.2)

in the frequency domain

$$(\mathbf{K} - \omega_n^2\mathbf{M})\mathbf{\tilde{U}}_n = \mathbf{0}$$ (4.3)

with the assumption of purely harmonic motion $\mathbf{u}(t) = \sum_n \mathbf{\tilde{U}}_n e^{i\omega_n t}$, justified by the absence of dumping. Since the system is not restrained, the six lowest frequency modes are the rigid body motion degrees of freedom, and can be discarded.

We applied the method to the dental implant in Figure 4.13, which is located as shown in Figure 4.14.

Tables 4.2 show the lowest eight natural frequencies apart from the solid body motion modes, for the device alone or surrounded by bone respectively. The corresponding modes are shown in Figures 4.17 and 4.18.

A general increase in the natural frequencies is apparent. Even though the low frequency bending modes are easily recognisable, the higher frequencies modes have a different order or shape.

We want to find modes whose natural frequencies can be used as a biomarkers of the surrounding bone support capability.

Mode number	Frequency [Hz]	Label	Mode number	Frequency [Hz]	Label
7	37865	a	7	61481	a
8	38384	b	8	62494	b
9	77235	c	9	111004	c
10	85459	d	10	114837	d
11	87351	e	11	119744	e
12	119828	f	12	127315	f
13	140642	g	13	167891	g
14	142552	h	14	171070	h

(a) free device. See figure 4.17   (b) device and surrounding bone. See figure 4.18

Table 4.2: Frequency values of the first eight non-rigid body motion modes of the dental implant alone (a) and surrounded by bone (b).
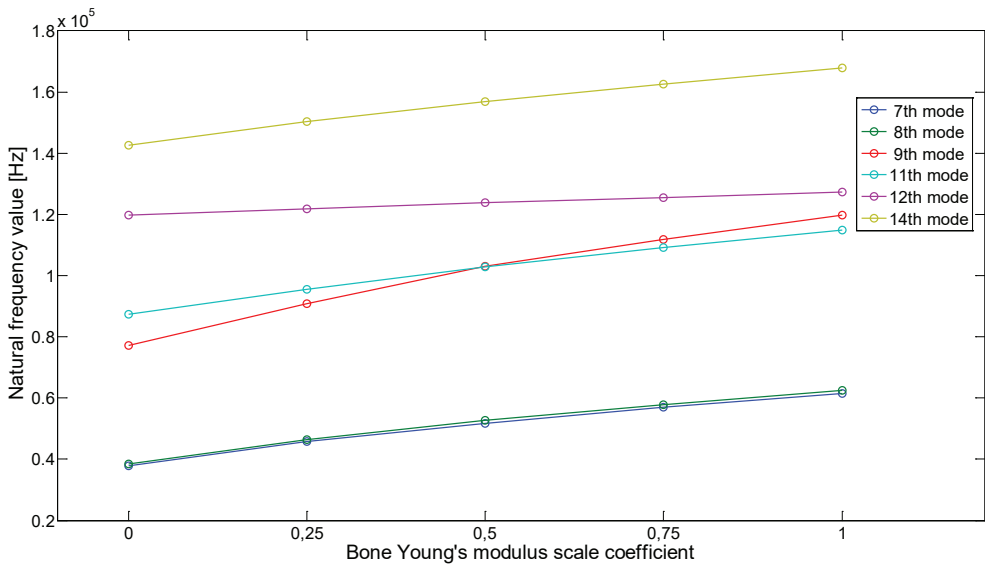
Figure 4.16: Natural frequencies of dental implant versus bone Young's modulus scale coefficient.

(a)   (b)   (c)

(d)   (e)   (f)

(g)   (h)
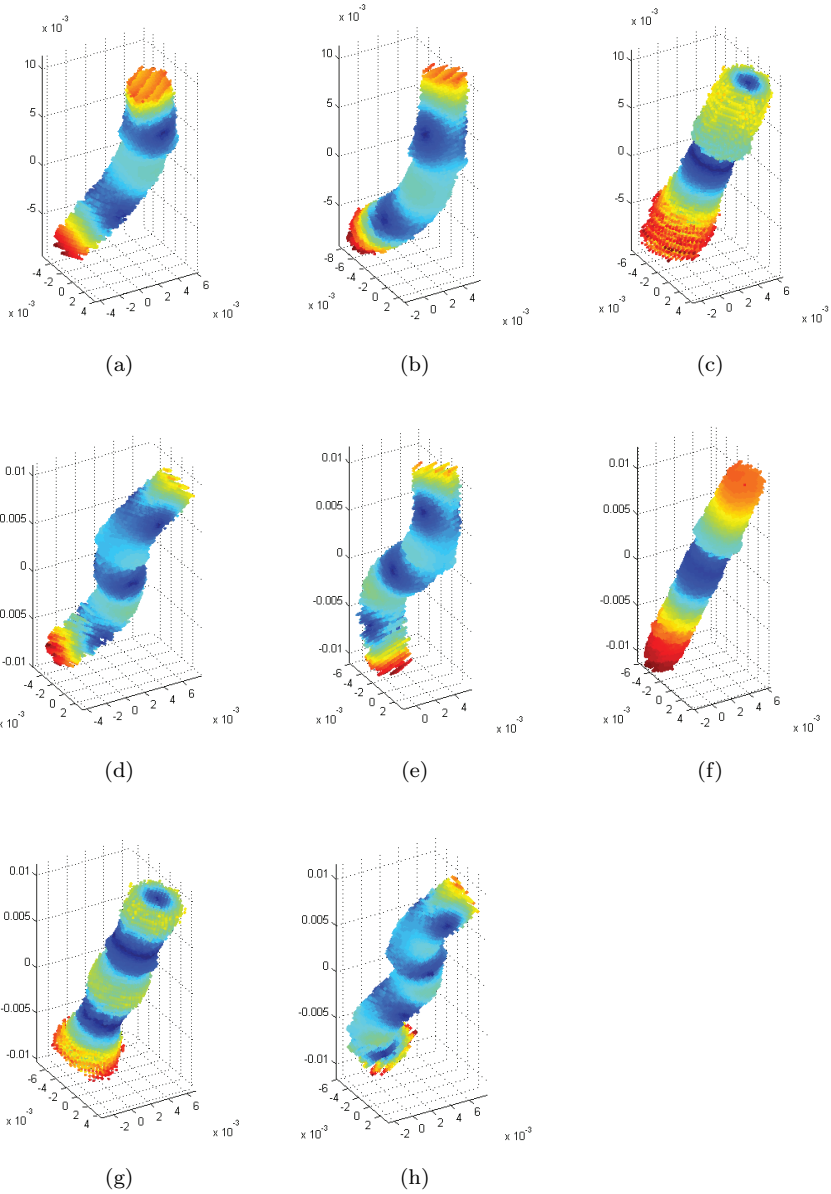
Figure 4.17: Dental implant alone vibration modes of first non rigid body motion lowest natural frequencies. The corresponding natural frequencies are shown in Table 4.2a.
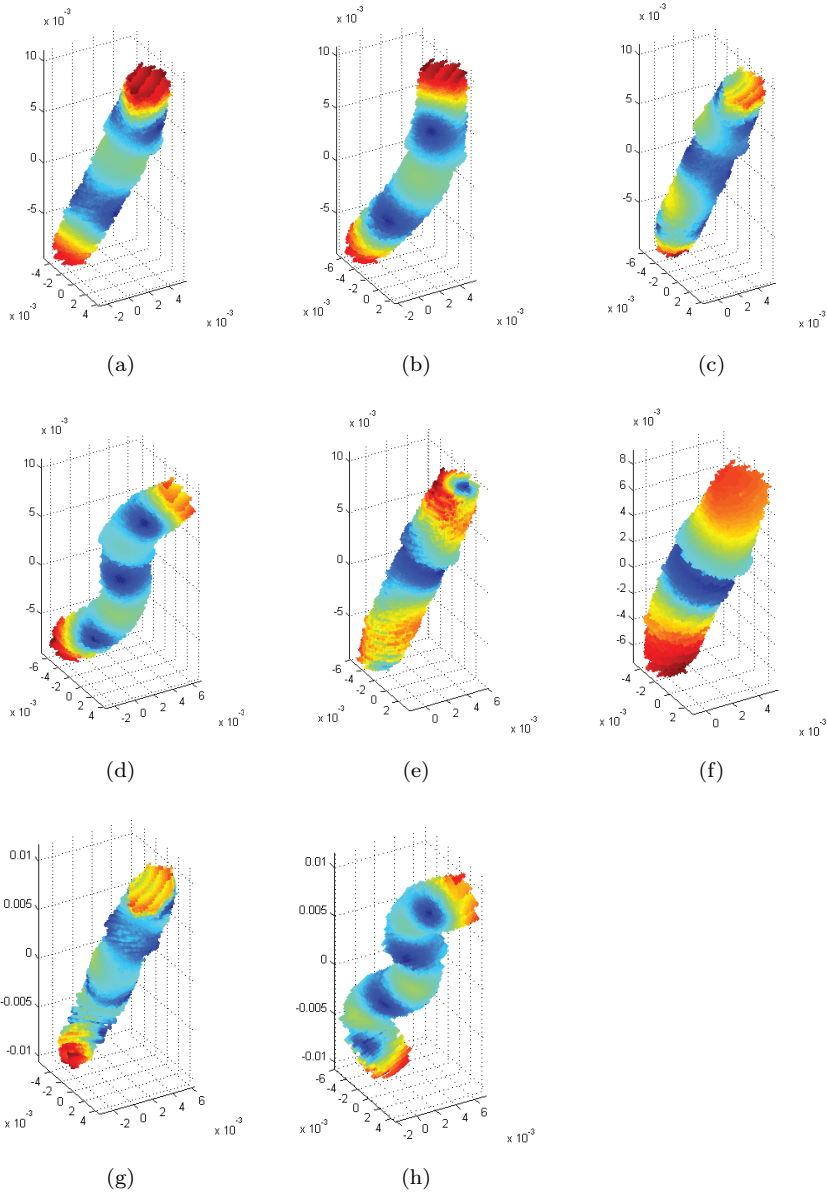
Figure 4.18: Dental implant surrounded by bone vibration modes of first non rigid body motion lowest natural frequencies. The corresponding natural frequencies are shown in Table 4.2b.

These modes have to be recognisable, that is undergo a limited shape change when surrounding bone is introduced in the simulation. At this preliminary stage we focus on the lowest 8 modes (excluding the 6 rigid body motion). If we only take into account the most recognisable flexion modes (a) and (b), we notice an increase of 62% for both of them. In order to check the viability of the method, we study the sensitivity of the implant natural frequencies to the surrounding bone stiffness. To do so, we repeat the natural frequency analysis of the implanted devices multiplying the bone Young's modulus by a scaling coefficient k, and evaluate its effect on the natural frequencies. Prior, it is necessary to use the Modal Assurance Criterion (MAC), [98], [99], [100], to check which modes are comparable between two calculations carried out with different k values. As the modes are ordered from the lowest frequency to the highest, the use of MAC technique is necessary to track the mode along the k value change. It can happen that, due to the effect of the surrounding tissue stiffness, the order of consecutive modes changes.

When the surrounding tissue stiffness increases one of the modes can stop to be fully recognisable in the set of the new modes taken into account. In this case we just discard it.

The modes from the seventh to the fourteenth were computed for k values of 0, 0.25, 0.5, 0.75 and 1. Each of the 8 modes for $k = 0$ was compared with all the other modes with different k values with the MAC technique. The results are shown in Figure 4.19 for modes seventh to tenth and in Figure 4.20 for eleventh to fourteenth. In the following we will refer to each mode by its order in the case of the implant alone ($k = 0$).

The shape and order is substantially unchanged for modes seven, eight and twelve. The order changes for the eleventh and ninth modes between $k = 0.25$ and $k = 0.5$ and between $k = 0$ and $k = 0.25$ for the fourteen mode. In both cases, the mode shapes are still easy to track. Instead, the mode is not as clear for modes 9, 10 and 13 in the mode range taken into account and, consequently, these modes are discarded. Figure 4.16 shows the frequency change corresponding to modes 7, 8, 9, 11, 12 and 14.

The least sensitive one is the axial deformation mode 12, whereas the others all have some bending and twisting component and show a similar behaviour as the surrounding tissue stiffness increases. In particular, in the range considered, the mode which increases its natural frequency the most is the twist mode 9. Nevertheless the
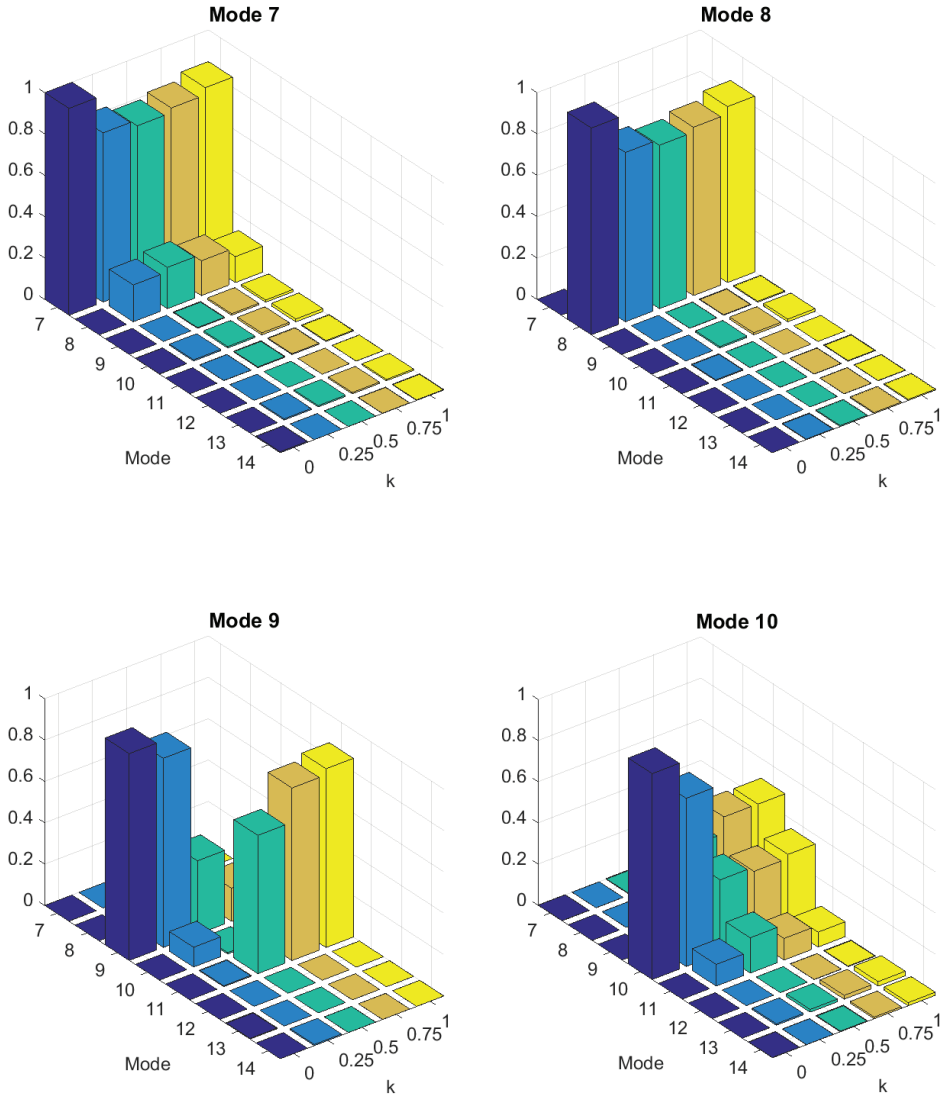
Figure 4.19: Dental implant natural vibration modes MAC comparison. Modes from 7 to 10

highest relative frequency change can be found for the low frequency bending modes 7 and 8.
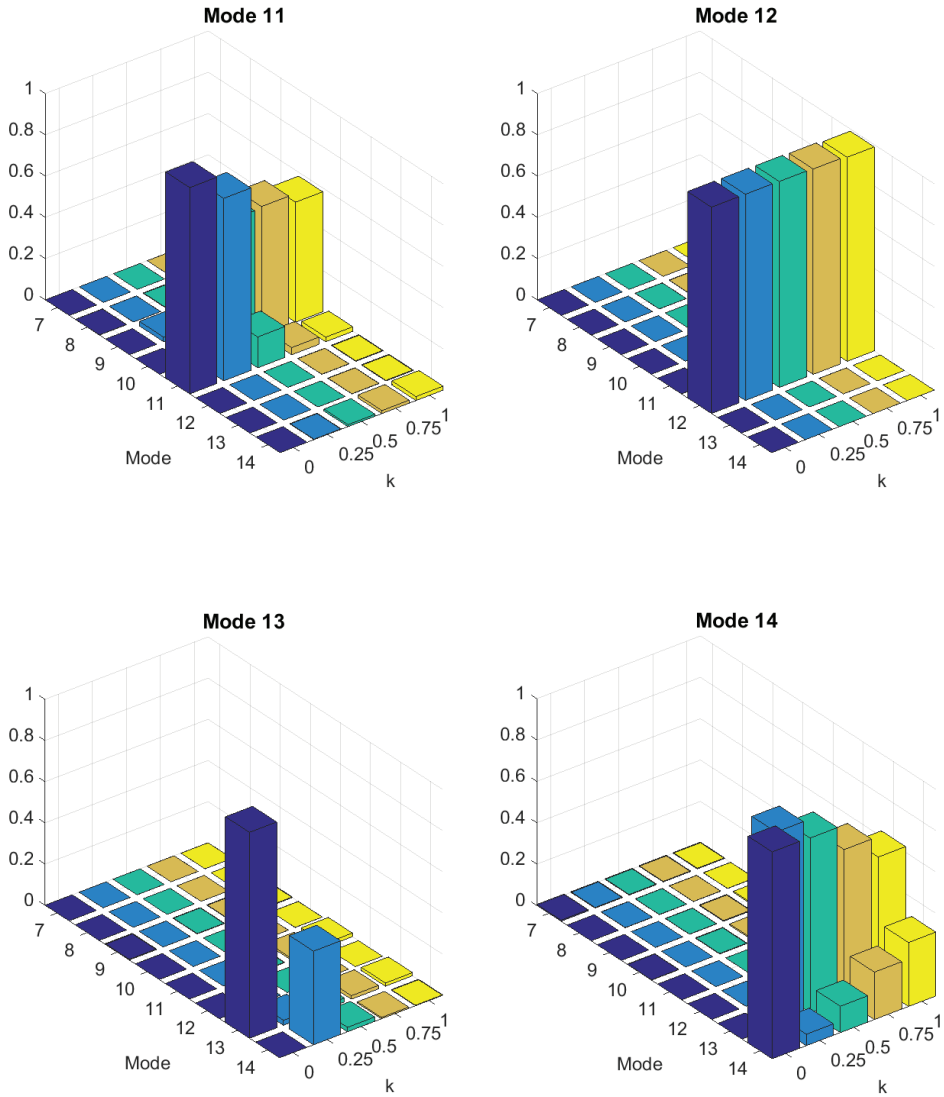
Figure 4.20: Dental implant natural vibration modes MAC comparison. Modes from 11 to 14

4.3.2. Stability of hip endoprosthesis

The same analysis was carried out on the the hip device model in Figure 4.21.

<div align="center">(a)   (b)</div>
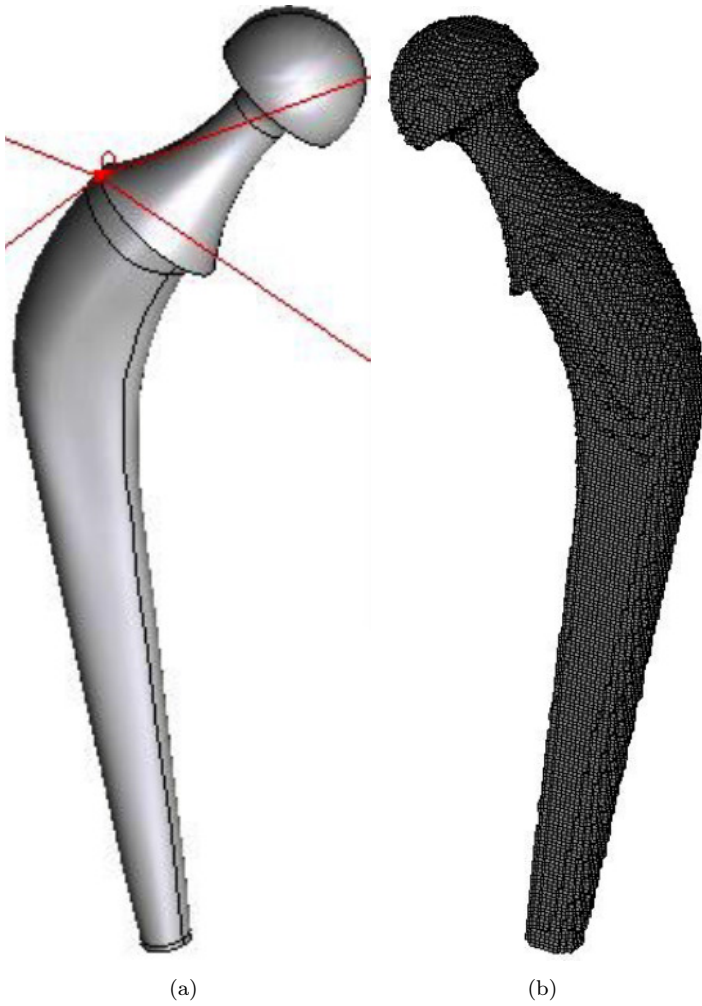
Figure 4.21: Hip inplant implant. (a) CAD model; (b) Voxelised model.

Table 4.3 shows the low frequencies for the hip model alone and surrounded by bone.

Mode number	Frequency [Hz]	Label	Mode number	Frequency [Hz]	Label
7	2403	a	7	3347	a
8	2675	b	8	4713	b
9	5209	c	9	6354	c
10	5445	d	10	7643	d
11	7261	e	11	8168	e
12	8408	f	12	12077	f
13	9081	g	13	12549	g
14	10618	h	14	16709	h

(a) free device. See figure 4.23   (b) device and surrounding bone. See figure 4.24

Table 4.3: Frequency values of the first eight non-rigid body motion modes of the hip implant alone and surrounded by bone.

As expected all the frequencies increase with the stiffness of the surrounding tissue, see Figure 4.22.
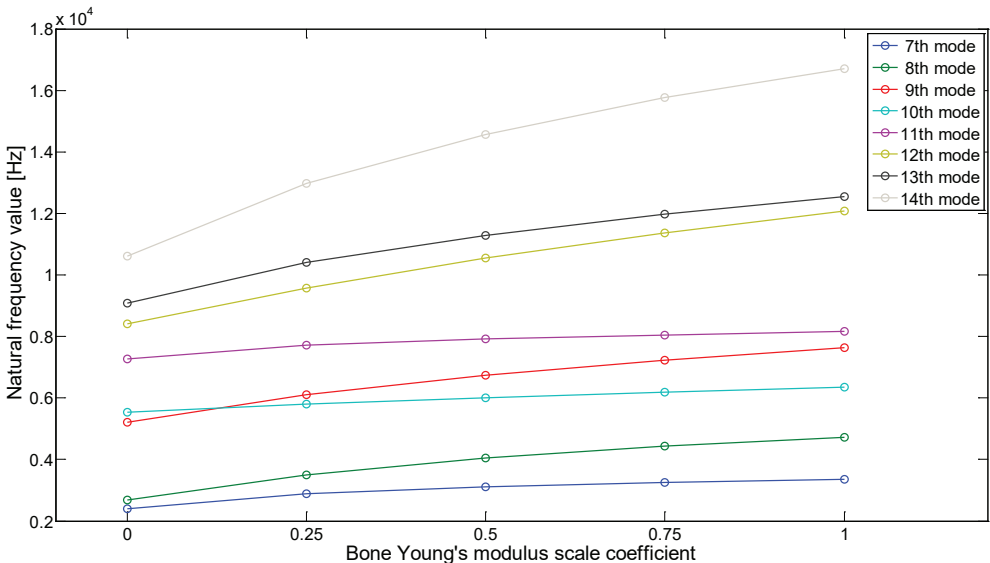
Figure 4.22: Natural frequencies of hip implant versus bone Young's modulus scale coefficient.

Natural frequencies are listed in table 4.3 for $k = 0$ and $k = 1$ respectively, whereas the corresponding mode shapes are shown in Figures 4.23 and 4.24.
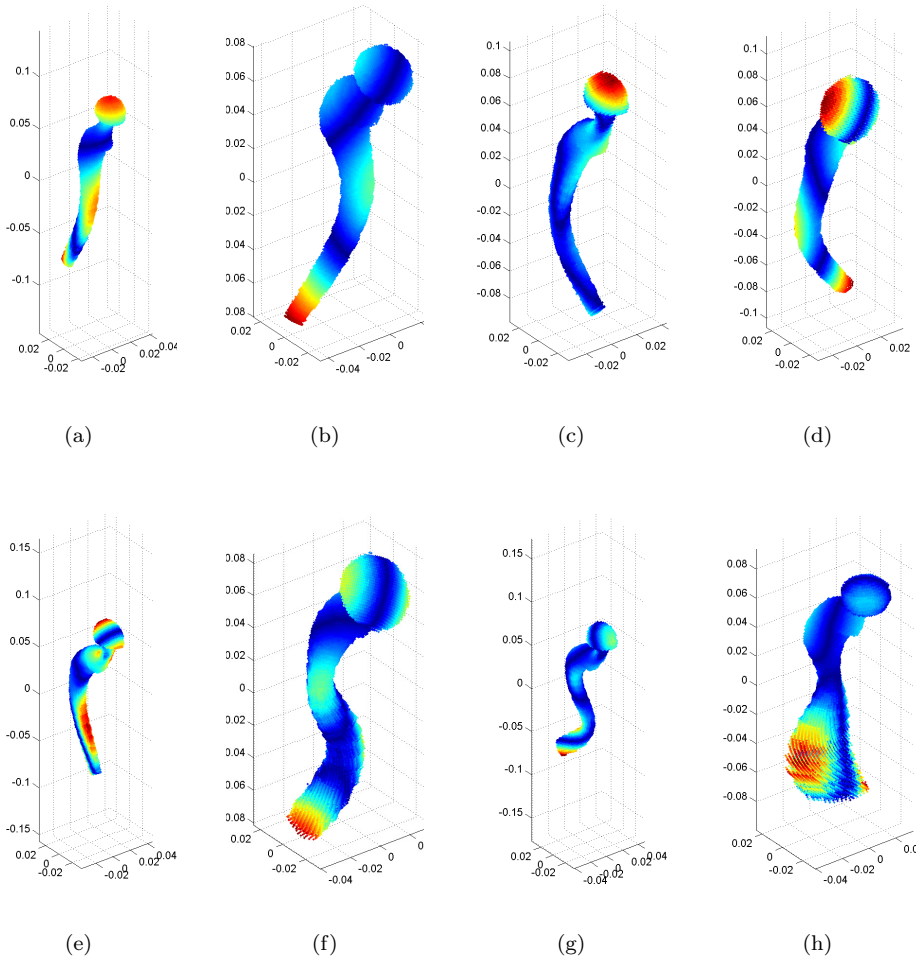
Figure 4.23: Hip implant alone vibration modes of first non rigid body motion lowest natural frequencies. The corresponding natural frequencies are shown in Table 4.3a.

The lowest 8 natural frequencies, not associated to rigid body motion modes, are shown in Table 4.3 and the corresponding modes in Figures 4.23 and 4.24.
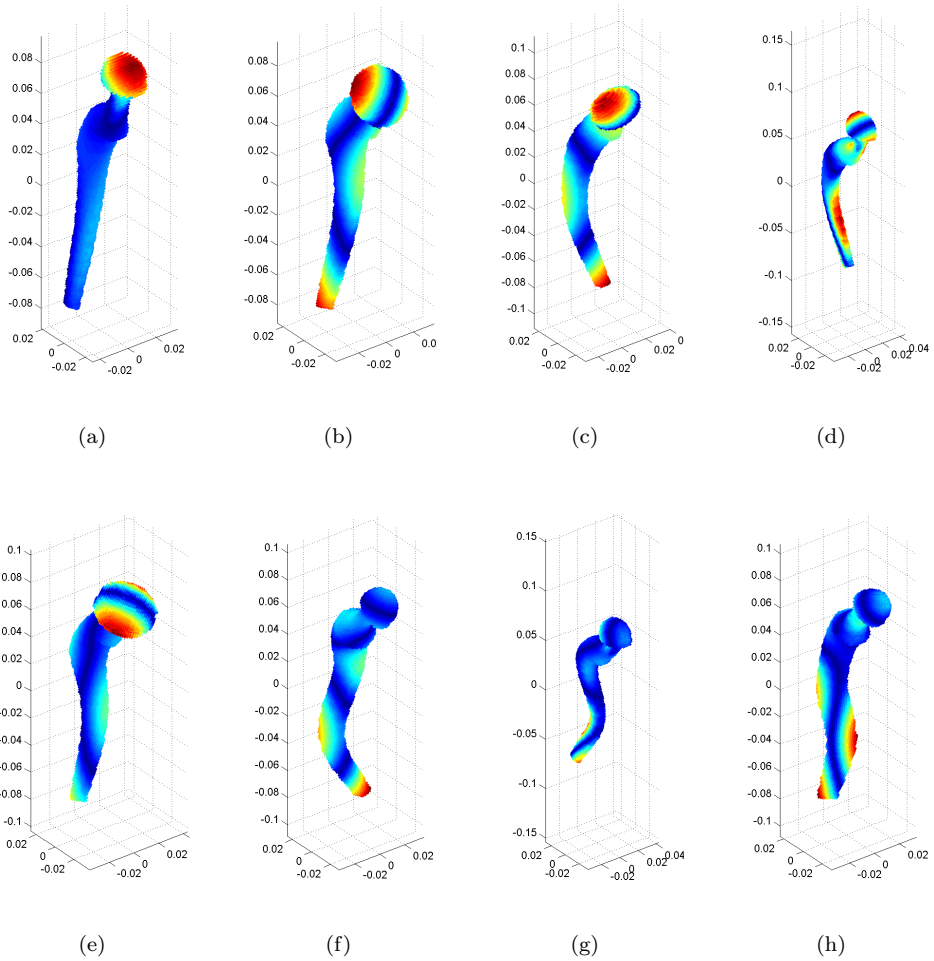
Figure 4.24: Hip prosthesis surrounded by bone vibration modes of first non rigid body motion lowest natural frequencies. The corresponding natural frequencies are shown in Table 4.3b.

The Mode Assurance Criterion for the lowest 8 non-rigid body modes of the hip device in Figures 4.26 and 4.25 shows that, differently from the dental implant, the modes stay easily recognisable as the surrounding tissue becomes stiffer. In addition,

with the only exception of modes 9 and 10, which invert their order between $k = 0$ and $k = 0.25$, all the other modes considered do not change their order.
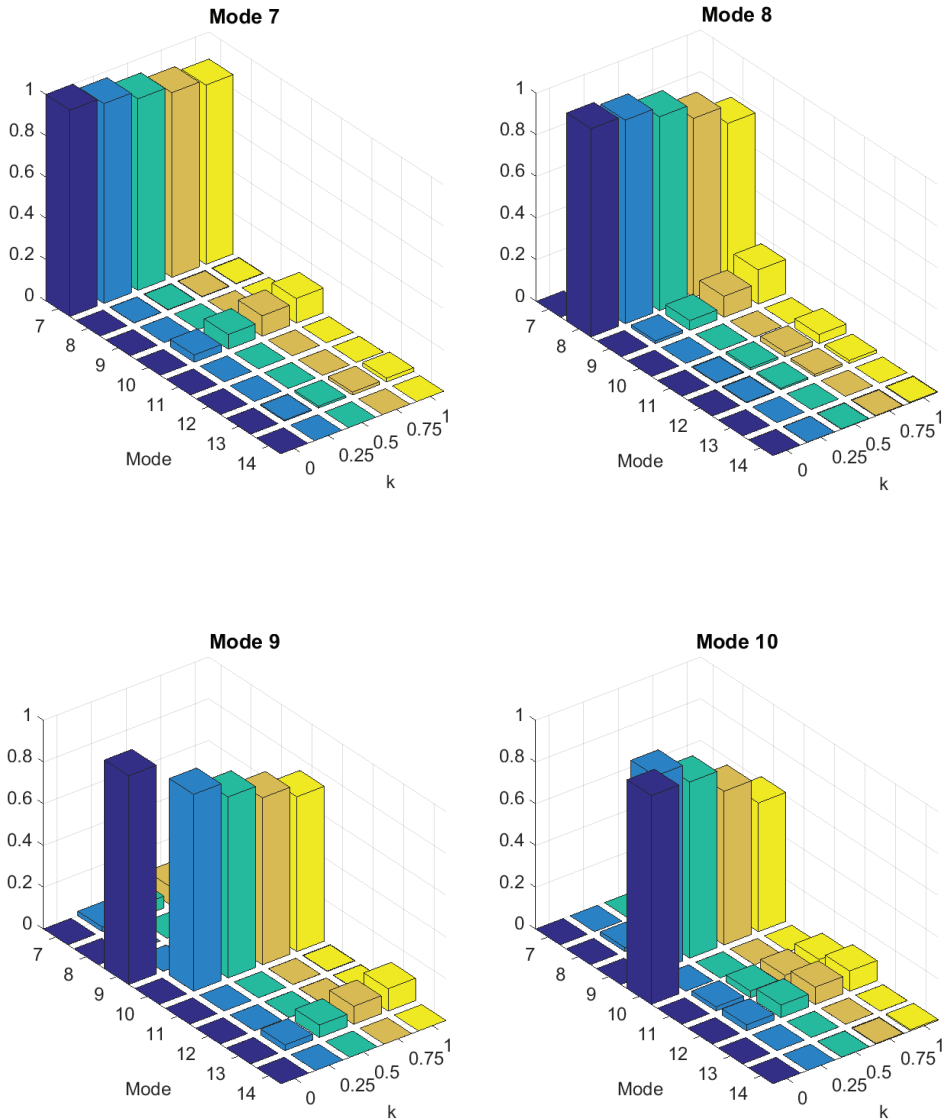
Figure 4.25: Hip implant natural vibration modes MAC comparison. Modes from 7 to 10.
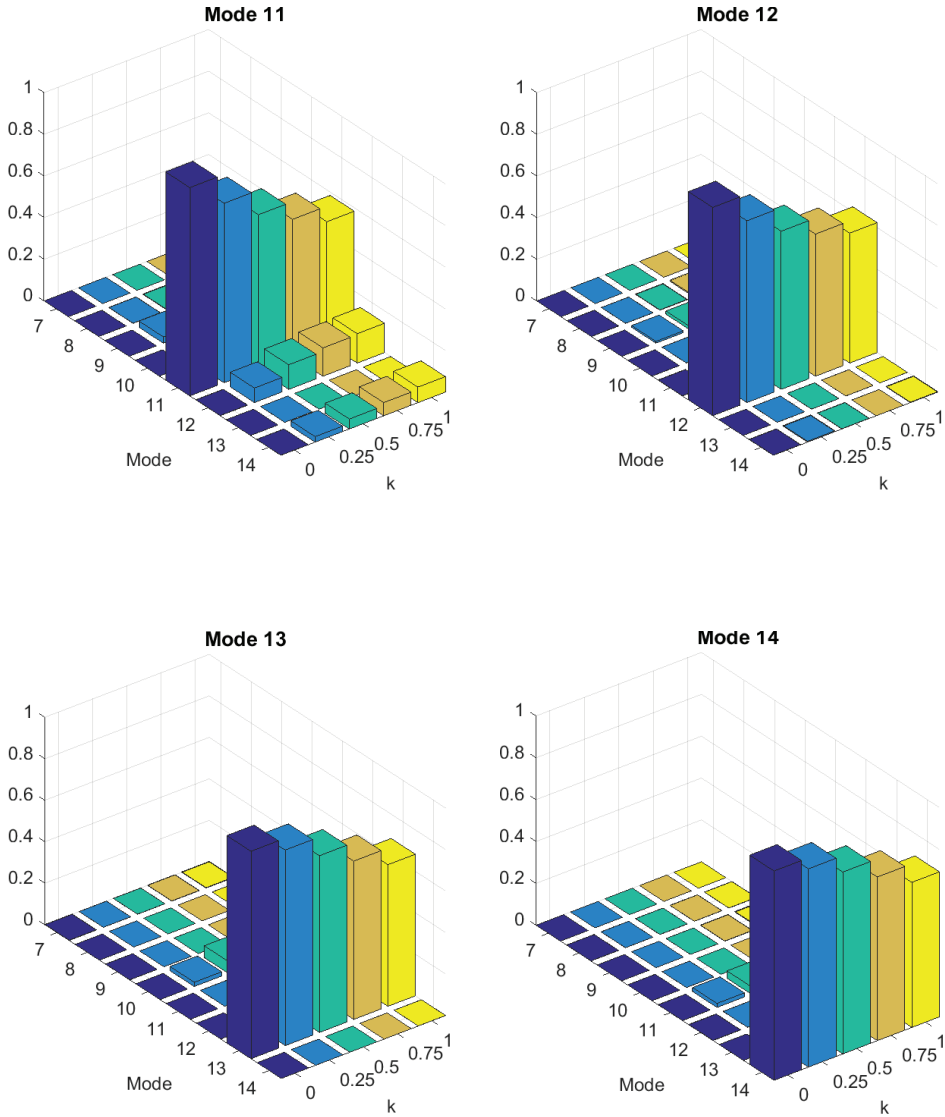
Figure 4.26: Hip implant natural vibration modes MAC comparison. Modes from 11 to 14.

The natural frequencies associated to the pair of the lowest bending modes increase

by 39% and 76%, respectively. In this femur model and for the considered range, the most sensitive modes are the 8th and the 12th, which increases by 57%.

The results obtained for hip model are similar to those calculated for the dental implant. In both cases the modes which show the highest relative change are the low frequency bending ones, which therefore would be suitable for an experimentation with clinical data analysis to properly define a bone quality indicator for a given kind of implant.

Chapter 5

Closure

The following subsections summarise the main contributions of this Thesis as well as the research lines opened.

5.1. Summary

In this Thesis we introduce an *image-based* version of *cg*FEM for solving linear elasticity problems on domains defined by 2D and 3D bitmaps and demonstrate its performance in a variety of cases. The key points of the new method can be summarized as follows:

- The use of Cartesian grids reduces the effort to model objects defined by 2D and 3D images keeping the number of degrees of freedom reasonable at the same time [101], [102], [103], [104], [105], [106]. An initial uniform grid is superimposed on the image and an *h*-adaptive process refines the mesh based on the level of heterogeneity of the pixels contained in each element. This makes it possible to

---

automatically take into account the interfaces, implicitly defined in the image, which are captured by the refinement process, as well as the information about the local elastic property provided by each pixel. This has been especially developed to deal with the structural analysis of heterogeneous solid materials, especially bone and bone-implant ensembles.

- We present and study the behaviour of different integration schemes based on direct pixel integration (Decomposition in integration subdomains and Riemann sum) and fitting to pixel values (Least squares) [107]. The convergence studies carried out highlight the range of usability of the mesh refinement, limited by the intrinsic presence of a modelling error due to the discrete nature of images. This cannot be reduced by h-refinement unlike discretisation error, therefore the theoretical convergence to the exact solution is guaranteed to a certain extent but it has a limit. Once the mesh refinement process produces a solution that reaches this limit, further mesh refinements increase the computational cost without increasing the result accuracy. From this point of view, *voxel-based* FE models are in this situation by default. This effect is analogous to the cases in which the error due to a poor geometrical description is higher than the error due to the FE discretisation [108].

  The Riemann sum based integration scheme showed to be a cheaper alternative to the subdomain decomposition scheme, as the integration error, which increases for finer meshes, starts to be relevant beyond the range of convenient application of mesh refinement.

  Finally the least squares integration strategy is a practical solution to reduce the computational cost necessary to obtain the element stiffness matrices and converges to the results of the other two techniques as the element size decreases.

  On the basis of the numerical results obtained, we propose to use the least square or Riemann sum integration strategies and linear elements containing 2 pixels in each direction at least.

- We propose the *cg*FEM virtual characterisation strategy: an homogenisation technique based on the use of Cartesian grids [109] to characterise heterogeneous materials represented in volumetric images. It was applied to 3D printed PLA close cell foams and partially validated with experimental results and empirical formulae. The proposed technique also includes an implementation of the

Window Method in the framework of *cg*FEM making it possible to reduce the RVE size required by the homogenisation technique at the cost of an iterative procedure. The window method is particularly compatible with *cg*FEM. On the one hand, this is due to the fact that the window creation is automatic as it is obtained by construction form the external element layer of the first uniform mesh, which is the starting point for meshing with *cg*FEM. On the other hand, one window element only requires to be integrated at each step of the process, thank to the fact that, similarly to the internal elements in geometrical *cg*FEM, the stiffness matrices of all the window elements are also proportional to each other.

- A methodology to take into account the anisotropy of the voxels affected by the Partial Volume Effect in the relation between voxel intensity and elastic properties. This is specific for models with a high number of interfaces and not pre-segmented as those used for solid foams characterisation with *cg*FEM, in which the elements are not conforming with any geometric boundary.

  The definition of the relation between voxel value and elastic properties also takes advantage of an inexpensive procedure which includes the specimen weighing and the image histogram processing.

- The proposed procedure produces results which match well with the experimental ones, in contrast to the latter, can provide a complete description of the anisotropic behaviour of the material in the linear elastic range and, in comparison, are much cheaper as they require a smaller amount of human intervention.

- Two Alternative procedures were proposed to include implants in patient specific simulations reducing the user intervention [101], [110], [111], [112].

  The first one consists in the direct inclusion of both the patient CT scan and the prosthesis CAD model in the same hierarchical Cartesian grid structure. The element stiffness matrices are obtained by combining the geometrical and image-based versions of *cg*FEM. The elements totally overlapped to the CAD have proportional stiffness matrices, therefore their calculation is inexpensive. The elements overlapped to both the CAD and the volumetric image undergo a mixed integration including both the decomposition in tetrahedra of the geometrical part and the voxel integration. The heterogeneity-based mesh refinement

makes it possible to conveniently adapt the model reducing the size of the mixed integration elements.

The second approach consists in the voxelisation of the CAD model by using commercial software capable of providing Cartesian meshes of geometrical models, such as GiD. The Cartesian mesh is created in order to be compatible to the volumetric image and directly included. This second solution is less accurate than the first one, as it reduces the quality of the implant definition introducing the same model error affecting the discontinuous volumetric image. Nevertheless, it simplifies the process reducing it to a standard *image-based cg*FEM calculation. This solution will have a sufficient accuracy in certain kinds of evaluations such as the implant stability assessment.

- A new indicator for the preoperative assessment of bone quality has been proposed [113]. This is based on the analysis of the natural frequencies of the device alone and implanted, computed by *cg*FEM and CT scans. The homologous modes can be matched by using the well known Mode Assurance Criterion (MAC). We consider that the influence on the implants natural frequencies due to the bone characteristics could be used as an indicator to evaluate implant stability.

5.2. Open research lines

This work has opened up several lines of research on *cg*FEM technology as follows:

- **Development of an error-driven mesh refinement strategy**.
  Taking advantage of the wide experience in error estimation of the research group involved in the development of this Thesis, a logical development would be the implementation of *a posteriori* error estimators suitable for image-based problems and the evaluation of their performance. These would make it possible to introduce better criteria for the mesh refinement, as material heterogeneity is only one of the possible sources of error. The first choice would be the use of

Zenkiewicz-Zhu estimators [114], due to their low computational cost and high effectiveness. There are different possible alternative strategies. For instance, in contrast to standard FEM problems, in *image-based cg*FEM, the ZZ error estimator is expected to behave quite differently depending if the recovered solution is obtained form the strain or the stress field due to the different influence of the intrinsic modelling error due to the bitmap piece wise continuity. Additional restraints [115] could also show unexpected behaviours, in the case of bitamp-based models. Once a suitable error estimation method is developed, it will make it possible to apply more sophisticated mesh strategies such as goal oriented error estimation [116]. The presence of homoscedastic distributions (i.e. with a constant standard deviation of the error terms of the fitted model) of bone elastic properties in bi-logarithmic scale for human femur [44] could also make it possible to optimise the mesh trying to minimise the error in the obtention of the probability density function (PDF) in the FE results.

- **Improvement and validation of the homogenisation technique**.
  On the one hand, in spite of the promising results obtained, it is necessary to carry out a high number of additional mechanical tests for the assessment of the directional values of the Young's modulus by uniaxial compression, due to the great dispersion found in the experimental measurements carried out so far on printed PLA foams. The natural development would be the study of the effect of the printing direction to evaluate the influence of the hypothesis of local isotropic elasticity of the basis material. Mechanical tests on solid specimens printed in different direction would help understanding the convenience of implementing a locally orthotropic material model. As an alternative to the Partial Volume Correction Function, a method based on the evaluation of the local gradient of the pixel value field could be used together with a proper orthotropic material model. It will be necessary to assess the performance of the method with additional foam specimens, with different structures, density values and materials. It would be also beneficial to improve the voxel clustering for the definition of the density-pixel intensity relation, in the case of μCT scans of solid foams. For this purpose automatic procedures based, for instance, on Gaussian mixture models [117], [83] could be used. This would make it possible to reduce the user intervention in the numerical homogenisation process.

- **Validation of the natural bone quality biomarker**.
  An extensive experimentation with large sets of preoperative CT-scans would be necessary to validate and make usable the natural frequency-based bone quality indicator. The information about the implantable device survival related to the database should be accessible in order to be able to properly define the most suitable frequencies to use as biomarkers and their thresholds. The experimentation would have to take into account the device and anatomical site specificity as well as the variability due to the volumetric image capture method and would be a retrospective clinical study on patient data stored by health care centres.

- **Implant-bone contact simulations**.
  Another development from results obtained in this thesis, is the use of advanced contact models [118], [119], to simulate the interaction between the a CAD-based device model and an image-based patient-specific one with independent cgFEM meshes. This is a research line currently in progress in the framework of another thesis in the same research group, which will make it possible to study the implant behaviour in the very first postoperative stages, when osteointegration has not occurred yet. In some cases, as for immediate-load dental device, this information is particularly valuable.

- **Bone remodelling**.
  The image-based version of cgFEM can be a good starting point for the implementation of bone remodelling procedures capable of forecasting the change in bone density over time due to the local stress state. Such models can be used for the optimisation of implants to avoid their long term failure due, for instance, to bone resorption.

Bibliography

[1] Grassi L, Schileo E, Taddei F, Zani L, Juszczyk M, Cristofolini L. Accuracy of finite element predictions in sideways load configurations for the proximal human femur. *Journal of biomechanics* 2012; **45**(2):394–399. 1

[2] Christen D, Melton III L, Zwahlen A, Amin S, Khosla S, Müller R. Improved fracture risk assessment based on nonlinear micro-finite element simulations from hrpqct images at the distal radius. *Journal of Bone and Mineral Research* 2013; **28**(12):2601–2608, doi:10.1002/jbmr.1996. 1

[3] Viceconti M, Qasim M, Bhattacharya P, Li X. Are ct-based finite element model predictions of femoral bone strengthening clinically useful? *Current Osteoporosis Reports* Jun 2018; **16**(3):216–223, doi:10.1007/s11914-018-0438-8. 1

[4] Hosseini HS, Dünki A, Fabech J, Stauber M, Vilayphiou N, Pahr D, Pretterklieber M, Wandel J, van Rietbergen B, Zysset PK. Fast estimation of colles' fracture load of the distal section of the radius by homogenized finite element analysis based on hr-pqct. *Bone* 2017; **97**:65 – 75, doi:https://doi.org/10.1016/j.bone.2017.01.003. URL http://www.sciencedirect.com/science/article/pii/S8756328217300030. 1

[5] Alberich-Bayarri A, Marti-Bonmati L, Sanz-Requena R, Belloch E, Moratal D. In vivo trabecular bone morphologic and mechanical relationship using high-

resolution 3-T MRI. *AJR. American journal of roentgenology* 2008; **191**(3):721–6, doi:10.2214/AJR.07.3528. 1, 1

[6] Roque WL, Arcaro K, Alberich-Bayarri A. Tortuosity and elasticity study of distal radius trabecular bone. *Iberian Conference on Information Systems and Technologies, CISTI*, 2012. 1

[7] Bah MT, Browne M, Young PG, Bryan R, Xuan VB. Effects of implant positioning in cementless total hip replacements. *Computer Methods in Biomechanics and Biomedical Engineering* 2011; **14**(sup1):275–276. 1

[8] Pérez M, Vendittoli PA, Lavigne M, Nuño N. Bone remodeling in the resurfaced femoral head: Effect of cement mantle thickness and interface characteristics. *Medical Engineering & Physics* 2014; **36**(2):185 – 195. 1

[9] Cheong VS, Fromme P, Mumith A, Coathup MJ, Blunn GW. Novel adaptive finite element algorithms to predict bone ingrowth in additive manufactured porous implants. *Journal of the Mechanical Behavior of Biomedical Materials* 2018; **87**:230 – 239, doi:https://doi.org/10.1016/j.jmbbm.2018.07.019. URL http://www.sciencedirect.com/science/article/pii/S1751616118307422. 1

[10] Levadnyi I, Awrejcewicz J, Gubaua JE, Pereira JT. Numerical evaluation of bone remodelling and adaptation considering different hip prosthesis designs. *Clinical Biomechanics* 2017; **50**:122 – 129, doi:https://doi.org/10.1016/j.clinbiomech.2017.10.015. URL http://www.sciencedirect.com/science/article/pii/S0268003317302681. 1

[11] Sutradhar A, Park J, Carrau D, Nguyen TH, Miller MJ, Paulino GH. Designing patient-specific 3d printed craniofacial implants using a novel topology optimization method. *Medical & Biological Engineering & Computing* 2016; **54**(7):1123–1135. 1

[12] Dharme M, Kuthe A. Effect of geometric parameters in the design of customized hip implants. *Journal of Medical Engineering and Technology* 2017; **41**(6):429–436, doi:10.1080/03091902.2017.1323967. 1

[13] Bishop J. Rapid stress analysis of geometrically complex domains using implicit meshing. *Computational Mechanics* Apr 2003; **30**(5):460–478, doi:10.1007/s00466-003-0424-5. URL https://doi.org/10.1007/s00466-003-0424-5. 1

[14] Cottrell JA, Hughes TJR, Bazilevs Y. *Isogeometric Analysis: Toward Integration of CAD and FEA*. Wiley, 2009. 1

[15] Bordas SPA, Rabczuk T, Rodenas JJ, Kerfriden P, Moumnassi M, Belouettar S. Recent Advances Towards Reducing the Meshing and Re-Meshing Burden in Computational Sciences. *Computational Technology Reviews* 2010; **2**:51–82. 1

[16] Burman E, Hansbo P. Fictitious domain finite element methods using cut elements: I. a stabilized lagrange multiplier method. *Computer Methods in Applied Mechanics and Engineering* 2010; **199**(41–44):2680 – 2686, doi:http://dx.doi.org/10.1016/j.cma.2010.05.011. 1

[17] Dolbow J, Harari I. An efficient finite element method for embedded interface problems. *International Journal for Numerical Methods in Engineering* 4 2009; **78**(2):229–252, doi:10.1002/nme.2486. 1

[18] Cottrell JA, Hughes TJR, Bazilevs Y. *Isogeometric Analysis: Toward Integration of CAD and FEA*. 1st edn., Wiley, 2009. 1

[19] Marco O, Sevilla R, Zhang Y, Ródenas JJ, Tur M. Exact 3d boundary representation in finite element analysis based on cartesian grids independent of the geometry. *International Journal for Numerical Methods in Engineering* 2015; **103**:445–468. 1

[20] Marco O, Ródenas JJ, Navarro-Jiménez JM, Tur M. Robust h-adaptive meshing strategy for arbitrary cad geometries in a cartesian grid framework. *Computers & Structures* 2017; **Submitted**. 1

[21] Panyasantisuk J, Dall'Ara E, Pretterklieber M, Pahr D, Zysset P. Mapping anisotropy improves qct-based finite element estimation of hip strength in pooled stance and side-fall load configurations. *Medical Engineering & Physics* 2018; **59**:36 – 42, doi:https://doi.org/10.1016/j.medengphy.2018.06.004. 1

[22] Zaharie D, Phillips A. Pelvic construct prediction of trabecular and cortical bone structural architecture. *Journal of Biomechanical Engineering* 2018; **140**(9), doi:10.1115/1.4039894. 1

[23] Marco M, Giner E, Larraínzar-Garijo R, Caeiro JR, Miguélez MH. Modelling of femur fracture using finite element procedures. *Engineering Fracture Mechanics* 2018; **196**:157 – 167, doi:https://doi.org/10.1016/j.engfracmech.2018.04.024. 1

[24] Natali AN, Pavan PG, Ruggero AL. Evaluation of stress induced in peri-implant bone tissue by misfit in multi-implant prosthesis. *Dental materials : official publication of the Academy of Dental Materials* 2006; **22**(4):388–95, doi:10.1016/j.dental.2005.08.001. 1

[25] Müller-Karger CM, Rank E, Cerrolaza M. P-Version of the Finite-Element Method for Highly Heterogeneous Simulation of Human Bone. *Finite Elements in Analysis and Design* 2004; **40**(7):757–770, doi:10.1016/S0168-874X(03)00113-6. 1

[26] Legrain G, Cartraud P, Perreard I, Moës N. An x-fem and level set computational approach for image-based modelling: Application to homogenization. *International Journal for Numerical Methods in Engineering* 2011; **86**(7):915–934, doi:10.1002/nme.3085. 1

[27] Lian WD, Legrain G, Cartraud P. Image-based computational homogenization and localization: comparison between x-fem/levelset and voxel-based approaches", journal="computational mechanics 2013; **51**(3):279–293. 1

[28] Liehr F, Preusser T, Rumpf M, Sauter S, Schwen LO. Composite finite elements for 3D image based computing. *Computing and Visualization in Science* 2009; **12**(4):171–188. 1

[29] Ruess M, Tal D, Trabelsi N, Yosibash Z, Rank E. The finite cell method for bone simulations: verification and validation. *Biomechanics and modeling in mechanobiology* 2012; **11**(3-4):425–37, doi:10.1007/s10237-011-0322-2. 1

[30] Dauge M, Düster A, Rank E. Theoretical and numerical investigation of the finite cell method. *Journal of Scientific Computing* 2015; **65**(3):1039–1064, doi:10.1007/s10915-015-9997-3. 1

[31] Verhoosel C, van Zwieten G, van Rietbergen B, de Borst R. Image-based goal-oriented adaptive isogeometric analysis with application to the micromechanical modeling of trabecular bone. *Computer Methods in Applied Mechanics and Engineering* 2015; **284**:138 – 164. 1

[32] Nadal E. Cartesian grid fem (cgfem): High performance h-adaptive fe analysis with efficient error control. application to structural shape optimization. PhD Thesis, Dir. F. J. Fuenmayor, J. J. Ródenas, Universidad Politécnica de Valencia 2014. 1, 2.1, 2.4.3

[33] Ródenas J, Albelda J, Tur M, Fuenmayor F. A hierarchical h adaptivity methodology based on element subdivision. *UIS Ingenierías* 2017; **16**(2):263 – 280, doi:https://doi.org/10.18273/revuin.v16n2-2017024. 2.1

[34] Zenk O, Sevilla R, Zhang Y, Ródenas JJ, Tur M. Exact 3d boundary representation in finite element analysis based on cartesian grids independent of the geometry. *International Journal for Numerical Methods in Engineering* 2015; **103**(6):445–468, doi:10.1002/nme.4914. 2.1, 4.2.1.3

[35] Zienkiewicz OC, Zhu JZ. A simple error estimator and adaptive procedure for practical engineering analysis. *International Journal for Numerical Methods in Engineering* 1987; **24**(2):337–357. 2.1

[36] Fuenmayor FJ, Oliver JL, Ródenas JJ. Extension of the Zienkiewicz-Zhu error estimator to shape sensitivity analysis. *International Journal for Numerical Methods in Engineering* 1997; **40**(8):1413–1433. 2.1

[37] Nadal E, Ródenas J. Fundaments of recovery-based error estimation and bounding. *SpringerBriefs in Applied Sciences and Technology* 2016; **172**:33–57, doi:10.1007/978-3-319-20553-3_3. 2.1

[38] Nadal E, Díez P, Ródenas J, Tur M, Fuenmayor F. A recovery-explicit error estimator in energy norm for linear elasticity. *Computer Methods in Applied Mechanics and Engineering* 2015; **287**:172 – 190, doi:http://dx.doi.org/10.1016/j.cma.2015.01.013. 2.1

[39] Tur M, Albelda J, Nadal E, Ródenas J. Imposing dirichlet boundary conditions in hierarchical cartesian meshes by means of stabilized lagrange multipliers.

International Journal for Numerical Methods in Engineering 2014; **98**(6):399–417, doi:10.1002/nme.4629. 2.1

[40] Tur M, Albelda J, Zenk O, Ródenas J. Stabilized method of imposing dirichlet boundary conditions using a recovered stress field. *Computer Methods in Applied Mechanics and Engineering* 2015; **296**:352–375, doi:http://dx.doi.org/10.1016/j.cma.2015.08.001. 2.1

[41] Yang Z, Ruess M, Kollmannsberger S, Düster A, Rank E. An efficient integration technique for the voxel-based finite cell method. *International Journal for Numerical Methods in Engineering* 2012; **91**(June):457–471, doi:10.1002/nme. 2.2.1

[42] Nadal E, Ródenas JJ, Albelda J, Tur M, Tarancón JE, Fuenmayor FJ. Efficient finite element methodology based on cartesian grids: Application to structural shape optimization. *Abstract and Applied Analysis* 2013; . 2.2.1, 2.7

[43] Zannoni C, Mantovani R, Viceconti M. Material properties assignment to finite element models of bone structures: a new method. *Medical engineering & physics* 1998; **20**(10):735–40. 2.2.2

[44] Wille H, Rank E, Yosibash Z. Prediction of the mechanical response of the femur with uncertain elastic properties. *Journal of Biomechanics* 2012; **45**(7):1140–1148, doi:10.1016/j.jbiomech.2012.02.006. 2.2.2, 5.2

[45] Helgason B, Perilli E, Schileo E, Taddei F, Brynjólfsson S, Viceconti M. Mathematical relationships between bone density and mechanical properties: A literature review. *Clinical Biomechanics* 2008; **23**(2):135 – 146, doi:https://doi.org/10.1016/j.clinbiomech.2007.08.024. 2.2.2

[46] Morgan EF, Bayraktar HH, Keaveny TM. Trabecular bone modulus–density relationships depend on anatomic site. *Journal of Biomechanics* 2003; **36**(7):897 – 904, doi:https://doi.org/10.1016/S0021-9290(03)00071-X. 2.2.2

[47] Ruess M, Varduhn V, Rank E, Yosibash Z. A Parallel High-Order Fictitious Domain Approach for Biomechanical Applications. *2012 11th International Symposium on Parallel and Distributed Computing* 2012; :279–285. 2.3

[48] Guldberg RE, Hollister SJ, Charras GT. The accuracy of digital image-based finite element models. *Journal of Biomechanical Engineering* 1998; **120**, doi:10.1115/1.2798314. 2.3.1.1

[49] Hollister SJ, Riemer BA. Digital-image-based finite element analysis for bone microstructure using conjugate gradient and gaussian filter techniques. *Proc.SPIE* 1993; **2035**:2035 – 2035 – 12, doi:10.1117/12.146616. 2.3.1.1

[50] Viceconti M, Bellingeri L, Cristofolini L, Toni A. A comparative study on different methods of automatic mesh generation of human femurs. *Medical engineering & physics* 1998; **20**(1):1–10. 2.4.2, 4.2.1.1

[51] Kim H, Jürgens P, Weber S, Nolte LP, Reyes M. A new soft-tissue simulation strategy for cranio-maxillofacial surgery using facial muscle template model. *Progress in biophysics and molecular biology* 2010; **103**(2-3):284–91, doi:10.1016/j.pbiomolbio.2010.09.004. 2.4.2, 4.2.1.1

[52] Reeves T, Mah P, McDavid W. Deriving hounsfield units using grey levels in cone beam ct: a clinical application. *Dentomaxillofacial Radiology* 2012; **41**(6):500–508. 2.4.3

[53] Marco O. Structural shape optimization based on the use of cartesian grids. PhD Thesis, Dir. J. J. Ródenas, M. Tur, Universitat Politècnica de València 2017. 2.4.3

[54] Kolken H, Janbaz S, Leeflang S, Lietaert K, Weinans H, Zadpoor A. Rationally designed meta-implants: A combination of auxetic and conventional meta-biomaterials. *Materials Horizons* 2018; **5**(1):28–35, doi:10.1039/c7mh00699c. 3.1

[55] Zadpoor A. Design for additive bio-manufacturing: From patient-specific medical devices to rationally designed meta-biomaterials. *International Journal of Molecular Sciences* 2017; **18**(8), doi:10.3390/ijms18081607. 3.1

[56] Schwen L, Pätz T, Preusser T. *Some use cases for composite finite elements in image based computing.* 2016, doi:10.1007/978-3-319-28329-6_11. 3.1

[57] Kowalczyk P. Orthotropic properties of cancellous bone modelled as parameterized cellular material. *Computer Methods in Biomechanics and Biomedical Engineering* 2006; **9**(3):135–147, doi:10.1080/10255840600751473. 3.1

[58] Bienvenu Y. Application and future of solid foams. *Comptes Rendus Physique* 2014; **15**(8):719 – 730, doi:https://doi.org/10.1016/j.crhy.2014.09.006. URL http://www.sciencedirect.com/science/article/pii/S1631070514001339, liquid and solid foams / Mousses liquides et solides. 3.1

[59] Chen WM, Xie YM, Imbalzano G, Shen J, Xu S, Lee SJ, Lee PVS. Lattice ti structures with low rigidity but compatible mechanical strength: Design of implant materials for trabecular bone. *International Journal of Precision Engineering and Manufacturing* Jun 2016; **17**(6):793–799, doi:10.1007/s12541-016-0097-6. URL https://doi.org/10.1007/s12541-016-0097-6. 3.1

[60] Arabnejad S, Johnston B, Tanzer M, Pasini D. Fully porous 3d printed titanium femoral stem to reduce stress-shielding following total hip arthroplasty. *Journal of Orthopaedic Research* 2017; **35**(8):1774–1783, doi:10.1002/jor.23445. 3.1

[61] Sumner D, Turner T, Igloria R, Urban R, Galante J. Functional adaptation and ingrowth of bone vary as a function of hip implant stiffness. *Journal of Biomechanics* 1998; **31**(10):909–917, doi:10.1016/S0021-9290(98)00096-7. 3.1

[62] Liu J, Zhou X, Wang H, Yang H, Ruan J. In vitro cell response and in vivo primary osteointegration of highly porous ta-nb alloys as implant materials. *Journal of Biomedical Materials Research - Part B Applied Biomaterials* 2018; doi:10.1002/jbm.b.34149. 3.1

[63] Zhang L, He Z, Tan J, Calin M, Prashanth K, Sarac B, Völker B, Jiang Y, Zhou R, Eckert J. Designing a multifunctional ti-2cu-4ca porous biomaterial with favorable mechanical properties and high bioactivity. *Journal of Alloys and Compounds* 2017; **727**:338–345, doi:10.1016/j.jallcom.2017.08.145. 3.1

[64] Sornay-Rendu E, Boutroy S, Duboeuf F, Chapurlat R. Bone microarchitecture assessed by hr-pqct as predictor of fracture risk in postmenopausal women: The ofely study. *Journal of Bone and Mineral Research* 2017; **32**(6):1243–1251, doi:10.1002/jbmr.3105. 3.1

[65] Boutroy S, Bouxsein M, Munoz F, Delmas P. In vivo assessment of trabecular bone microarchitecture by high-resolution peripheral quantitative computed tomography. *Journal of Clinical Endocrinology and Metabolism* 2005; **90**(12):6508–6515, doi:10.1210/jc.2005-1258. 3.1

[66] Xie F, Zhou B, Wang J, Liu T, Wu X, Fang R, Kang Y, Dai R. Microstructural properties of trabecular bone autografts: comparison of men and women with and without osteoporosis. *Archives of Osteoporosis* Mar 2018; **13**(1):18, doi:10.1007/s11657-018-0422-z. 3.1

[67] Hohe J, Becker W. Effective mechanical behavior of hyperelastic honeycombs and two-dimensional model foams at finite strain. *International Journal of Mechanical Sciences* 2003; **45**(5):891 – 913, doi:https://doi.org/10.1016/S0020-7403(03)00114-0. URL http://www.sciencedirect.com/science/article/pii/S0020740303001140. 3.1

[68] Düster A, Sehlhorst HG, Rank E. Numerical homogenization of heterogeneous and cellular materials utilizing the finite cell method. *Computational Mechanics* 2012; **50**(4):413–431, doi:10.1007/s00466-012-0681-2. 3.1, 3.3

[69] Sun C, Vaidya R. Prediction of composite properties from a representative volume element. *Composites Science and Technology* 1996; **56**(2):171–179, doi:10.1016/0266-3538(95)00141-7. 3.1

[70] Xia Z, Zhang Y, Ellyin F. A unified periodical boundary conditions for representative volume elements of composites and applications. *International Journal of Solids and Structures* 2003; **40**(8):1907–1921, doi:10.1016/S0020-7683(03)00024-6. 3.1

[71] Segurado J, Llorca J. A numerical approximation to the elastic properties of sphere-reinforced composites. *Journal of the Mechanics and Physics of Solids* 2002; **50**(10):2107–2121, doi:10.1016/S0022-5096(02)00021-2. 3.1

[72] Hain M, Wriggers P. Numerical homogenization of hardened cement paste. *Computational Mechanics* Jul 2008; **42**(2):197–212, doi:10.1007/s00466-007-0211-9. URL https://doi.org/10.1007/s00466-007-0211-9. 3.1, 3.3

[73] Hill R. The Elastic Behaviour of a Crystalline Aggregate. *Proceedings of the Physical Society. Section A* 1952; **65**(5):349–354, doi:10.1088/0370-1298/65/5/307. URL http://stacks.iop.org/0370-1298/65/i=5/a=307?key=crossref.630b67f122246b4defcc5fda55c7bf20. 3.2

[74] Zohdi T, Wriggers P. An introduction to computational micromechanics. *Lecture Notes in Applied and Computational Mechanics* 2005; **20**:1–195. URL https://www.scopus.com/inward/record.uri?eid=2-s2.0-84858397692&partnerID=40&md5=4070925abffa334d8c71c46c44ef39ed, cited By 92. 3.2

[75] Daszkiewicz K, Maquer G, Zysset PK. The effective elastic properties of human trabecular bone may be approximated using micro-finite element analyses of embedded volume elements. *Biomechanics and Modeling in Mechanobiology* 2017; **16**(3):731–742, doi:10.1007/s10237-016-0849-3. URL https://doi.org/10.1007/s10237-016-0849-3. 3.3

[76] Temizer I, Wu T, Wriggers P. On the optimality of the window method in computational homogenization. *International Journal of Engineering Science* 2013; **64**:66 – 73, doi:https://doi.org/10.1016/j.ijengsci.2012.12.007. URL http://www.sciencedirect.com/science/article/pii/S0020722513000049. 3.3

[77] Fedorov A, Beichel R, Kalpathy-Cramer J, Finet J, Fillion-Robin JC, Pujol S, Bauer C, Jennings D, Fennessy F, Sonka M, *et al.*. 3d slicer as an image computing platform for the quantitative imaging network. *Magnetic Resonance Imaging* 2012; **30**(9):1323–1341, doi:10.1016/j.mri.2012.05.001. 3.4

[78] The Mathworks, Inc., Natick, Massachusetts. *MATLAB version 8.5.0.197613 (R2015a)* 2015. 3.4

[79] MEDICAL S. www.scanco.ch 2011. URL http://www.scanco.ch/en/docs/images/microct80.html, [Online; accessed Sep-2018]. 3.4

[80] Stręk AM. Methodology for experimental investigations of metal foams and their mechanical properties. *Mechanics and Control* 2012; **Vol. 31, no. 2**:90–96. 3.4.2

[81] Soret M, Bacharach S, Buvat I. Partial-volume effect in pet tumor imaging. *Journal of Nuclear Medicine* 2007; **48**(6):932–945. 3.5

[82] Goodenough D, Weaver K, Davis D, LaFalce S. Volume averaging limitations of computed tomography. *American Journal of Roentgenology* 1982; **138**(2):313–316. 3.5

[83] Bazi Y, Bruzzone L, Melgani F. Image thresholding based on the em algorithm and the generalized gaussian distribution. *Pattern Recognition* 2007; **40**(2):619–634. 3.5, 5.2

[84] Xiberta P, Bardera A, Boada I, Gispert M, Brun A, Font-i Furnols M. Evaluation of an automatic lean meat percentage quantification method based on a partial volume model from computed tomography scans. *Computers and Electronics in Agriculture* 2018; **151**:365–375. 3.5

[85] Kato M, Takahashi M, Kawasaki S, Kaneko K. Segmentation of multi-phase x-ray computed tomography images. *Environmental Geotechnics* 2015; **2**(2):104–117. 3.5

[86] Ruan S, Jaggi C, Xue J, Fadili J, Bloyet D. Brain tissue classification of magnetic resonance images using partial volume modeling. *IEEE Transactions on Medical Imaging* 2000; **19**(12):1179–1187. 3.5

[87] Torres J, Cotelo J, Karl J, Gordon AP. Mechanical property optimization of fdm pla in shear with multiple objectives. *JOM* May 2015; **67**(5):1183–1193, doi:10.1007/s11837-015-1367-y. URL https://doi.org/10.1007/s11837-015-1367-y. 3.6

[88] Gibson LJ, Ashby MF. *Cellular Solids: Structure and Properties*. 2 edn., Cambridge Solid State Science Series, Cambridge University Press, 1997, doi:10.1017/CBO9781139878326. 3.8

[89] Roberts A, Garboczi E. Elastic moduli of model random three-dimensional closed-cell cellular solids. *Acta Materialia* 2001; **49**(2):189 – 197, doi:10.1016/S1359-6454(00)00314-1. 3.8

[90] Yang M, Sun G, Guo S, Zeng C, Yan M, Han Y, Xia D, Zhang J, Li X, Xiang Y, *et al.*. The biomechanical study of extraforaminal lumbar interbody fusion: A three-dimensional finite-element analysis. *Journal of Healthcare Engineering* sep 2017; **2017**:9365 068, doi:10.1155/2017/9365068. URL http://www.ncbi.nlm.nih.gov/pmc/articles/PMC5634568/. 4.1

[91] Young P, Coward S, Tabor G, Kennedy J, Chen B, Harkara A. Computational modeling for cad data integration into 3d image data. 2009; 287–288, doi:10.1007/978-3-642-01697-4_100. 4.1

[92] Dopico-González C, New AM, Browne M. Probabilistic analysis of an uncemented total hip replacement. *Medical Engineering & Physics* 2009; **31**(4):470–476, doi:https://doi.org/10.1016/j.medengphy.2009.01.002. URL `http://www.sciencedirect.com/science/article/pii/S1350453309000368`, finite Element Modelling of Medical Devices. 4.1

[93] Gelaude F, Sloten JV, Lauwers B. Accuracy assessment of ct-based outer surface femur meshes. *Computer Aided Surgery* 2008; **13**(4):188–199, doi:10.3109/10929080802195783. 4.1

[94] Coll A, Ribó R, Pasenau M, Escolano E, Perez J, Melendo A, Monros A, Gárate J. *GiD v.13 User Manual* 2016. 4.3

[95] Coll A, Ribó R, Pasenau M, Escolano E, Perez J, Melendo A, Monros A, Gárate J. *GiD v.13 Reference Manual* 2016. 4.3

[96] Coll A, Ribó R, Pasenau M, Escolano E, Perez J, Melendo A, Monros A, Gárate J. *GiD v.13 Customization Manual* 2016. 4.3

[97] Rondon A. Characterization of the bone-implant interface and numerical analysis of implant vibrational behavior for a mechanics based preoperative planning of total hip arthroplasty. PhD Thesis, Dir. Q. Grimal, Université Pierre et Marie Curie - Paris VI 2017. 4.3.1

[98] Asma F, Kacel S. Finite element and isogeometric correlation analysis using modal assurance criterion. *Mechanika* 2017; **23**(1):132–137, doi:10.5755/j01.mech.23.1.13890. 4.3.1

[99] Brigante D, Rainieri C, Fabbrocino G. The role of the modal assurance criterion in the interpretation and validation of models for seismic analysis of architectural complexes. 2017; 3404–3409, doi:10.1016/j.proeng.2017.09.484. 4.3.1

[100] Allemang RJ. The modal assurance criterion - Twenty years of use and abuse. *Sound and Vibration* 2003; **37**(8):14–21, doi:10.1016/j.chemgeo.2006.02.014.

URL   http://www.scopus.com/inward/record.url?eid=2-s2.
0-0141958862{&}partnerID=tZOtx3y1. 4.3.1

[101] Giovannelli L, Ródenas J, Navarro-Jiménez J, Tur M. Direct medical
image-based finite element modelling for patient-specific simulation of fu-
ture implants. *Finite Elements in Analysis and Design* 2017; **136**:37–57,
doi:10.1016/j.finel.2017.07.010. 5.1

[102] Giovannelli L, Marco O, Navarro J, Giner E, Ródenas J. Direct creation of fi-
nite element models from medical images using cartesian grids. *Computational
Vision and Medical Image Processing IV - Proceedings of Eccomas Thematic
Conference on Computational Vision and Medical Image Processing, VIPIM-
AGE 2013*, 2014; 167–172. 5.1

[103] Giovannelli L, Nadal E, Tur M, Albelda-Vitoria J, Ródenas J. Automatic mesh
refinement of objects defined by images. mesh efficiency study. *19th Interna-
tional Conference on Finite Elements in Flow Problems (FEF 2017)*, 2017. 5.1

[104] Giovannelli L, Ródenas J, Nadal E, Albelda-Vitoria J, Tur M. Automatic
patient-specific numerical simulations with the cartesian grid finite element
method and image data recovery. *12th World Congress on Computational Me-
chanics (WCCM 2016)*, 2017. 5.1

[105] Giovannelli L, Ródenas J, Navarro-Jiménez J, Tur M. Automatically adapted
finite element models from medical images. *12th International Symposium on
Computer Methods in Biomechanics and Biomedical Engineering (CMMBE
2014)*, 2014. 5.1

[106] Giovannelli L, Navarro-Jiménez J, Marco O, Nadal E, Tur M, Ródenas J. Au-
tomatically adapted finite element models from medical images. *11th World
Congress on Computational Mechanics (WCCM 2014)*, 2014. 5.1

[107] Giovannelli L, Ródenas J, Navarro-Jiménez J, Tur M. Element stiffness matrix
integration in image-based cartesian grid finite element method. *Lecture Notes
in Computer Science (including subseries Lecture Notes in Artificial Intelligence
and Lecture Notes in Bioinformatics)* 2014; **8641 LNCS**:304–315. 5.1

[108] Dey S, Shephard M, Flaherty J. Geometry representation issues associated with p-version finite element computations. *Computer Methods in Applied Mechanics and Engineering* 1997; **150**(1-4):39–55. 5.1

[109] Giovannelli L, Cárcel A, Cárcel B, Ródenas J. Automatic elastic characterization of aluminium foams by using h-adapted meshes with cartesian grid finite element method. *7th European Congress on Computational Methods in Applied Sciences and Engineering (ECCOMAS 2016)*, 2016. 5.1

[110] Ródenas J, Giovannelli L, Nadal E, Navarro J, Tur M. Creation of patient specific finite element models of bone-prosthesis—simulation of the effect of future implants. *Computational Vision and Medical Image Processing IV - Proceedings of Eccomas Thematic Conference on Computational Vision and Medical Image Processing, VIPIMAGE 2013*, 2014; 161–166. 5.1

[111] Marco O, Giovannelli L, Fuenmayor-Fernández F, Ródenas J, Tur M. Generación automática de mallas cartesianas 3d geométricamente h-adaptadas considerando representación exacta de la geometría. *Congreso de Métodos Numéricos en Ingeniería (CMN 2015)*, 2015. 5.1

[112] Giovannelli L, Marco O, Albelda-Vitoria J, Tur M, Ródenas J. Modelos 3d hueso-implante combinando tac y cad en mallas cartesianas de elementos finitos h-adaptados. *Congreso de Métodos Numéricos en Ingeniería (CMN 2015)*, 2015. 5.1

[113] Giovannelli L, Ródenas J, Nadal E, Tur M. Patient-specific frequency analysis for the preoperative evaluation of implant stability. *VIRTUAL PHYSIOLOGICAL HUMAN 2018 (VPH2018)*, 2018. 5.1

[114] Samuelsson A, Wiberg NE, Zeng LF. The effectivity of the Zienkiewicz–Zhu error estimate and two 2D adaptive mesh generators. *Communications in Numerical Methods in Engineering* 1993; **9**(8):687–699, doi:10.1002/cnm.1640090808. URL http://dx.doi.org/10.1002/cnm.1640090808. 5.2

[115] Ródenas JJ, Tur M, Fuenmayor FJ, Vercher A. Improvement of the superconvergent patch recovery technique by the use of constraint equations: the SPR-C technique. *International Journal for Numerical Methods in Engineering* 2007; **70**(6):705–727, doi:10.1002/nme.1903. 5.2

[116] Ródenas JJ. Goal Oriented Adaptivity: Una introducción a través del problema elástico lineal. *Technical Report*, CIMNE, PI274, Barcelona, Spain 2005. 5.2

[117] Zheng Y, Li Z, Cao L. Unsupervised image histogram peak detection based on gaussian mixture model. *Applied Sciences in Graphic Communication and Packaging*, Zhao P, Ouyang Y, Xu M, Yang L, Ren Y (eds.), Springer Singapore: Singapore, 2018; 233–241. 5.2

[118] Navarro-Jiménez J, Tur M, Fuenmayor F, Ródenas J. On the effect of the contact surface definition in the cartesian grid finite element method. *Advanced Modeling and Simulation in Engineering Sciences* 2018; **5**(1), doi:10.1186/s40323-018-0108-5. 5.2

[119] Navarro-Jiménez J, Tur M, Albelda J, Ródenas J. Large deformation frictional contact analysis with immersed boundary method. *Computational Mechanics* 2018; :1–18doi:10.1007/s00466-017-1533-x. 5.2